

Fraihat, Jonas Darweesh  
Dinh, Kai Hoang  
Lerbakk, Hans Magnus Dahlstrøm

# Characterization of Fluid Flow for Rigid Glass Weave Filters (RGW) Karakterisering av væskeflyt for Rigid Glass Weave Filter (RGW)

Bachelor's thesis in Chemical Engineering  
Supervisor: Fritzsich, Robert  
May 2022



Fraihat, Jonas Darweesh  
Dinh, Kai Hoang  
Lerbakk, Hans Magnus Dahlstrøm

**Characterization of Fluid Flow for Rigid  
Glass Weave Filters (RGW)**  
**Karakterisering av væskeflyt for Rigid  
Glass Weave Filter (RGW)**

Bachelor's thesis in Chemical Engineering  
Supervisor: Fritzsich, Robert  
May 2022

Norwegian University of Science and Technology  
Faculty of Natural Sciences  
Department of Materials Science and Engineering





Faculty of Natural Sciences  
Department of Materials Science  
and Engineering

DEPARTMENT OF MATERIALS SCIENCE AND ENGINEERING

TKJE3001 - BACHELOROPPGAVE KJEMI

---

## Characterization of Fluid Flow for Rigid Glass Weave Filters (RGW)

---

---

## Karakterisering av væskeflyt for Rigid Glass Weave Filter (RGW)

---

*Authors:*  
Jonas Kai Hans Magnus  
Darweesh Fraihat Hoang Dinh Dahlstrøm Lerbakk

*Supervisor:*  
Robert Fritzsch

May 20, 2022

**Project number:** IMA-B-06-2022  
**Grading:** Open Thesis  
**Client:** Pyrotek Inc.  
**Contact:** Andrew Carlson

The Pyrotek logo features the word 'Pyrotek' in a bold, red, sans-serif font. The 'P' is significantly larger and more stylized than the other letters. A registered trademark symbol (®) is located at the end of the word.

### Statutory Declaration

I declare that I have developed and written the enclosed thesis entirely by myself and in collaboration with the group signed onto this work, and have not used sources or means without declaration in the text. Any thoughts or quotations, which were inferred from these sources, are clearly marked as such.

This report was not submitted in the same or in a substantially similar version, not even partially, to any other authority to achieve an academic grading and was not published elsewhere.

Trondheim, May 2022

*Jonas Fraihat*

Jonas Darweesh Fraihat

Trondheim, May 2022

*Kai Hoang Dinh*

Kai Hoang Dinh

Trondheim, May 2022

*Hans Magnus D. Lerbakk*

Hans Magnus Dahlstrøm Lerbakk

## Foreword

This thesis was written for our Bachelor's degree in Chemical Engineering at Norwegian University of Science and Technology in Trondheim. The task was given to us by Pyrotek Inc. through Norwegian University of Science and Technology. This topic is fascinating as there is a lot of room for improvement in filtration technology and being a part of this is exciting. Additionally, it was fun and challenging having to learn skills which are outside of the curriculum of our degree.

In the work encompassing this thesis we would like to offer our sincere thanks and appreciation to Dr. Robert Fritsch, our supervisor, for his patience, support and help in this undertaking. And following we would like to thank Pyrotek Inc. for providing us the materials needed to undertake this project, and more importantly giving Robert the time to supervise us and the four other groups vying for his attention. For the essential work necessary to facilitate this project we want to offer our gratitude to Ina Merete Stuen. We would also like to thank Andrey Kosinskiy for providing his time both to teach us how to prepare our samples for and the use of scanning electron microscopy. And we would like to thank Dimitry Silzovskiy for providing us with the necessary instructions for health and safety in the casting of metals, and also to find general equipment for use in our the pressure-drop experiments. In writing this report we would like to thank Hannes Zedel for reviewing our report and Mark William Kennedy for his willingness to grade this report. This thanks we also want to give to Andrew Carlson and Jay Fritzke for providing helpful information and willingness to attend a meeting with us. For providing us with the initial course on health and safety without which we would not be allowed to carry out the experiments, we would also like to thank Frida Hemstad Danmo.

As we are students of the Norwegian University of Science and Technology, we thank the university for the education encompassing and allowing us this undertaking. Following we would like to thank our lecturers for teaching us and providing us with the skills necessary in this undertaking. Also we want to thank the fellow students with Robert as a supervisor for their cordiality. Lastly we want to thank our parents and friends for their support throughout this project.

## Abstract

Filtration of metal inclusions is an important step in ensuring the castings meet the standards for cleanliness. In this respect the development of new metal filtration technology is of interest. One such technology is Rigid Glass Weave (RGW) which may replace the Ceramic Foam Filters (CFF) in foundry applications. While CFF is significantly better at lower flowrates, the RGW can handle very high flowrates and offers other advantages for casting machines in general. The focus of this thesis is the characterization of the flow through this filter. Five different weaves across two geometries were tried at various flowrates in a pressure-drop experiment. And the data was used in an attempt at quantifying the empirical constants in regards to the Forchheimer equation. Four methods were used in attempting to quantify these constants: Linear Regression, Ergun Empirical, Exponential Regression, and Brute Force. Of these, the first three were a form of linear regression. The quantification of the last method was treated as the expected value and used to quantify the p-values for the Linear Regression Method and the Ergun Empirical Method.

In addition, the system with each geometry was modelled in 2D and 3D using COMSOL Multiphysics®. Both the 2D models were simulated using by treating both the filter geometries as permeable media, and one filter geometry for the 3D model. The 3D model with a flat weave was modelled as individual strands, and simulated as such.

## Sammendrag

Filtrering av metallinkluderinger er et viktig steg i støpningsprosessen for å forsikre renhetskravet. I denne forstand er utvikling av nye metallfiltreringsteknologier interessant. En slik teknologi er Rigid Glass Weave (RGW) som kan erstatte Ceramic Foam Filters (CFF) for bruk i støperi. Mens CFF er betydelig bedre ved lavere væskehastigheter, kan RGW håndtere veldig høye væskehastigheter samt den tilbyr andre fordeler for støpningsmaskiner. Fokuset til denne oppgaven er karakteriseringen av væskeflyten gjennom filteret. To geometrier med fem forskjellige vevstyper ble testet ved flere væskehastigheter i et trykkforskjellsforsøk. Der dataen ble brukt i et forsøk på å kvantifisere empiriske konstanter i henhold til Forchheimers likning. Fire metoder ble brukt i forsøkene for å kvantifisere disse verdiene: Lineær Regresjon, Ergun Empirisk, Eksponentialregresjon og Ren Gjetting. Verdiene fra den siste metoden ble brukt som forventningsverdier til å kvantifisere p-verdier til Lineær Regresjon Metoden og Ergun Empiriske metoden.

I tillegg, ble systemet modellert i 2D og 3D med COMSOL Multiphysics® for hver geometri. I begge 2D simuleringene ble filtrene behandlet som permeable medier, samt en geometri i 3D modellen. 3D modellen med det flate vevet ble modellert med individuelle vev, og simulert i samme respekt.



# Contents

<b>Contents</b>	<b>v</b>
<b>1 Introduction</b>	<b>1</b>
<b>2 Theory</b>	<b>3</b>
2.1 Permeability . . . . .	3
2.1.1 Forchheimer Equation . . . . .	3
2.1.2 Ergun Equation . . . . .	3
2.2 Scanning Electron Microscopy . . . . .	4
2.3 Finite Element Modelling . . . . .	4
<b>3 Methodology</b>	<b>7</b>
3.1 Workflow . . . . .	7
3.2 Pressure Drop Experiments . . . . .	8
3.2.1 Experimental Setup . . . . .	8
3.2.2 Experimental Procedure . . . . .	9
3.2.3 Filter Placements . . . . .	9
3.2.4 Data Gathering . . . . .	11
3.2.5 Determination of the Empirical Constants . . . . .	11
3.3 Scanning Electron Microscopy . . . . .	15
3.3.1 Sand Casting of Metal Samples . . . . .	15
3.3.2 Metallographic Sample Preparation . . . . .	15
3.3.3 Scanning Electron Microscopy . . . . .	16
3.4 COMSOL Multiphysics® Modelling . . . . .	16
3.4.1 Making the 2D-Model . . . . .	16
3.4.2 Making the 3D-Model . . . . .	18
3.4.3 2D-Modelling . . . . .	20
3.4.4 3D-Modelling . . . . .	21
<b>4 Results and Discussion</b>	<b>25</b>
4.1 Water Trials . . . . .	25
4.1.1 In Regard to the Water Trials . . . . .	25
4.1.2 The Pressure Drop Results of the Flat and the Shaped Filters . . . . .	25
4.1.3 The First Regression Method: Linear Regression . . . . .	25
4.1.4 The Second Regression Method: Ergun Method . . . . .	29
4.1.5 The Third Regression Method: Exponential Regression . . . . .	32
4.1.6 Utilization of Brute Force . . . . .	35
4.1.7 In Regard to all Three Regression Methods . . . . .	38
4.1.8 The Pressure-Drop Results of the Ceramic Foam Filters . . . . .	40
4.2 Sand Casting and Scanning Electron Microscopy . . . . .	41
4.3 COMSOL Multiphysics® Modelling . . . . .	43
4.3.1 2D-Modelling . . . . .	44
4.3.2 3D-Modelling . . . . .	46
<b>5 Conclusion</b>	<b>53</b>
<b>6 Future Work</b>	<b>55</b>

<b>Bibliography</b>	<b>57</b>
<b>APPENDIX</b>	<b>59</b>
<b>A Filter House Dimensions</b>	<b>61</b>
<b>B SEM Samples</b>	<b>63</b>
<b>C SEM Pictures</b>	<b>67</b>

# List of Figures

1.1	Geometrical Shaped Filter of the Type Rigid Glass Weave . . . . .	1
1.2	Ceramic Foam Filter . . . . .	1
2.1	COMSOL Turbulence Model Example . . . . .	5
3.1	Workflow . . . . .	7
3.2	Process Flow Diagram of Setup for Pressure Drop Experiments . . . . .	8
3.3	Setup for the Pressure-Drop Experiments . . . . .	9
3.4	Geometric Weave in Filter House . . . . .	9
3.5	Flat Weave in Filter House . . . . .	9
3.7	Filter House in Pipe . . . . .	10
3.6	Ceramic Foam Filter in Filter House . . . . .	10
3.8	Flowchart of Pressure-Drop Data Manipulation . . . . .	12
3.9	Flowchart of the Exponential Regression Method . . . . .	13
3.10	Flowchart of the Brute Force Method . . . . .	14
3.11	Polishing Machine - ATM Saphir 360 . . . . .	15
3.12	Polishing Machine - ATM Saphir 350 . . . . .	15
3.13	Vacuum Chamber . . . . .	15
3.14	Cope and Drag . . . . .	15
3.15	Scanning Electron Microscopy Setup . . . . .	16
3.16	Outline of the 2D-COMSOL Multiphysics® Model . . . . .	16
3.17	Alternative Weaves Modelled in 2D . . . . .	17
3.18	Mesh of 2D-Models with Flat Weave and Geometric Weave . . . . .	17
3.19	Pre-Simplified 3D-Model of System Shape . . . . .	18
3.20	1/8th of the 3D-Model . . . . .	19
3.21	Process of Modelling for Geometric Weave . . . . .	20
3.22	3D-COMSOL Multiphysics® Model With Geometric Weave . . . . .	21
3.23	3D-Mesh of Flat Weave and Geometric Weave . . . . .	22
4.1	Constraint on the Inlet Tube . . . . .	25
4.2	Comparison of the 34L Weave using Linear Regression . . . . .	26
4.3	Comparison of the 36L Weave using Linear Regression . . . . .	27
4.4	Comparison of the 40L Weave using Linear Regression . . . . .	27
4.5	Comparison of the 43L Weave using Linear Regression . . . . .	27
4.6	Comparison of the XW2 Weave using Linear Regression . . . . .	28
4.7	Comparison of the Square and Circular Interior with Linear Regression . . . . .	28
4.8	Comparison of the 34L Weave using the Ergun Empirical Method . . . . .	30
4.9	Comparison of the 36L Weave using the Ergun Empirical Method . . . . .	30
4.10	Comparison of the 40L Weave using the Ergun Empirical Method . . . . .	30
4.11	Comparison of the 43L Weave using the Ergun Empirical Method . . . . .	31
4.12	Comparison of the XW2 Weave using the Ergun Empirical Method . . . . .	31
4.13	Comparison of the Square and Circular Interior with the Ergun Empirical Method . . . . .	31
4.14	Comparison of the 34L Weave using Exponential Regression . . . . .	33
4.15	Comparison of the 36L Weave using Exponential Regression . . . . .	33
4.16	Comparison of the 40L Weave using Exponential Regression . . . . .	33
4.17	Comparison of the 43L Weave using Exponential Regression . . . . .	34
4.18	Comparison of the XW2 Weave using Exponential Regression . . . . .	34

4.19	Comparison of the Square and Circular Interior with Exponential Regression . . . . .	34
4.20	Comparison of the 34L Weave using Brute Force . . . . .	36
4.21	Comparison of the 36L Weave using Brute Force . . . . .	36
4.22	Comparison of the 40L Weave using Brute Force . . . . .	36
4.23	Comparison of the 43L Weave using Brute Force . . . . .	37
4.24	Comparison of the XW2 Weave using Brute Force . . . . .	37
4.25	Comparison of the Square and Circular Interior with the Brute Force Method . . . . .	37
4.26	Comparison of Flat RGW-Filters . . . . .	39
4.27	Comparison of Geometric RGW-Filters . . . . .	39
4.28	Comparison of the 10 ppi and 20 ppi CFF-Filters . . . . .	41
4.29	A Comparison between RGW and CFF . . . . .	41
4.30	Successful Sand Casting . . . . .	41
4.33	Samples before and after Metallographic Preparation . . . . .	42
4.31	Unsuccessful Sand Casting . . . . .	42
4.32	Unsuccessful Sand Casting . . . . .	42
4.34	SEM Image - Samples . . . . .	43
4.35	Flow pattern of 2D-Model with Flat Weave . . . . .	44
4.36	Flow pattern of 2D-Model with Geometric Weave . . . . .	45
4.37	Trajectories of Simulated Particles . . . . .	46
4.38	Simulated Particle Movement . . . . .	46
4.39	Isosurface Plot of Solution for System with Geometric Weave . . . . .	47
4.40	Isosurface Plot of Solution for System with Geometric Weave . . . . .	47
4.41	Plots of Simulated Flow Pattern with Geometric Weave . . . . .	48
4.42	Pressure contour of 1/8th of Geometric Weave . . . . .	49
4.43	3D-Plot of Solution for System with Flat Weave . . . . .	51
4.44	Close-Up of Flat Weave Structure in 3D-Plot . . . . .	51
4.45	2D-Plot of the Filter House with a Flat Weave . . . . .	52
4.46	Close-Up of Jets in 2D-Plot of the Filter House . . . . .	52
B.1	Unpolished Sample of the 36L Geometrical Weave . . . . .	63
B.2	Unpolished Sample of the 40L Geometrical Weave . . . . .	63
B.3	Unpolished Sample of the 43L Geometrical Weave . . . . .	64
B.4	Unpolished Sample of the XW2 Geometrical Weave . . . . .	64
B.5	Polished Sample of the 36L Geometrical Weave . . . . .	64
B.6	Polished Sample of the 40L Geometrical Weave . . . . .	65
B.7	Polished Sample of the 43L Geometrical Weave . . . . .	65
B.8	Polished Sample of the XW2 Geometrical Weave . . . . .	65
C.1	SEM Image - Sample PO48 - 2505I (20x34L) . . . . .	67
C.2	SEM Image - Sample PO48 - 2505I (20x34L) . . . . .	67
C.3	SEM Image - Sample PO48 - 2505I (20x34L) . . . . .	68
C.4	SEM Image - Sample PO48 - 25052 (20x36L) . . . . .	68
C.5	SEM Image - Sample PO48 - 25052 (20x36L) . . . . .	68
C.6	SEM Image - Sample PO48 - 25052 (20x36L) . . . . .	69
C.7	SEM Image - Sample PO48 - 25052 (20x36L) . . . . .	69
C.8	SEM Image - Sample PO48 - 25052 (20x36L) . . . . .	69
C.9	SEM Image - Sample PO48 - 25052 (20x36L) . . . . .	70
C.10	SEM Image - Sample PO48 - 25052 (20x36L) . . . . .	70
C.11	SEM Image - Sample PO48 - 25052 (20x36L) . . . . .	70
C.12	SEM Image - Sample PO48 - 25052 (20x36L) . . . . .	71
C.13	SEM Image - Sample PO48 - 25052 (20x36L) . . . . .	71

C.14 SEM Image - Sample PO48 - 25052 (20x36L) . . . . .	71
C.15 SEM Image - Sample PO48 - 25052 (20x36L) . . . . .	72
C.16 SEM Image - Sample PO48 - 25653 (20x40L) . . . . .	72
C.17 SEM Image - Sample PO48 - 25653 (20x40L) . . . . .	72
C.18 SEM Image - Sample PO48 - 25054 (20x43L) . . . . .	73
C.19 SEM Image - Sample PO48 - 25054 (20x43L) . . . . .	73
C.20 SEM Image - Sample PO48 - 25054 (20x43L) . . . . .	73
C.21 SEM Image - Sample PO48 - 25054 (20x43L) . . . . .	74
C.22 SEM Image - Sample PO48 - 25054 (20x43L) . . . . .	74
C.23 SEM Image - Sample PO48 - 2505X (20xXW2) . . . . .	74
C.24 SEM Image - Sample PO48 - 2505X (20xXW2) . . . . .	75
C.25 SEM Image - Sample PO48 - 2505X (20xXW2) . . . . .	75
C.26 SEM Image - Sample PO48 - 2505X (20xXW2) . . . . .	75
C.27 SEM Image - Sample PO48 - 2505X (20xXW2) . . . . .	76

## List of Tables

4.1 Calculated Empirical Constants with Linear Regression . . . . .	26
4.2 Calculated Empirical Constants with Ergun Empirical Method . . . . .	29
4.3 Calculated Exponents from the Exponential Regression . . . . .	32
4.4 Calculated Empirical Constants with Exponential Regression . . . . .	32
4.5 Calculated Empirical Constants with Brute Force . . . . .	35
4.6 Determined Empirical Constants for RGW. . . . .	38
4.7 Calculated P-Values based on the Brute Force Method . . . . .	40
A.1 Dimensions of the Filter House . . . . .	61



# Introduction

# 1

Metal cleanliness is an important factor in the process of ingot production, due to how it can affect the final products and cause undesired performances in consumer items and industry. The metal cleanliness is measured by the amount, size, and identity of non-metallic inclusions in the molten metal and its products. There are therefore varying requirements for metal cleanliness to avoid performance issues, where filtration is an essential step to meet those requirements (in addition to other cleaning methods). Filtration is usually the final step of metal treatment before casting [1]. Today there are multiple filter solutions for the aluminium market. For cast houses, where metals are filtered at higher amounts and lower velocities ( $2 - 20 \text{ mm s}^{-1}$ ), it is normal to use bed filters, bonded particle tube filters, or high grid ceramic foam filters. In foundries, where metal is filtered in smaller amounts and higher velocities (up to several  $\text{m s}^{-1}$ ), it is common practice to use low grade ceramic foam filters and in the future potentially the Rigid Glass Weave (RGW) filters.

The aluminium industry being the second largest metal industry after the steel industry, is projected to grow more rapidly in the future. As the light metal industry is shifting into a greener economy as a response to global warming, the demand for aluminium is increasing. Aluminium is a highly versatile material that can be completely recycled without loss, and is important in, among others, the transport, construction, packaging and electrical sectors. [2].

Besides the increasing demand for more aluminium, more efficient technology is becoming more beneficial to use. In the aluminium foundry industry, the demand for new filter types with higher efficiency has been increasing. Although it is favourable to develop the most efficient and cost-efficient filters, it is required that these filters meet the quality standards for metal cleanliness in the industry. Currently in the aluminium foundry industry, the Ceramic Foam Filter (CFF) is normally used for filtration, where the Rigid Glass Weave filter stands as a possible replacement. Filters of the type Rigid Glass Weave are made of woven fiberglass and is a sheet-like filter, as shown in Figure 1.1, as opposed to the alumina construct that is CFF. Since the RGW-filter is a sheet-like filter, its structure does not have an impact on tortuosity, which CFF-filter structures have, as shown in Figure 1.2. The RGW-filter has performance benefits while having the same casting quality as CFF and does not require process changes or filter pocket modifications. The performance benefits include increased savings, process efficiency, pouring time consistency, and reduced abrasion on mould and mould coatings. Additionally, the RGW-filter reduces metal bypass significantly and remelts easily with the gating for recycling [3]. The focus in this thesis is setting a new reliability standard of the new filter type Rigid Glass Weave (RGW).

[1]: Chesonis (2017), *A Holistic Approach to Molten Metal Cleanliness*

[2]: International Aluminium Institute (2022), 'Opportunities for aluminium in a post-Covid economy'

[3]: Pyrotek (2022), *Rigid Glasweve® Filters for Sand and Permanent Mould Casting*



**Figure 1.1:** A geometrical shaped filter (20x43L) of the type Rigid Glass Weave. This type of filter is a sheet-like filter, its structure does not have an impact on tortuosity.

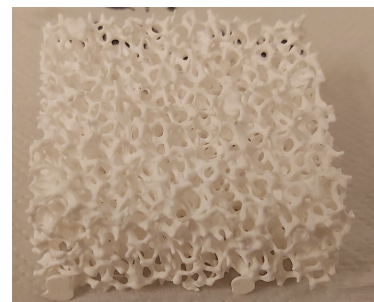


**Figure 1.2:** A Ceramic Foam Filter. This type of filter has a porous structure, which has impact on the tortuosity.





## 2.1 Permeability

Permeability is an important parameter in the characterization of Rigid Glass Weave filters (RGW), as it is important in the characterization of Ceramic Foam Filters (CFFs). The filter permeability can be used to predict the obtainable flowrate for an applied pressure gradient, or predict the required pressure drop to achieve a specific flowrate. The parameters can be expressed as a function of the fluid flow and medium properties, and can be obtained by fitting the experimental data with permeability equations [4].

[4]: Kennedy (2013), 'Removal of Inclusions from Liquid Aluminium using Electromagnetically Modified Filtration'

### 2.1.1 Forchheimer Equation

For a permeable medium, the velocity of a permeating liquid will cause a pressure drop across the media. These variables correlate with one another, and one empirical model for determining one of these variables from the other is the Forchheimer equation. This equation is shown in equation 2.1, and corroborates the pressure drop,  $\Delta P$ ; the filter length,  $L$ ; the liquid viscosity,  $\mu$ ; the density of the liquid,  $\rho$ , and two constants,  $k_1$  and  $k_2$ , which are the Darcy constant and Forchheimer constant respectively [5].

[5]: Forchheimer (1901), *Wasserbewegung Durch Boden*

$$\frac{\Delta P}{L} = \frac{\mu}{k_1} \cdot v + \frac{\rho}{k_2} \cdot v^2 \quad (2.1)$$

### 2.1.2 Ergun Equation

To express the Darcian and the non-Darcian permeability constant  $k_1$  and  $k_2$  respectively, Ergun proposed in 1952 the following expressions [6]:

[6]: Ergun (1952), *Fluid Flow through Packed Columns*

$$k_1 = \frac{\epsilon^3 d_p^2}{150 (1 - \epsilon)^2} \quad (2.2)$$

$$k_2 = \frac{\epsilon^3 d_p}{1.75 (1 - \epsilon)} \quad (2.3)$$

Where  $\epsilon$  is the fractional porosity, and  $d_p$  is the mean particle diameter. The Forchheimer equation can be modified using the expressions proposed by Ergun [6]:

$$\frac{\Delta P}{L} = 150 \frac{(1 - \epsilon^2) \mu}{\epsilon^3 d_p^2} V_s + 1.75 \frac{(1 - \epsilon) \rho}{\epsilon^3 d_p} V_s^2 \quad (2.4)$$

## 2.2 Scanning Electron Microscopy

SEM Scanning electron microscopy (SEM) is a type of electron microscope, which employs an electron beam to produce images samples with resolutions at nanometer scale. By using electrons instead of visible light as illuminating source, SEM can provide higher magnification than optical microscopes due to electrons having shorter wavelengths. SEM provides high-resolution imaging with large depth of field by using electrostatic and electromagnetic lenses to focus short wavelengths of electrons. The generated electrons produce a variety of useful signals when the electrons are employed on the sample. The different signals are based on their energy and how deep they come from within the sample. They carry different information about the sample, that can be captured by the microscope. Backscattered electrons (BSE) are electrons with higher energy and are scattered out of the sample while losing a small amount of energy. BSE provides compositional information, but lower resolution images. This is due to a strong interaction between sample and electrons within the sample (few microns deep). Secondary electrons (SE) reflect a few nanometers from within the sample, with a lower energy than BSE. The electrons are sensitive to surface structure and gives a topographic view of the sample. X-Rays are produced when electrons hit the surface of the sample, thus giving information about the elemental composition of the sample [7, 8]. The SEM system consists of [8]:

[7]: Scientific (2022), 'Principles of Scanning Electron Microscopy'

[8]: (2008), 'Principles of SEM'

- ▶ an electron source (electron gun);
- ▶ electrostatic lenses with apertures ;
- ▶ coils for scanning the beam;
- ▶ voltage and electronic controlling supplies;
- ▶ a electron beam deflection system for collecting and processing the signal information;
- ▶ a display monitor;
- ▶ a vacuum system for the source, column and specimen chamber.

At higher voltages, the electron wavelength decreases, thus giving increased resolution of the sample. While in scanning mode with standard SEM techniques (magnification ranging from 20X to approximately 30,000X, spatial resolution of 50 to 100 nm), image areas can range from approximately 1 cm to 5 microns in width [9].

[9]: Swapp (2017), 'Scanning Electron Microscopy (SEM)'

## 2.3 Finite Element Modelling

Finite Element Method (FEM) is used to compute numerical model equations that approximates how space- and time- dependent problems in physics are expressed. The description of the laws of physics for space- and time-dependent problems are usually expressed as partial differential

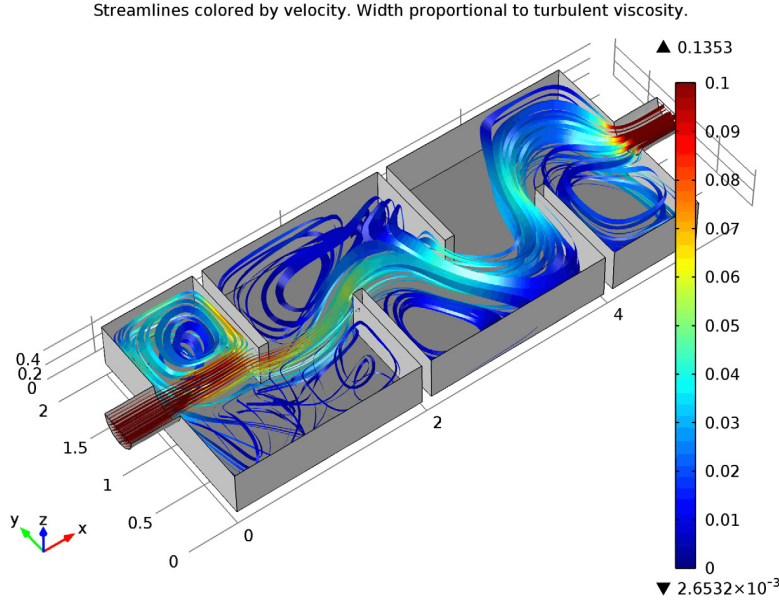


**Figure 2.1:** Model showing the flow pattern, flow velocity, and turbulent viscosity [11]

equations (PDE). These PDEs can not be solved with analytical methods and are therefore approximated by discretization methods. These discretization methods can approximate the PDEs by using numerical model equations that can be solved with numerical methods. COMSOL Multiphysics® can use FEM to perform computational fluid dynamic (CFD) simulations on fluid flow models [10]. The CFD module can be used to model the water trial system, as it includes a set of Reynolds-averaged Navier Stokes (RANS) turbulence models, and porous media flow simulation. Figure 2.1 shows a fluid flow model, computed with COMSOL Multiphysics® using the CFD module. Navier–Stokes equations can predict flow velocity, and pressure given geometry, and are therefore essential for fluid flow modelling. For compressible Newtonian fluid, the equation is expressed as:

[10]: COMSOL (2017), ‘The Finite Element Method (FEM)’

$$\underbrace{\rho \left( \frac{\partial u}{\partial t} + u \cdot \nabla u \right)}_{=1} = \underbrace{-\nabla p}_{2} + \underbrace{\nabla \cdot \left( \mu \left( \nabla u + (\nabla u)^T \right) - \frac{2}{3} \mu (\nabla \cdot u) I \right)}_{3} + \underbrace{F}_{4} \quad (2.5)$$

Where  $u$  is the fluid velocity,  $p$  is the fluid pressure,  $\rho$  is fluid density,  $\mu$  is fluid dynamic viscosity. The different terms correspond to the inertial forces (1), pressure forces (2), viscous forces (3), and the external forces (4). In higher turbulence models, the Reynolds number is very high, and the inertial forces are a lot more dominant than viscous forces. In these cases, RANS formulation of the Navier–Stokes equations is used to reduce computing power and time. Reynolds-averaged Navier–Stokes equations averages the velocity and pressure fields in time, and is expressed as follows:

$$\underbrace{\rho (+u \cdot \nabla u) + \nabla \cdot \left( \mu_T \left( \nabla U + (\nabla U)^T \right) - \frac{2}{3} \mu_T (\nabla \cdot U) I \right)}_{1} = \underbrace{-\nabla P}_{2} + \underbrace{\nabla \cdot \left( \mu \left( \nabla U + (\nabla U)^T \right) - \frac{2}{3} \mu (\nabla \cdot U) I \right)}_{3} + \underbrace{F}_{4} \quad (2.6)$$

[12]: COMSOL (2017), 'Navier-Stokes Equations'

Where  $U$  the time averaged fluid velocity,  $P$  is the time averaged fluid pressure and  $\mu_T$  is turbulent viscosity [12]. The turbulent viscosity is evaluated by using a RANS turbulence model. The various turbulence models provided by COMSOL Multiphysics® differ in how they calculate flow near walls, and what additional variables are computed in the RANS-equations. The turbulence model  $k-\epsilon$  consists of solving two additional equations for the transport of turbulent kinetic energy  $k$ , and rate of dissipation of turbulent kinetic energy  $\epsilon$ . This turbulence model is commonly used in the industry due to its flexibility, high convergence rate and lower computational intensity. The model is excellent for computing external flow problems around a geometry. Although being popular, the turbulence model does not compute flow fields with adverse pressure gradients and strong curvature very accurately. The turbulence model L-VEL computes the eddy viscosity using algebraic expressions based on the local fluid velocity and the distance to the closest wall. Unlike the turbulence model  $k-\epsilon$ , L-VEL does not compute additional transport equations. The model solves for the flow everywhere, and for requiring the least computational power of the various turbulence models, the model provides good approximations for internal flow, for example flow in a tube [13].

[13]: Walter Frei (2017), 'Which Turbulence Model Should I Choose for My CFD Application?'

## 3.1 Workflow

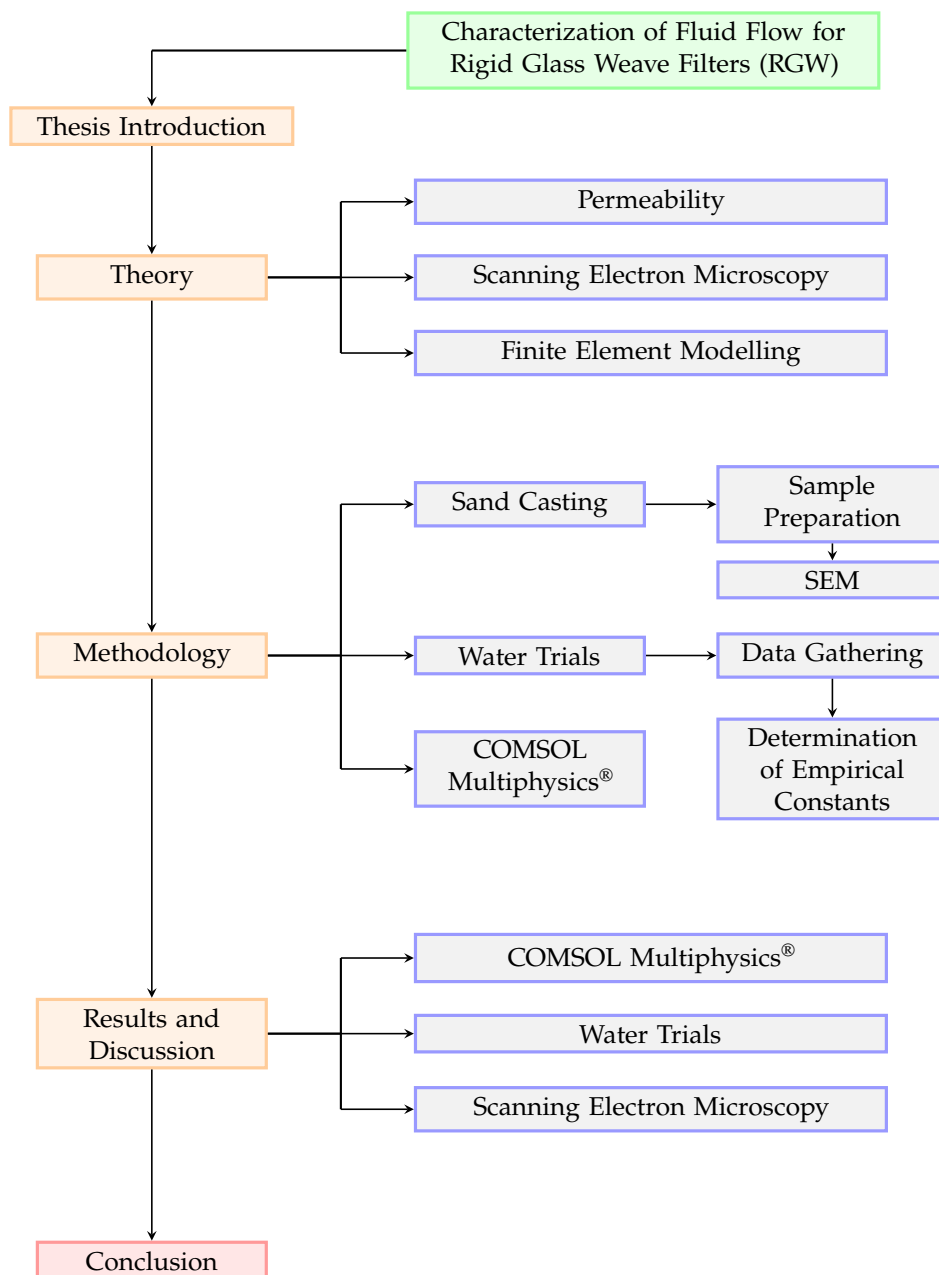


Figure 3.1: A flowchart showing the workflow of this thesis. The workflow contains each chapters and main subchapters for the thesis.

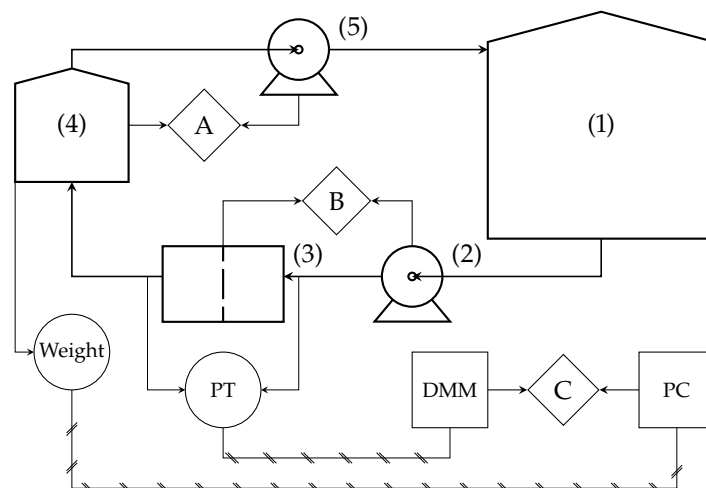
## 3.2 Pressure Drop Experiments

### 3.2.1 Experimental Setup

The experiment consisted of two tanks, intermediated by one pump, the filter house and tubing. This setup is illustrated in Figure 3.2, where the instruments used and the stations from which the experiment was performed also is shown. During the experiment, water would be driven out of the primary tank, either with gravity or the primary pump, through the filter house and into the secondary tank. The pressure drop across the filter house and the weight of the added water in the secondary tank would be measured respectively with a pressure transducer and a weight. This data would be logged using a digital multi-meter and a computer respectively. When the water in the secondary tank reached its capacity, the secondary pump would be turned on to empty its content back to the primary tank. Followed by updating the setting on the primary pump, and then disabling it. After the secondary pump had emptied the secondary tank, the weight was zeroed and the primary pump enabled to repeat the process.

Figure 3.3 shows an image of the experimental setups, including where each element of the experiment was placed in relation to Figure 3.2. In this figure we can see that the primary pump draws the water out of the primary tank through a piece of tubing. Following this the water is passed through a longer piece of tubing, circulating under a table until it reaches a bend, from which point the flow is straight. The next section the water passes is the filter house, of which a pressure transducer is connected to each end. And the water proceeds to a section of three bends leading to the secondary tank. This tank is placed atop the weight, of which only the backside of the display is visible. Additionally the secondary pump is placed inside the secondary tank, which draws its power from a power strip next to the primary pump. This power strip served as the power-switch for the secondary pump. Suspended above the system is a section of tubing that connects the secondary pump with the primary tank, and this was the tube used to return the water to the the primary tank. Further, a second tube can be seen in the figure leading to the primary tank, this was the tube used to fill the tank with water. Next

**Figure 3.2:** A process flow diagram that shows the experimental setup, including the measuring devices and stations during the experiment. (1) indicates the primary tank, (2) the primary pump, (3) the filter house, (4) the secondary tank and (5) the secondary pump. The diagram shows that the weight receives input from the secondary tank, while the pressure transducer receives input from the stream next to the filter house. Both the weight and pressure transducer send their signal to a computer (PC) and a digital multi-meter (DMM) respectively. The stations during the experiments are labelled respectively as A, B and C, where the instruments these stations control are shown with incoming arrows.



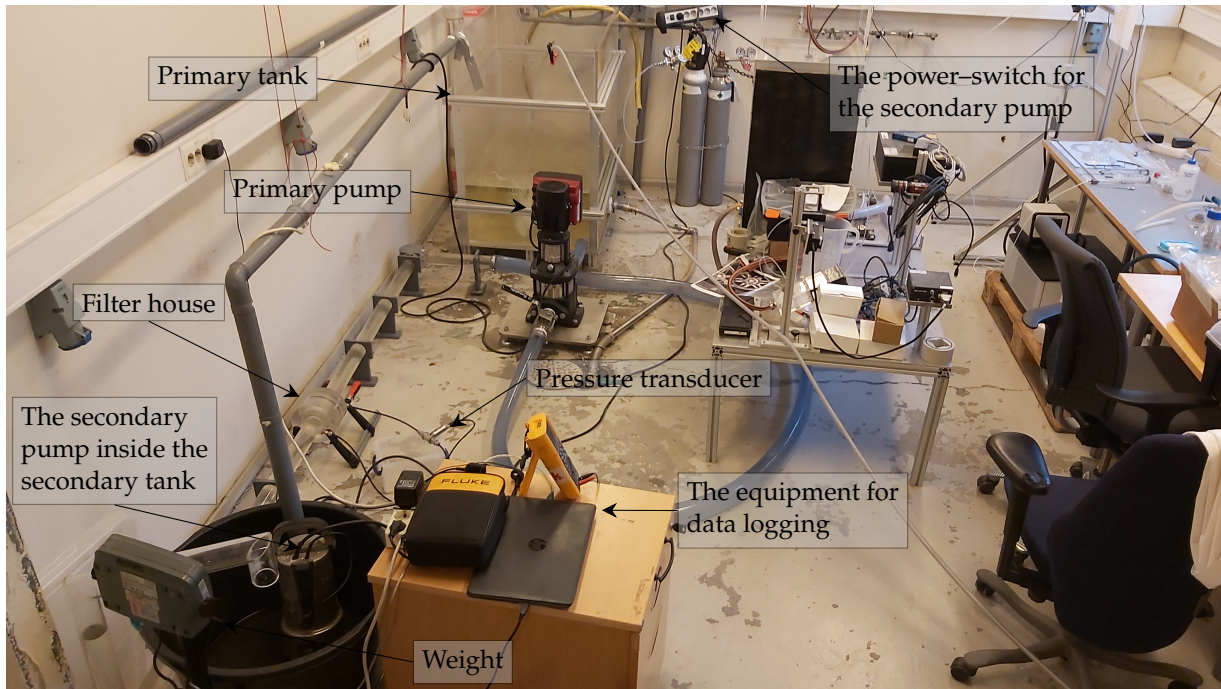


Figure 3.3: An image of the pressure-drop experiment setup, showing where each element in relation to Figure 3.2 is.

to the secondary tank, a pc and digital multi-meter can be seen, these were used to log the data in the experiment. Additionally, the following equipment was used:

**Primary pump:** CRE 15-1 N-A-A-E-HQQE No. 98390716

**Secondary pump:** Meek Tools 731-077

**Weight:** Ohaus Defender 3000 Model T31P

**Pressure transducer:** AEP DF2R

**Digital multi-meter:** Fluke 298 True RMS Multimeter

### 3.2.2 Experimental Procedure

The experiment involved five differing filter weaves and two different geometries, resulting in 10 different filters to measure the pressure drop for. Every filter was measured at 11 different velocities, ranging from 0; gravity driven; to 10; the highest setting on the primary pump that was used. The velocity measurements were done in series for each parallel. All the filters were measured using a square interior for the filter house, where one filter was used additionally with a circular interior. The circular interior had the same diameter as the length of one side for the square interior. It was the flat XW2 filter that was used with the circular interior, where the same individual filters were used a with both interiors.

### 3.2.3 Filter Placements

#### Shaped filter:

The shaped filters were placed in the square interior for the filter house, with vacuum grease lining a small interior protrusion at the end, made to hold the filter. The filters were placed in this

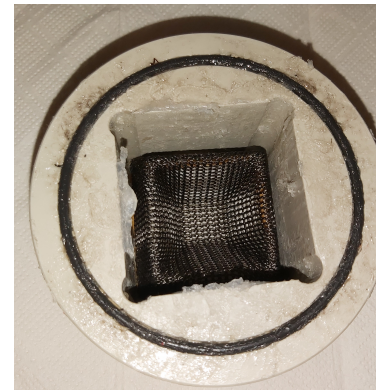


Figure 3.4: A geometric weave placed on the protrusions in the interior for the filter house.

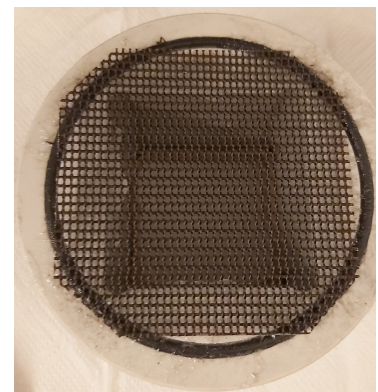
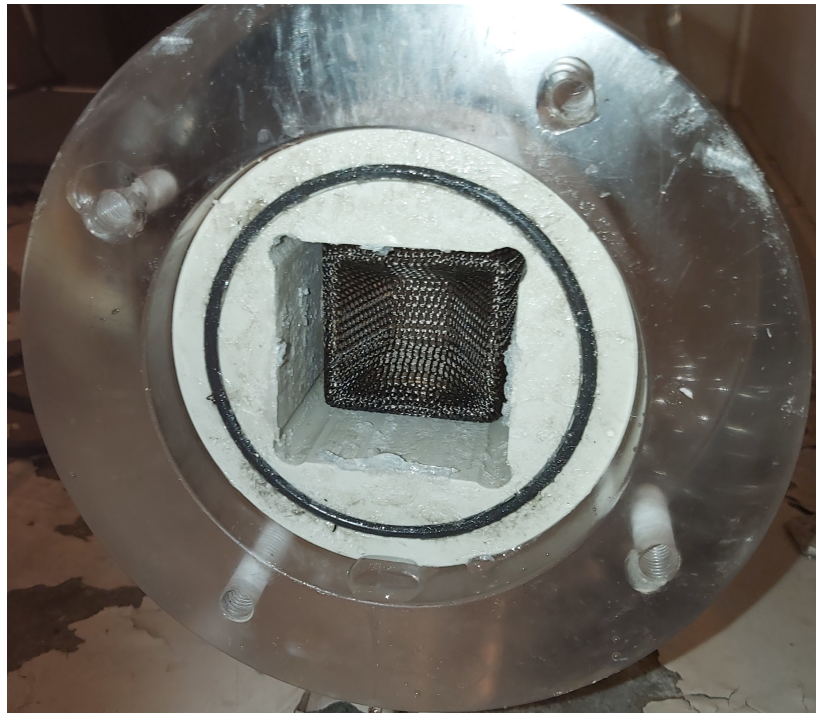


Figure 3.5: A flat weave with cut corners placed atop the square interior for the filter house.

**Figure 3.7:** The filter house with the flat interior. This figure shows the orientation the filter house interiors were placed in the experiment. A geometric weave can be seen inside the interior, and is atop the protrusions. On the front of the filter house interior, remnants of vacuum grease can be seen, which has been used to fix flat weaves to the interior. The flow would go through the interior in the direction the image is taken.



**Figure 3.6:** A CFF filter inside the interior to the filter house, placed atop the protrusions. On the obscured faces of the CFF filter is first a layer of cellulose paper and second a layer of silicone grease.

[14]: Zhang (2012), 'Liquid Permeability of Ceramic Foam Filters'

chamber with the edge of the filter resting atop this protrusion, using vacuum grease to secure the placement. The interior were then placed inside the filter house, aligned such that the protrusions are placed at the opposite face from the fluid flow. A geometric weave in this position can be seen in Figure 3.4.

#### **Flat filter:**

The flat filters were placed atop the interior, where parts of the filters that extended past the face of the interior was cut off. Figure 3.5 shows an example of this. The filters were placed on the same face that the shaped filter would be inserted inside the interior from, using vacuum grease to secure the placement. With both filters the interior would be placed the same way inside the filter house, such that the fluid flow would meet the flat filter prior to meeting the interior.

#### **CFF filter:**

The CFF filters were placed inside square interiors to the filter house, resting atop the same protrusions that hold the shaped filters. This filter would be inserted surrounded by cellulose paper on the obscured faces, where the cellulose papers were covered with silicone grease. This method of inserting CFF filters was gathered from [14], and can be seen in Figure 3.6.

An example of a filter placed inside the filter house is provided in Figure 3.7, where a geometric weave can be seen inside the square interior. In this figure, remnant of vacuum grease which has been used to affix a flat weave can be seen on the camera-facing face of the filter house interior. This grease can also be seen in Figure 3.4 and 3.6. The flow would pass through the filters in the same direction the camera is facing, where every filter was placed in the filter house and the accompanying interior in the same direction as shown.

For the RGW filters the following weaves were used across a flat and



geometric geometry. A representation of the geometric weave can be seen in Figure 3.4 and 3.7, whilst a representation of the flat weave can be seen in Figure 3.5.

- ▶ 20x34L
- ▶ 20x36L
- ▶ 20x40L
- ▶ 20x43L
- ▶ 20xXW2

These weaves are referred to by the unique part of their identifier, e.g. 34L for the 20x34L weave. The CFF filters were of pure alumina and of a 10 and 20 ppi, and was handmade by Dr.-Ing. Claudia Voigt [15].

### 3.2.4 Data Gathering

The data that was gathered from the experiment described in this section was manipulated programmatically, as shown in Figure 3.8. In the data, the first datapoint was set at a point in time after the start of the experiment. Every datapoint that followed this initial datapoint was appended to an empty variable. This was done until the difference between the current datapoint and the previous preceded a set tolerance, and the appended variables was appended as an entry in a dataframe. After which the following datapoints was discarded until this difference exceeded the absolute value of this tolerance. This indicated a switch to the next flowrate, where the datapoints was appended to a new empty variable. This procedure was repeated for every flowrate that was used in the experiment. This method for datamanipulation was used for both the weight measurement and the current measurement.

### 3.2.5 Determination of the Empirical Constants

The empirical constants,  $k_1$  and  $k_2$ , in regards to the Forchheimer equation, see equation 2.1, can be determined with several methods. In this thesis four methods for determining these constants are used, where the first three are taken from [14].

#### Linear Regression:

The first method is simply the utilization of multiple linear regression, with both a linear and second order term. In both these terms, the variable is the flowrate,  $v$ , and the regression is forced through the origin. Equation 3.1 shows the equation to which the experimental data is fitted to in the regression, and equation 3.2 and 3.3 show how the  $k_1$ - and  $k_2$ -values respectively are determined.

$$\frac{\Delta P}{L} = a \cdot v^2 + b \cdot v \quad (3.1)$$

$$k_1 = \frac{\mu}{b} \quad (3.2)$$

$$k_2 = \frac{\rho}{a} \quad (3.3)$$

#### Ergun Empirical:

The Ergun Empirical Method is similar to the Linear Regression Method, except that equation 3.1 is divided on both sides by the

[15]: Voigt et al. (2021), 'Overview of the Possibilities and Limitations of the Characterization of Ceramic Foam Filters for Metal Melt Filtration'

[14]: Zhang (2012), 'Liquid Permeability of Ceramic Foam Filters'

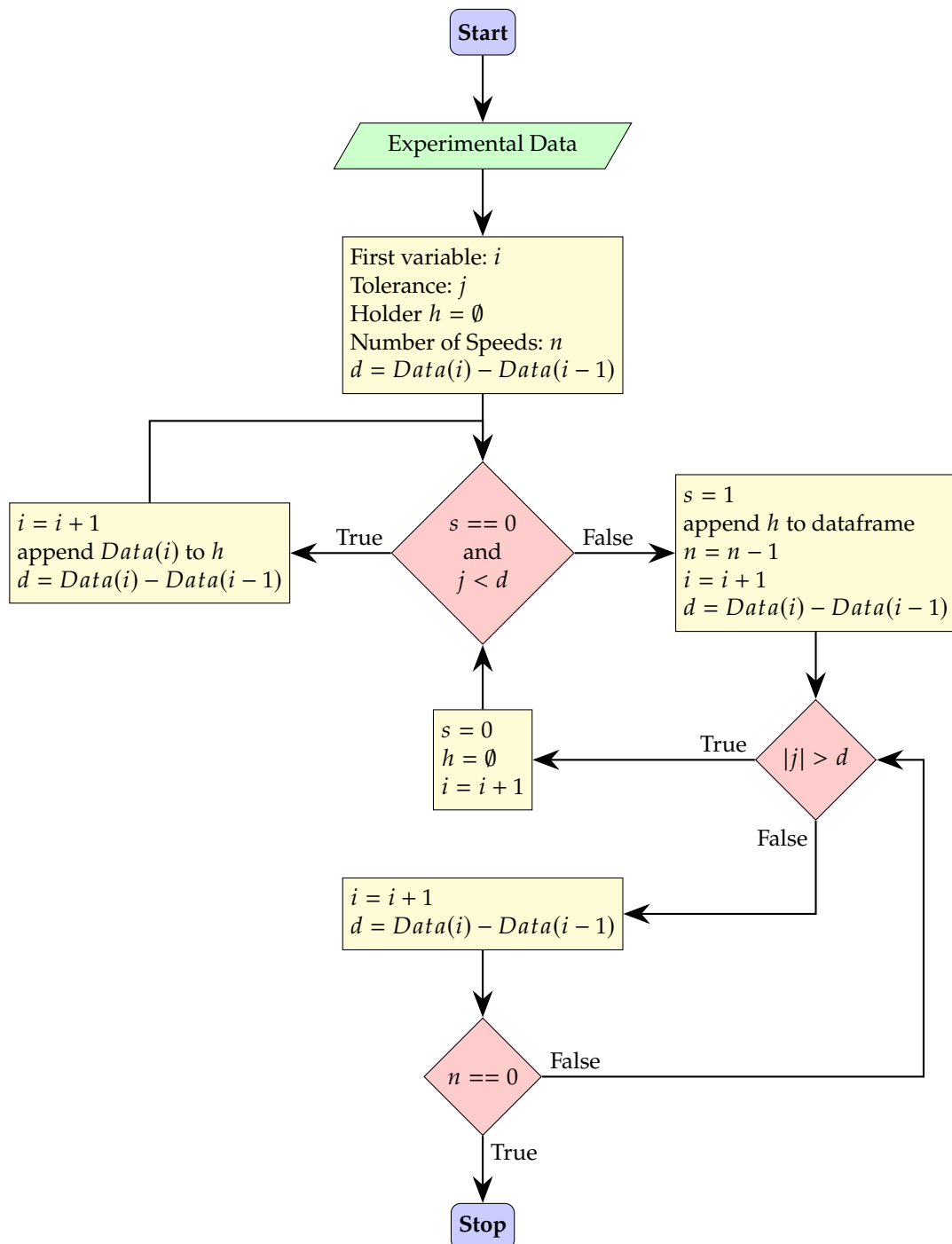


**Figure 3.8:** A flowchart describing how the experimental data was manipulated by programming to separate each flowrate in every parallel. This was done by specifying which datapoint was registered first, to ensure the experiment had begun in the data. Then appending every datapoint to an empty variable until the change in the values preceded a set tolerance, which indicate a termination of the current flowrate in the experiment. After this the datapoints begins to be registered after the change in the values exceed the tolerance, which indicate the initiation of the next flowrate in the experiment. This procedure is then repeated for every flowrate that was used in the experiment.

flowrate, giving equation 3.4, where this regression is not forced through the origin and due to the equation having a constant term. Here the empirical constants are similarly calculated as in equation 3.2 and 3.3.

$$\frac{\Delta P}{L} \cdot v^{-1} = a \cdot v + b \tag{3.4}$$

**Exponential Regression:**

The Exponential Regression Method is an iterative method whereby the Forchheimer equation is rearranged to isolate the second order term and then taking the logarithm of the equation, as shown in equation 3.5. Here the base for the logarithm is chosen to be 2. The iterative approach is done by guessing an initial value for  $k_1$ , such as 0, and then iteratively increasing this guess, as such the value of  $k_1$  is constrained to be positive. This incremental increase is coupled with fitting the experimental data to equation 3.5. In the initial part of the iteration, the number inside the left part of equation 3.5 could be negative, and in such instances the value of  $k_1$  was further incremented. This procedure is continued until the regressed constant for  $\log_2 v$  is as close to 2 as could be managed. This process is illustrated as a flowchart in Figure 3.9.

$$\log_2 \left( \frac{\frac{\Delta P}{L} - \frac{\mu}{k_1} \cdot v}{\rho} \right) = 2 \log_2 v - \log_2 k_2 \tag{3.5}$$

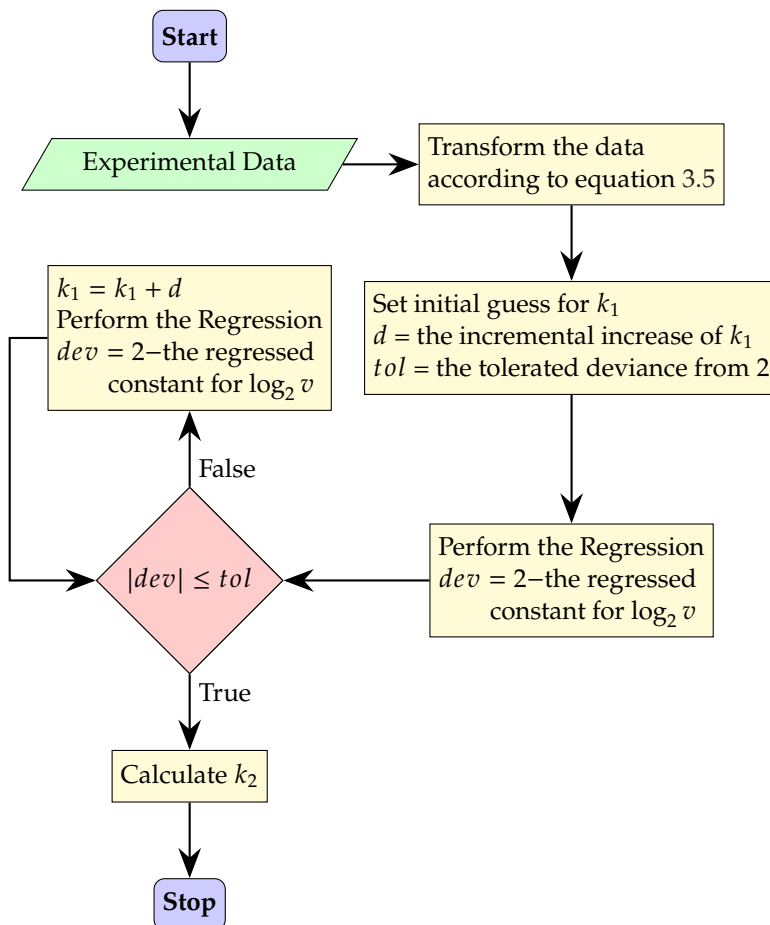


**Figure 3.9:** A flowchart showing the method by which the exponential regression was done. The method begins by transforming the data to a linear form, and then guessing an initial value for  $k_1$ . The linear regression is then done, and the deviancy of the resulting linear term from 2 is checked. If this deviance was greater than a preset tolerance the  $k_1$ -value would be incremented to a higher value. This would also happen if the  $k_1$ -value was too small, resulting in a negative value in the logarithm, which is not shown in the flowchart. This incremental increase of  $k_1$  would keep happening in a loop until the deviance was within the preset tolerance.

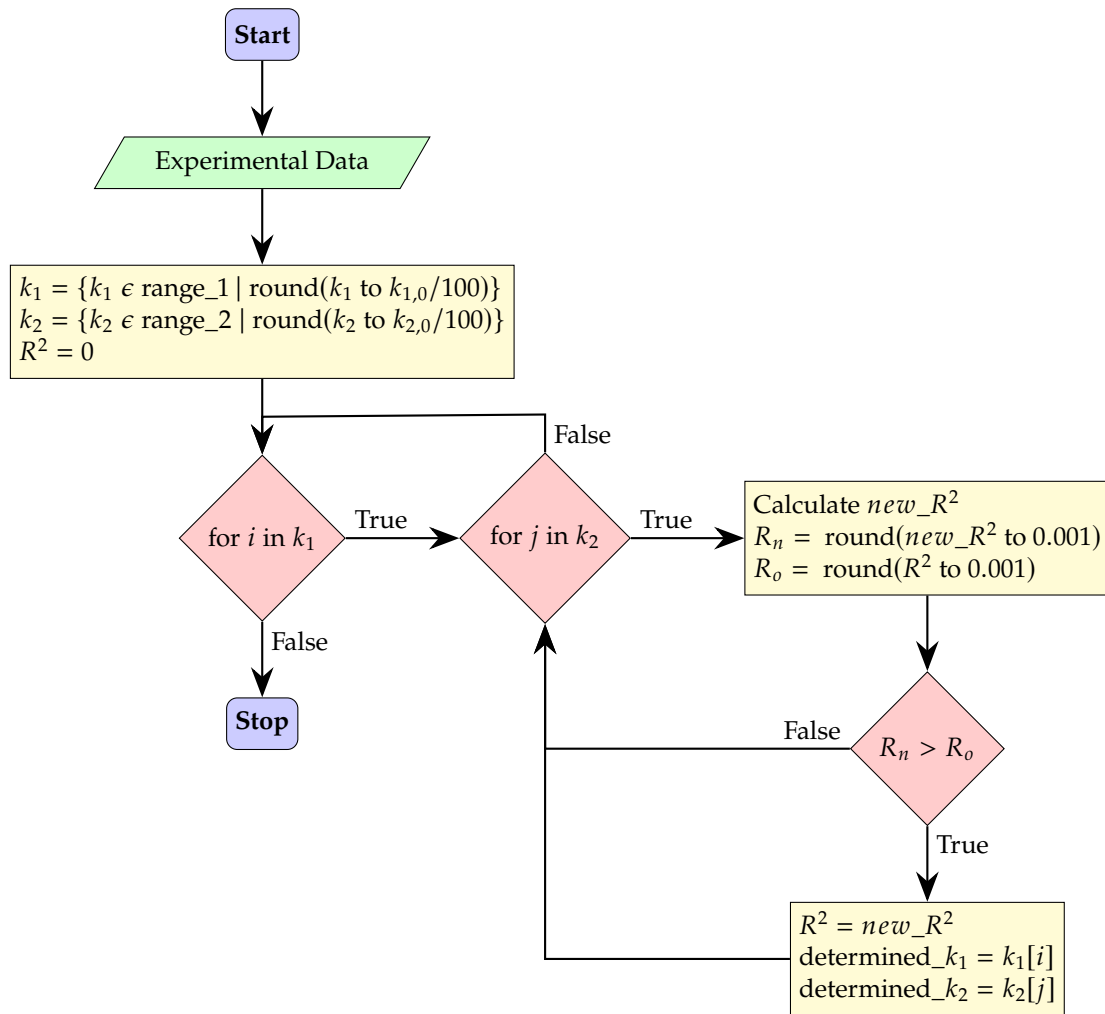


**Figure 3.10:** A flowchart describing the Brute Force Method, which starts by defining the range of both  $k_1$  and  $k_2$ , with their respective intervals. For every combination the  $R^2$ -value of both these values would be calculated, starting with  $k_1$  and looping through each  $k_2$ -value. The  $R^2$ -value is calculated as in linear regression forced through the origin. Every  $R^2$ -value is compared with the previous saved  $R^2$ -value, where both the new and old value are rounded to three decimals. By rounding to three decimals, the procedure is biased towards lower values of both  $k_1$  and  $k_2$ . If a new  $R^2$ -value is found to exceed the old to three decimals, this value for the  $R^2$  would be saved, along with the accompanying  $k_1$ - and  $k_2$ -values.

### Brute Force:

The brute Force Method is the only method that does not involve regression, where this method guesses both the  $k_1$ - and  $k_2$ -values for the Forchheimer equation. These values are incrementally increased iteratively in a predetermined range, where the  $R^2$ -value is calculated for every permutation of these values. The  $R^2$ -value is calculated as in linear regression forced through the origin [16]. And the predetermined ranges are based on the determined values from the previous three methods. During the calculation each newly calculated  $R^2$ -value is compared to the last saved  $R^2$ -value, and should the rounded value of this  $R^2$ -value to three decimals exceed the former  $R^2$ -value, again to three decimals, then the new value would be chosen in favour of the previous. The purpose of the rounding is to bias the  $k_1$ -value to a smaller magnitude, in order to avoid the eventuality of a negative  $k_1$ -value yielding the best fit. This method is illustrated with a flowchart in Figure 3.10.

[16]: Eisenhauer (2003), 'Regression through the Origin'

### 3.3 Scanning Electron Microscopy

#### 3.3.1 Sand Casting of Metal Samples

For the sand casting, an aluminium-alloy consisting of aluminium and silicon was used. The alloy was heated in a crucible using a casting oven until it melted. Red oil sand and a two-part casting flask of metal was used to create and hold the cope and drag for casting. Pockets for holding the filters were made, as shown in figure 3.14. The inlet and gas outlets were placed in a metal frame to create the cope. Talcum powder was dusted on the drag for easier separation of the frames after casting. The filters were then placed in the filter pockets in the drag, and the cope was placed on top. Figure 3.14 shows the cope and drag with the inlet and fume pipes. When the molten metal was sufficiently heated, it was poured into the inlet and filtered. After leaving the casting flask overnight for cooling, the metal solidified with the filter, and was removed from the flask for further processing. As there were 5 different types of filters to be sampled, the sand casting was done twice.

#### 3.3.2 Metallographic Sample Preparation

Before starting the metallographic sample preparation, the metal samples were cut using a bandsaw. They were cut in half along the height of the filter. In the sample preparation, the grinding of the samples were done using polishing machines with sand paper at different levels of grit. The model of the polishing machines used were ATM Saphir 360 and ATM Saphir 350, and is shown in Figure 3.11 and Figure 3.12. The sand papers were of the type Rhaco Grit by Akasel. At the first level, the samples were grinded with 220 grit sandpaper, and at the following levels, the level of grit were increasing until 4000 grit. At the second level 500 grit sandpaper was used; third level, 800 grit; fourth level, 1200 grit; fifth level, 2000 grit, and last level at 4000 grit. For these levels, ATM Saphir 360 polishing machines was used. Additionally, the samples were diamond polished using polishing pads of cloth and 3- and afterwards 1 micron-sized particles. The diamond polishing was done using ATM Saphir 350. Between each grinding and polishing level, the samples were put in an ultrasonic bath for cleaning. Then, the samples were cleaned even further by submerging them in ethanol. Lastly, they were dried with hot air and was put in a vacuum chamber for at least 24 hours to remove contaminants and water. Some of the samples drying in the vacuum chamber are shown in Figure 3.13.



Figure 3.11: The polishing machines used for grinding and polishing of the samples, ATM Saphir 360.



Figure 3.12: The polishing machines used for diamond polishing of the samples, ATM Saphir 350.



Figure 3.13: Vacuum drying of samples after being submerged in ethanol for at least 24 hours.

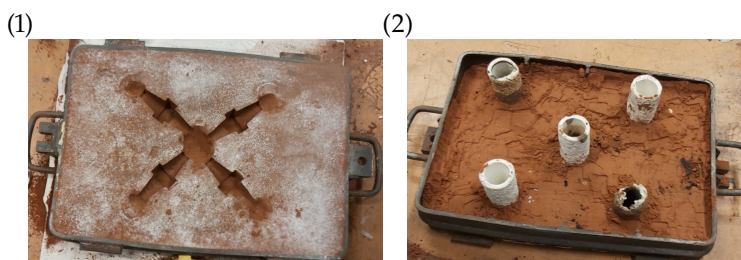


Figure 3.14: Figure to the left (1) shows the mould used for sand casting, which was the bottom of two layers of sand, where the filters were placed. Figure to the right (2) shows the top side of the sand casting setup, which consists of four fume pipes and one tube in the middle to pour molten metal into.



**Figure 3.15:** Setup consisting of the JEOL JCM-6000 scanning electron microscope, computer and display monitor.

### 3.3.3 Scanning Electron Microscopy

For the scanning electron microscopy, JEOL JCM-6000 scanning electron microscope (SEM) was used. The setup is shown in Figure 3.15. The polished samples were placed into the vacuum chamber of the SEM, and was examined and taken picture of one at a time. The focus of the microscopy was the weaves of the filter, and how the casted metal interacts with the weaves. The settings used for SEM were High-vacuum setting, 15 kV, PC-std and SEI as analysing method. Pictures of the filters were taken with zoom between 10x and 200x.

## 3.4 COMSOL Multiphysics® Modelling

Concerning the use of FEM in this project, only COMSOL Multiphysics® 5.5 was used. And two models of the geometric filters, that were made in Solidworks, was provided for use in COMSOL Multiphysics®. Two main models were made in COMSOL Multiphysics®, one for 2D-modelling and another for 3D-modelling. Appendix A shows the dimensions for the filter house with the square interior, as the circular interior was not modelled. These main models were modified for use with the flat or geometric weaves. Of the modules in COMSOL Multiphysics® that Norwegian University of Science and Technology provided licences for, only the following three were used:

- ▶ Free and Porous Media Flow (*fp*)
- ▶ Turbulent Flow,  $k-\varepsilon$  (*spf*)
- ▶ Particle Tracing for Fluid Flow (*ftp*)

In addition, there are several factors that were assumed to be negligible during the modelling. These aspects were the hydrodynamic pressure from the primary tank, the outlet head, backpressure and minor gaps in the geometry. For the inlet, the flow was defined as a fully developed flow, whilst the outlet was defined with a pressure of 0.



**Figure 3.16:** The outline of the 2D-COMSOL Multiphysics® model. In this figure a subsection of the whole system is shown, where the filter house is shown with the inlet and outlet tube on both sides. The flow goes from top to bottom, and the voids in the filter house next to the outlet tube represent the protrusions in the filter house.

### 3.4.1 Making the 2D-Model

The 2D-model was made using parameters defined in COMSOL, and are the following:

- ▶ The coordinates for the origin
- ▶ The filter thickness, 0.1 mm
- ▶ The dimensions of the filter house and the tube diameter, see Appendix A
- ▶ The length of the tube, treated as 0.3 m
- ▶ The flowrate, a range for this variable was used mainly based on the experimental data. All the values in the specified range was used in a parametric sweep, and these values were: 0.1, 0.2, 0.3, 0.4, 0.5, 0.6, 0.7, 1.0, 1.5 and 2.0  $\text{m s}^{-1}$

With these parameters an outline of the system was made, which consisted of the inlet and outlet tubes, the filter house and the small protrusions of the filter house. This outline is shown in Figure 3.16. After this, the relevant filter was placed in this system. For the flat weave, it was defined

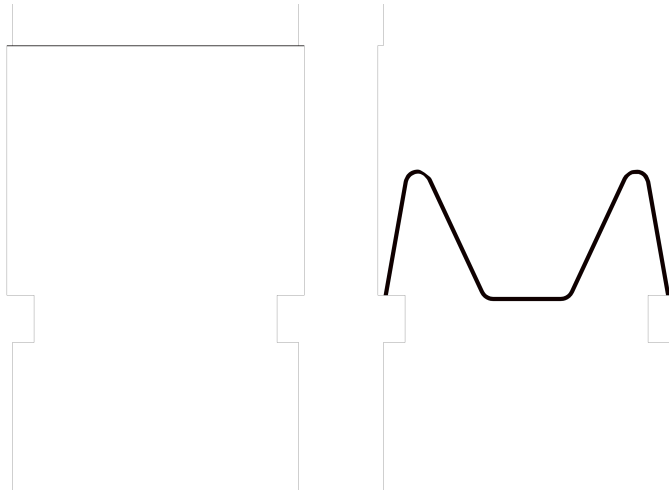


**Figure 3.17:** Both alternative weaves that were modelled in 2D with COMSOL Multiphysics®. Here the leftmost image shows the system with the flat weave, where it is illustrated in black. And the rightmost image shows the system with the geometric weave, also illustrated as black.

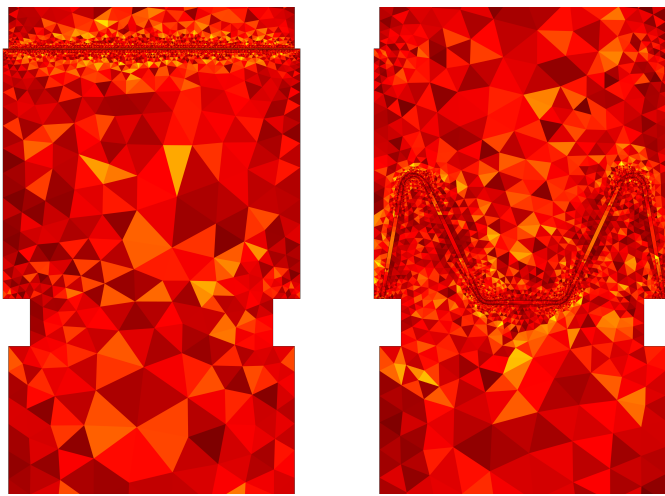


**Figure 3.18:** On the left is an image showing the mesh for the 2D-model with the flat weave, while on the right is an image showing the mesh for the 2D-model with the geometric weave.

as a rectangle spanning the length of the filter house and with the width of the filter thickness. And it was placed next to the inlet tube in the filter house. For the geometric weave, the Solidworks model of the whole geometric weave was first loaded in a 3D-COMSOL model. A workplane was placed inside this model, and a 2D-cutout of the model was traced using the sketch function in COMSOL with a polygon. Afterwards a fillet was added to the edges in the bent parts of the geometry. The geometry was then exported, and imported to the 2D-model. The geometry was then placed atop the protrusion inside the filter house. Both these weaves can be seen inside the model in Figure 3.17, where the flat weave is shown to the right, and the geometric weave is shown to the left.

The mesh for the 2D-model was made the same way for both the flat weave and the geometric weave. A free triangular mesh was added to the weave. This mesh was calibrated for general physics, and had a predefined extremely fine element size. The mesh for the remaining geometry was added as a boundary layers, with the number of boundary layers being 16; the boundary layer stretching factor being 0.1; the thickness of the first layer being automatic; the thickness adjustment factor being 0.1 and the element size scale being 1.1. In Figure 3.18 the mesh for the 2D-model for both the flat and geometric weave can be seen respectively.

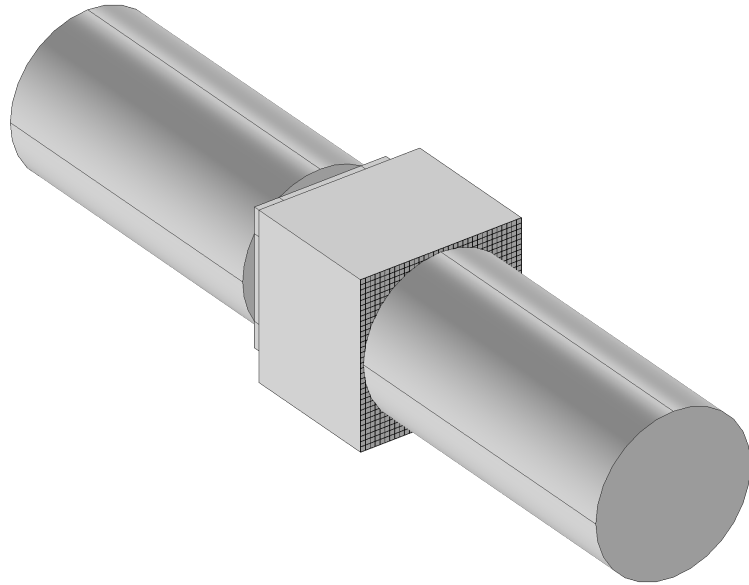


**Figure 3.19:** The 3D-model as it was constructed prior to simplifying it in order to use symmetry in the model. Here the shape of the system is shown, where the inlet would be on tube to the bottom left, and the outlet on the top right. In this figure the void where the filter house would have occupied next to the outlet tube represent the protrusions in the filter house. Additionally, the grid on the face of the filter house represents the flat weave.

### 3.4.2 Making the 3D-Model

The 3D-model was also made using parameters defined in COMSOL, and are the following:

- ▶ The coordinates for the origin
- ▶ The filter thickness, 0.1 mm
- ▶ The dimensions of the filter house and the tube diameter, see Appendix A
- ▶ The length of the tube, treated as 0.1 m
- ▶ The number of strands, which described how many individual strands each axis of the flat wave was composed of. The number that was used was 80, and is arbitrary.
- ▶ The flowrate, a range for this variable was used mainly based on the experimental data. All the values in the specified range was used in a parametric sweep, and these values were: 0.1, 0.2, 0.3, 0.7, 1.0, 1.5, 2.0 and 3.0  $\text{m s}^{-1}$ .

In making the 3D-model, the flat weave was added whilst the model was built. First the basic outline for the whole system was made based on the dimensions in Appendix A. In addition to this, the flat geometry was added as an array of cylinders, with the same diameter as the filter thickness, on both cross-sectional axes prior to the filter house, and spanning the length of the filter house. This is shown in Figure 3.19, where the model at this stage is shown. The part of the flat geometry that extended past the inlet cylinder was cut off and removed from the model. Following this, a geometry that covered one eighth of the model axially, from the center, was made. This geometry covered the model from the corner of one of the diagonals to the center of the adjacent side, and was subsequently used to remove the remaining uncovered parts of the model. Figure 3.20 shows the model at this stage, where the diagonal face is hidden to show the interior of the system. The fact that the filter houses protrusion only covers a part of the access to the outlet tube is visible in this figure, as well as the geometry for the flat weave.



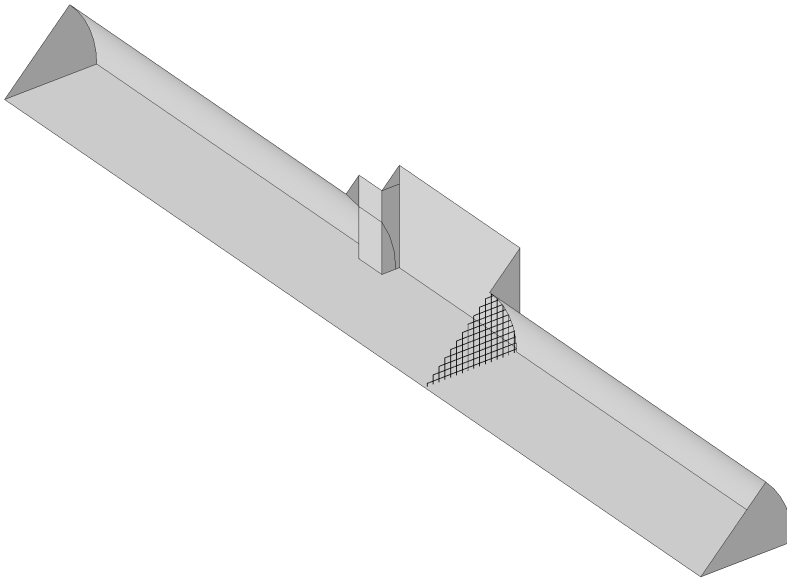
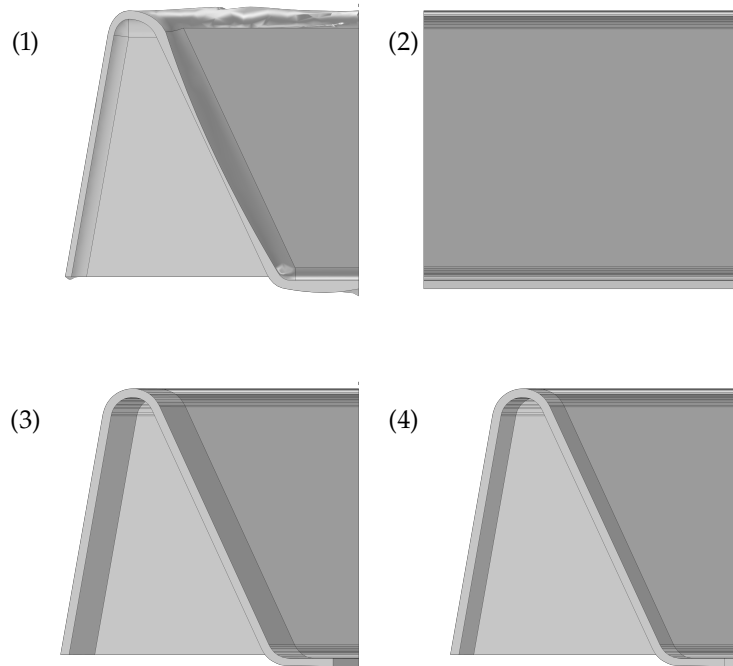


**Figure 3.20:** The 3D-model after one eighth of the model was cut off, to allow for the use of symmetry. In the figure the diagonal face is hidden to show the interior of the model, where the geometry for the flat weave is visible in addition to the protrusion in the filter house. It can be seen that the protrusion of the filter house covers a part of the beginnings of the outlet tube in the middle of the filter house, and extends past this opening in the diagonal.

Next, the model for the geometric weave was added. This was done by first importing a provided Solidworks model for 12.5% of the filter that matched the cutout of the system. Based on this model a separate model for this weave was made in COMSOL due to a lack of a license for the CAD import module. First a workplane was added on the face of the imported model that matched the middle of the filter house. In this workplane a 2D-cross-section of this face was traced using the sketch function in COMSOL with a polygon, and a fillet was added to the edges of the bent parts in the geometry. This 2D-model was extruded over the imported model, and partitioned using a workplane that was added in the initial part of the bend in the model. This workplane was used to make a cross-section of the extrusion, which was extruded to diagonal face of the imported model. Afterwards, another workplane was added to the flat face of the second extrusion, that was located where the central part of the whole geometry would be. A cross-section of this face was extruded, and partitioned using a workplane on the first extrusion, where this workplane was placed on the face that would be in the middle of the filter house. The separate parts of the simplified model for the geometric weave was joined together in a union, and this process of making this part can be seen in Figure 3.21.

The model of the geometrical weave was scaled down to an appropriate size and rotated to fit inside the filter house. It was moved inside the filter house such that the central point of the geometric weave was placed along the central axis of the system, and the middle face of the model was placed on the middle wall of the system. The diagonal face of the geometric weave was subsequently extruded to match the diagonal face of the system, and the resulting hole in the center of geometric weave was filled by extruding the face and cutting it using the faces of the system. Additionally the part of the geometric weave that extended past the protrusion in the filter house was cut from the model. Following, the parts that constituted the model of the geometric weave was joined together in an union, where Figure 3.22 shows the model at this stage.

**Figure 3.21:** Four images representing how the model for the geometric weave was made in COMSOL Multiphysics®. (1) shows the imported Solidworks-model of 12.5% of the geometric weave. (2) shows the extruded 2D cross-sectional tracing of the right face of (1). (3) shows the geometry after a workplane was added to the beginning of the curvature on (1), and used to both partition and take a cross-section of (2). This cross-section was the extruded to the left face of (1). (4) shows geometry after a workplane was added to the front face of (2), and its cross-section was extruded. Afterward this extrusion was partitioned with a workplane on the right of (2), and the various parts of this geometry was joined together in a union. Above each of these images a small part can be seen to the right, this is the 3D model of the system.



At this stage in the making of the 3D-model, the relevant weave was deleted to facilitate the meshing and modelling. In both instances several edges in the model was removed, where they were not necessary for maintaining the geometry, including most of the edges in the model for the geometric weave, particularly the ones on the bent part of the weave. For both the versions of the model, a mapped mesh was added in both the inlet and outlet tube from the inlet or outlet respectively partway towards the filter house, with a predefined fine element size. All the other meshes was done using a free tetrahedral mesh, and in both versions the inlet and outlet faces mesh was predefined with an extremely fine element size. Both the flat weave and geometric weave was meshed with a predefined finer element size, and the remaining geometry was mapped with a predefined finer element size. Every mesh was calibrated for fluid dynamics, and the meshed model for the flat and geometric weave respectively is shown in Figure 3.23.

### 3.4.3 2D-Modelling

For both modelling the flat and geometric weave, the Free and Porous Media Flow (*fp*) module was used. With this module the whole system was assigned water as the fluid, whilst the filter material was user defined with the following three properties: a density of  $1000 \text{ kg m}^{-3}$ , a dynamic viscosity of  $0.001 \text{ Pa s}$  and a porosity of 0.4. This material was applied to the weave. Following this, the edge at either extreme of the system for the inlet and outlet tube was respectively defined as the inlet and outlet. The initial conditions was defined with no velocity field and no pressure. Fluid and matrix properties was assigned to the weave geometry, where the permeability model that was used was Kozeny-Carman, with a particle diameter of the filter thickness. For the module, the L-VEL turbulence model was used.

This turbulence model was used due to the Fluid and matrix properties not being compatible with the  $k-\epsilon$  turbulence model.

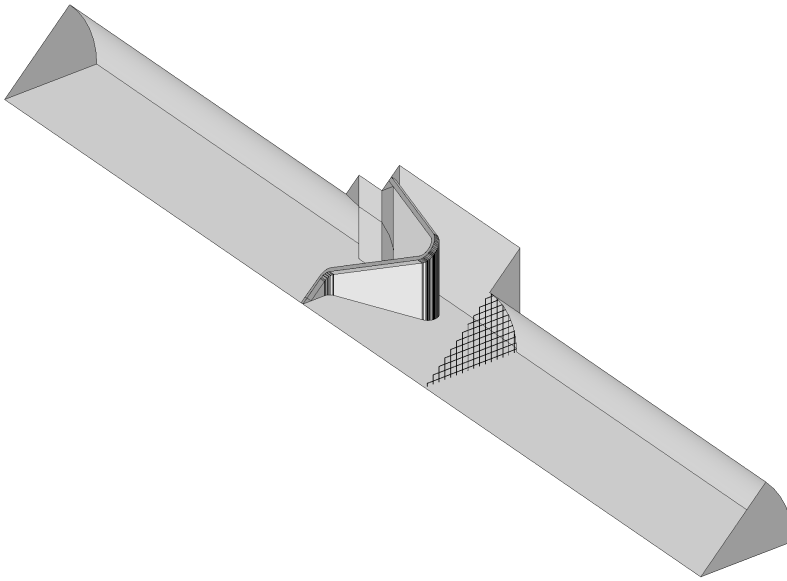


**Figure 3.22:** The 3D-COMSOL Multiphysics® model after adding the geometric weave. It is visible that the placement of the geometric weave is downstream from the placement of the flat weave, and that the geometric weave rests on the protrusions in the filter house.

Only in the 2D-model was the Particle Tracing for Fluid Flow (*ftp*) module used. And this module was used in conjunction with the geometric weave. Here, release times were specified, with a maximum number of secondary particles of 5000. The particle properties were defined to be a density of  $1000 \text{ kg m}^{-3}$  and a diameter of the filter thickness. The inlet was defined as a list of values, with a release time of 0 to 0.005 s, and intervals of 0.001 s. A density based initial position was used, where the density was proportional to the solved velocity field and the number of particles per release was 1000. An expression based initial velocity was used, where this expression was the solved velocity field. The outlet wall condition was set to disappear. A drag force was added to the system, using Stoke's law, where the velocity was set to the solved velocity field. Additionally the discrete random walk turbulence dispersion model was used.

Both studies for the permeability of the flat and geometric weave used a stationary solver, with a parametric sweep. Here only the Free and Porous Media Flow (*fp*) module was used. The study for particle tracing used only the Particle Tracing for Fluid Flow (*ftp*) module, where a time dependant solver was used. In this solver the time unit was a second, and it solved for a range from 0 to 0.5 s, with a step of 0.0025 s.

### 3.4.4 3D-Modelling

With the 3D-model both the Free and Porous Media Flow (*fp*) and the module Turbulent Flow,  $k-\epsilon$  (*spf*) module was used. These modules were used respectively for the geometric and flat weave. And the Free and Porous Media Flow used the L-VEL turbulence model, where the Turbulent Flow,  $k-\epsilon$ , module used the  $k-\epsilon$  turbulence model. Both models defined the fluid properties from the model, where water was assigned as the material for the whole model and a user defined material with the following properties was assigned to the respective weaves: a density of  $1000 \text{ kg m}^{-3}$ , a dynamic viscosity of  $0.0001 \text{ Pa s}$  and a porosity of 0 and 0.4 for the flat and geometric weave respectively. Both modules used an

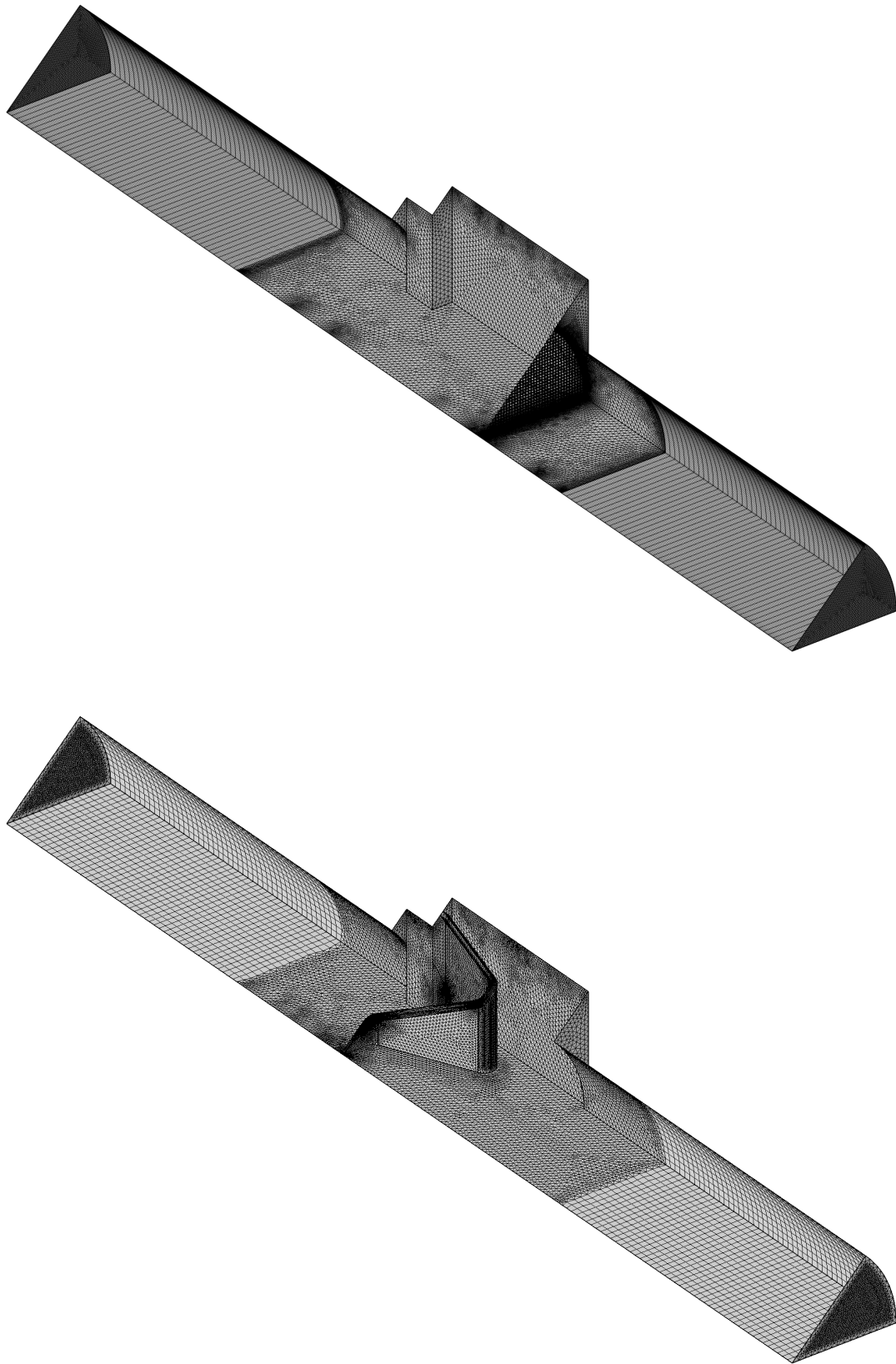


**Figure 3.23:** On the top, the mesh for the 3D-model with the flat weave is shown, and similarly the mesh for the 3D-model with the geometric weave is shown on the bottom. In both images, the use of a free tetrahedral mesh for both the inlet, outlet and the respective weave is shown. And the use of a mapped mesh next to the inlet and outlet is shown. Additionally, it is shown that the whole filter house and part of the tubes use a free tetrahedral mesh, where this was defined as the remaining parts of the geometry.

initial value of no pressure and no velocity field. The inlet was defined as a fully developed flow with an average velocity for both weaves, and the outlet with a pressure of 0. Symmetry was used for both modules, with it being assigned to the diagonal and middle face in relation to the filter house, and this was assigned to the faces of the tubes, filter house and weave. For the Turbulent Flow,  $k-\epsilon$ , module a interior wall was added around the geometry for the flat weave, with a no slip boundary condition. Additionally, both models used a stationary solver with a parametric sweep.



## 4.1 Water Trials

### 4.1.1 In Regard to the Water Trials

During the experimental procedure only 10 settings for the speed on the primary pump were used, excluding the gravity driven velocity. These velocities were used due to two factors: (1) during the initial run of the experiment, one filter was shot through the filter house at a higher pressure. (2) the tube which connected the primary tank and the primary pump was constrained during the higher velocities, which is shown in Figure 4.1. This strain is due to this tubing only being made to withstand atmospheric pressures, and is believed to constrain the achievable flowrates in the experiment.

Another limiting factor for this experiment was the size of the secondary tank, and this constraint was furthered by the secondary pump being placed inside this tank. Thus, the size of this tank was the primary constraint of the experiment, as it limited the number of measurements at higher flowrates. This will accentuate any variability in the experimental measurements, both for the weight and the pressure–transducer, as both these instruments measurements were time dependent. This is a bigger source of error for the weight measurements than for the pressure–drop measurements, due to the weight measurements being used to calculate the flowrate. Difference between the weight at the extremities for each flowrate is used for this calculation. As such any variance in these measurements will result in a larger error for the higher flowrates due to a smaller time window to offset this error.

### 4.1.2 The Pressure Drop Results of the Flat and the Shaped Filters

In the following sections the pressure–drop results are presented. The first four sections show these results and the determined empirical constants for their respective method. These methods being the Linear Regression Method, the Ergun Empirical Method, the Exponential Regression Method and the Brute Force Method. In each of these sections the empirical constants are presented in a table, and the predicted pressure–drop values are compared with the measured values for each weave in separate figures. And all of these sections compares the square and circular interior for the filter house. Following this, every method is compared in a separate section, where weaves themselves are compared to each other across geometry.

### 4.1.3 The First Regression Method: Linear Regression

Table 4.1 shows the calculated  $k_1$ – and  $k_2$ –values using the first method for regression. As can be seen in this table, not all of  $k_1$ –values are positive.



**Figure 4.1:** An image of the constrained tube, with an unconstrained tube behind. Both these tubes are rated for atmospheric pressure, and the constrained tube is the one connecting the primary tank with the primary pump. This tube experienced constraint with the use of the higher settings of the primary pump.

**Table 4.1:** The calculated empirical constants for each filter in regards to the Forchheimer equation, where the values are determined with the Linear Regression Method. The first six rows show the flat weaves, whilst the last five show the geometric weaves. And the following three columns shows the  $k_1$ ,  $k_2$  and  $R^2$ -values.

Filter:	Linear Regression		
	$k_1$ :	$k_2$ :	$R^2$ :
Flat (20x34L)	1.21e-12	2.99e-07	0.995
Flat (20x36L)	-9.90e-13	1.55e-07	0.989
Flat (20x40L)	-6.27e-13	1.47e-07	0.989
Flat (20x43L)	-4.04e-13	1.14e-07	0.984
Flat (20xXW2) square opening	1.17e-12	1.39e-07	0.991
Flat (20xXW2) circular opening	5.45e-12	1.74e-07	0.995
PO48 - 2505I (20x34L)	5.64e-13	8.13e-07	0.955
PO48 - 25052 (20x36L)	-6.18e-13	2.32e-07	0.962
PO48 - 25653 (20x40L)	-7.16e-13	2.70e-07	0.977
PO48 - 25054 (20x43L)	-2.38e-12	2.99e-07	0.988
PO48 - 2505X (20xXW2)	7.13e-13	2.59e-07	0.989

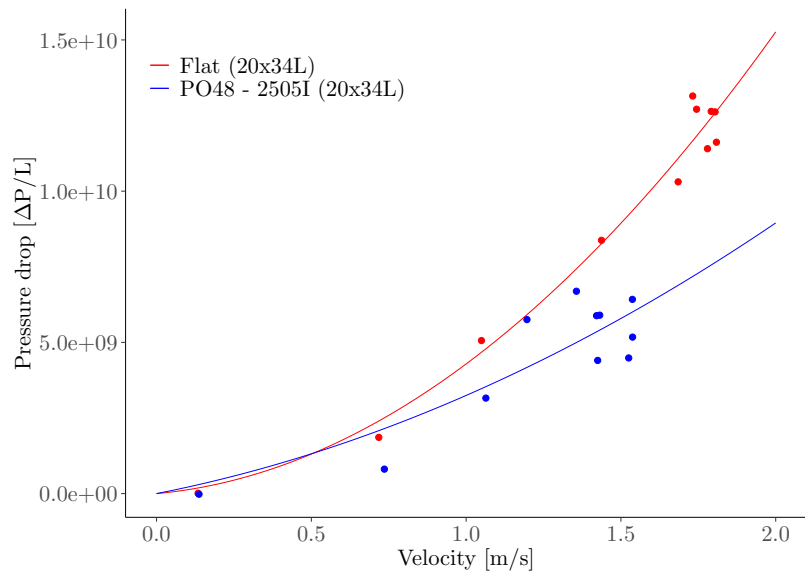


**Figure 4.2:** Comparison of the 34L flat and geometric weave, respectively shown as red and blue. Showing the predicted pressure-drop as determined using the Linear Regression Method. In addition, the relevant pressure-drop data is plotted in for each geometry.

Non-positive empirical constants does not meet the expectation of an increase in pressure drop with an increase in the flowrate, such that these values do not make sense. The remaining filters in the table, with only positive empirical constants, make sense in this regard, and match the data well given the high  $R^2$ -values that are greater than 95%.

In Figures 4.2–4.6 a comparison between the flat and shaped geometries for each weave is shown. These figures use the Forchheimer equation with the calculated empirical constants from Table 4.1, whilst also plotting the mean of the experimentally gathered pressure drops. Additionally, Figure 4.7 shows a graph of the pressure drop values for the XW2 filters in the filter house with a square and circular interior respectively. This figure also has the experimentally gathered pressure drop values plotted for both filters.



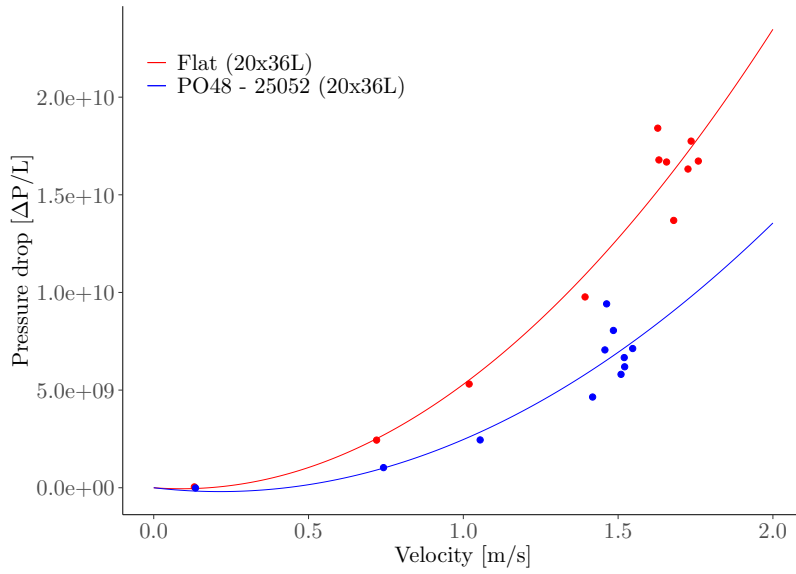


**Figure 4.3:** Comparison of the 36L flat and geometric weave, respectively shown as red and blue. Showing the predicted pressure-drop as determined using the Linear Regression Method. In addition, the relevant pressure-drop data is plotted in for each geometry.

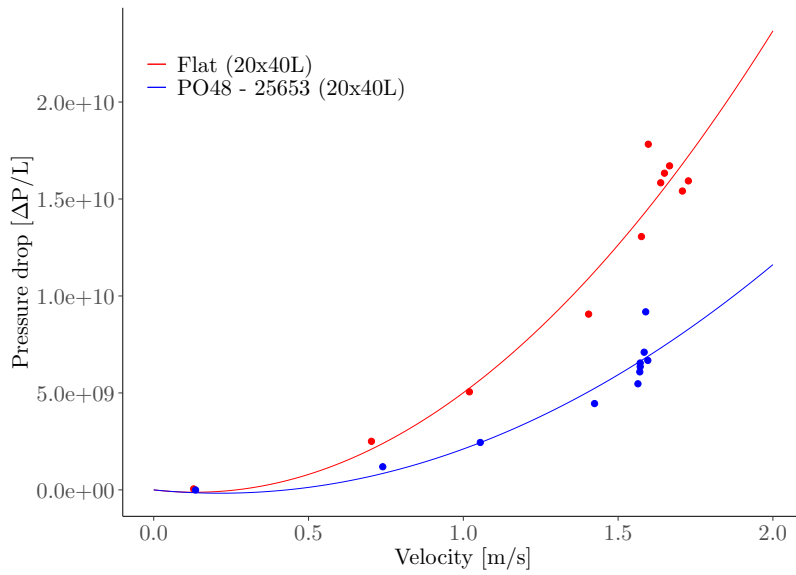


**Figure 4.4:** Comparison of the 40L flat and geometric weave, respectively shown as red and blue. Showing the predicted pressure-drop as determined using the Linear Regression Method. In addition, the relevant pressure-drop data is plotted in for each geometry.

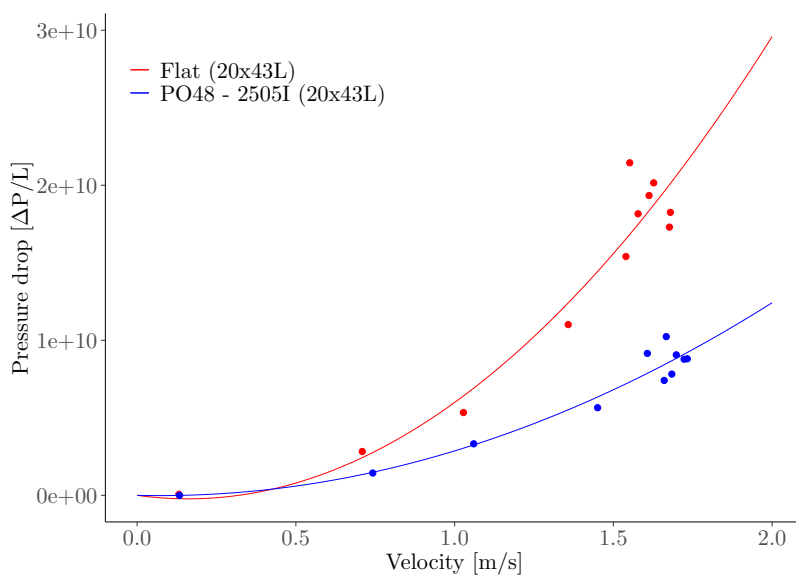


**Figure 4.5:** Comparison of the 43L flat and geometric weave, respectively shown as red and blue. Showing the predicted pressure-drop as determined using the Linear Regression Method. In addition, the relevant pressure-drop data is plotted in for each geometry.

**Figure 4.6:** Comparison of the XW2 flat and geometric weave, respectively shown as red and blue. Showing the predicted pressure-drop as determined using the Linear Regression Method. In addition, the relevant pressure-drop data is plotted in for each geometry.

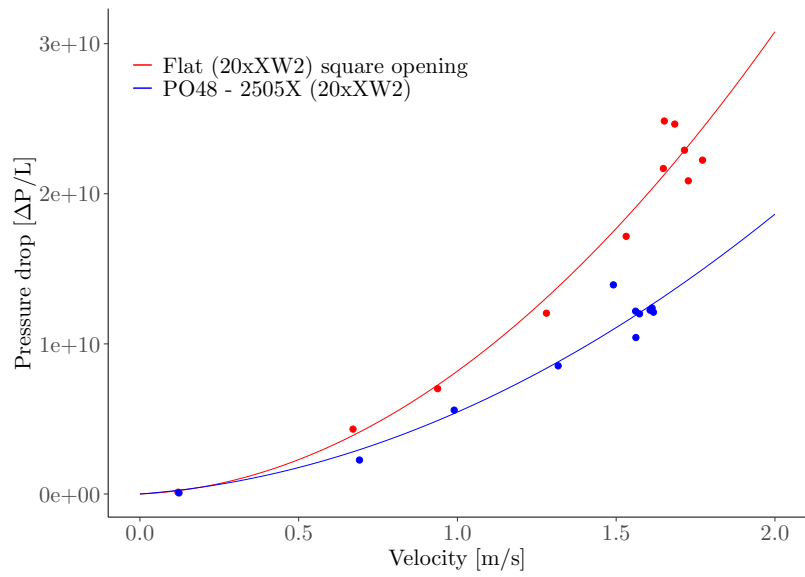
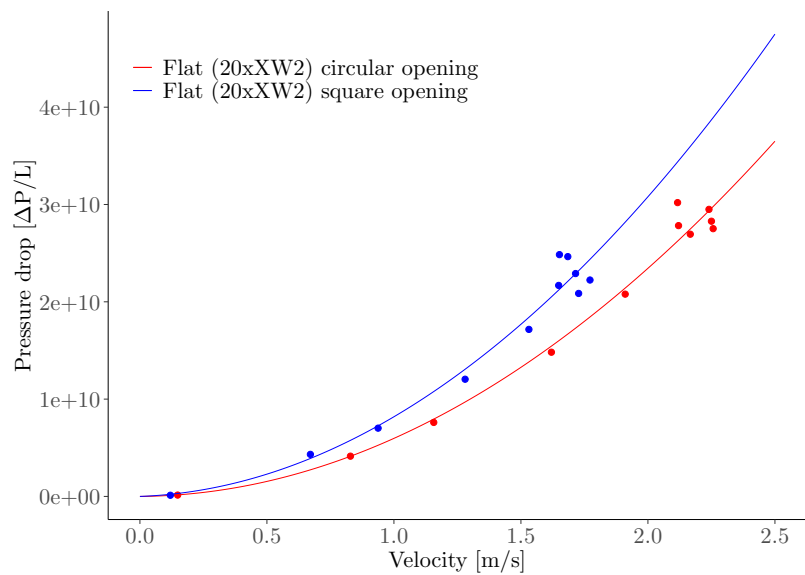


**Figure 4.7:** Comparing the square and circular interior for the filter house using the flat XW2 weave as a filter. The predicted pressure-drop with each opening is determined using the Linear Regression Method, where the circular and square opening are shown as red and blue respectively. Additionally the measured pressure-drop data is plotted in with the respective colors.



#### 4.1.4 The Second Regression Method: Ergun Method

In Table 4.2 the calculated empirical constants with the Empirical Ergun Method is shown. By comparing this table to Table 4.1, we can see that the filters with a corresponding negative  $k_1$ -value are reciprocated here, with an additional two negative  $k_1$ -values. Thus, this method has yielded less useful results compared with the Linear Regression, as opposed to the findings in [14]. Additionally, considering the  $R^2$ -values for the filters with a positive  $k_1$ -value, the  $R^2$ -value for the Linear Regression Method exceeds the ones found with this method. This discrepancy could be the result of the flowrates used in the experiment, where in this experiment was based in higher flowrates, and thus outside the region of linear pressure drop. This being that the Linear Regression Method is directly applied to a second order function, whilst the Empirical Ergun method first converts the second order equation to a first order one. Whilst this is a possible explanation for the discrepancy in the  $k_1$ -values where the Linear Regression Method gave a positive value, whilst this method gave a negative value, it is not an explanation for the filters that both method yielded a negative  $k_1$ -value for in and of itself. For these filters there may be two factors contributing to these values being negative, with the first factor being the flowrates that was used in the experiment, as mentioned. Whilst the second error could be minor errors in the initial pressure-drop data that was gathered. Minor fluctuations in the initial pressure-drop data would be able to influence the  $k_1$ -value sufficiently to give it a negative sign, in spite of the pressure-drop increasing. This is due to the data fitting nature of regression, where a negative linear coefficient would be able to match the data better than a positive one.

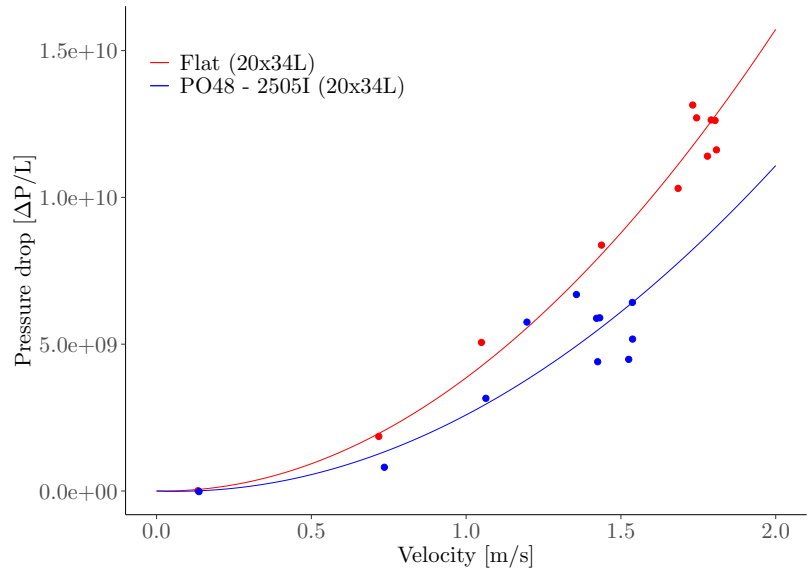
These calculated empirical constants are also graphically represented in figures, with the relevant pressure-drop data plotted in. These are Figures 4.8–4.13, where the first five figures compare the flat filters with their geometric counterparts, and the last figure compares the circular interior with the square interior using the flat XW2 weave as a filter.

Filter:	Ergun Empirical		
	$k_1$ :	$k_2$ :	$R^2$ :
Flat (20x34L)	-7.70e-12	2.50e-07	0.950
Flat (20x36L)	-1.40e-12	1.61e-07	0.923
Flat (20x40L)	-1.51e-12	1.63e-07	0.919
Flat (20x43L)	-8.95e-13	1.29e-07	0.889
Flat (20xXW2) square opening	2.13e-12	1.33e-07	0.930
Flat (20xXW2) circular opening	3.84e-11	1.71e-07	0.967
PO48 - 2505I (20x34L)	-3.17e-12	3.39e-07	0.677
PO48 - 25052 (20x36L)	-1.18e-12	2.71e-07	0.782
PO48 - 25653 (20x40L)	-1.79e-12	3.27e-07	0.860
PO48 - 25054 (20x43L)	-2.37e-12	2.99e-07	0.918
PO48 - 2505X (20xXW2)	4.93e-12	2.09e-07	0.902

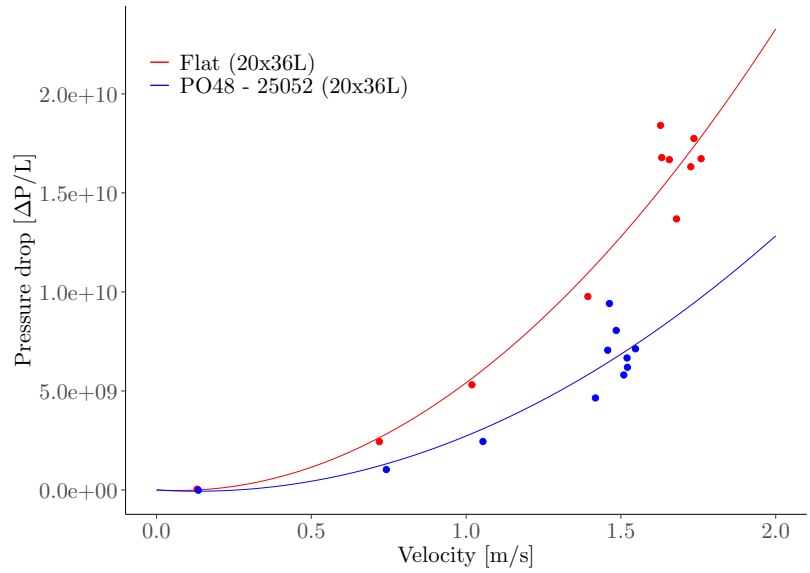
[14]: Zhang (2012), 'Liquid Permeability of Ceramic Foam Filters'

**Table 4.2:** The calculated empirical constants for each filter in regards to the Forchheimer equation, where the values are determined with the Ergun Empirical Method. The first six rows show the flat weaves, whilst the last five show the geometric weaves. And the following three columns shows the  $k_1$ ,  $k_2$  and  $R^2$ -values.

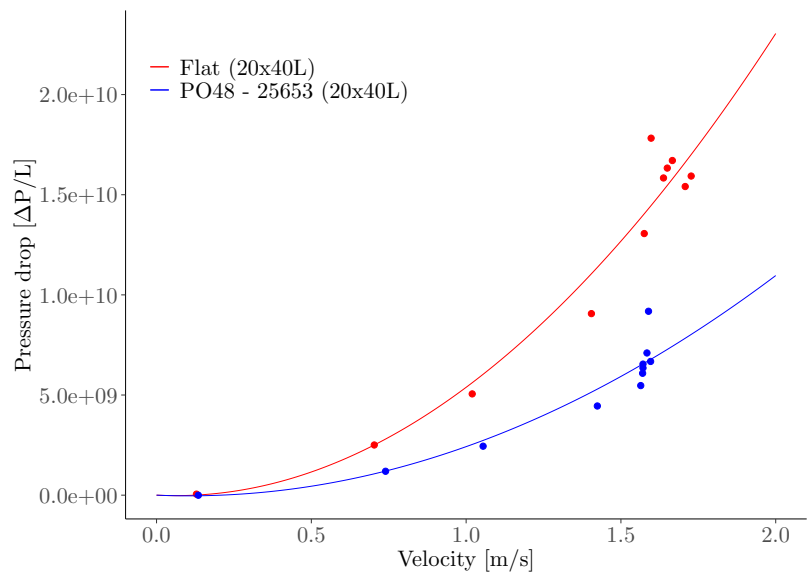
**Figure 4.8:** Comparison of the 34L flat and geometric weave, respectively shown as red and blue. Showing the predicted pressure-drop as determined using the Ergun Empirical Method. In addition, the relevant pressure-drop data is plotted in for each geometry.



**Figure 4.9:** Comparison of the 36L flat and geometric weave, respectively shown as red and blue. Showing the predicted pressure-drop as determined using the Ergun Empirical Method. In addition, the relevant pressure-drop data is plotted in for each geometry.



**Figure 4.10:** Comparison of the 40L flat and geometric weave, respectively shown as red and blue. Showing the predicted pressure-drop as determined using the Ergun Empirical Method. In addition, the relevant pressure-drop data is plotted in for each geometry.



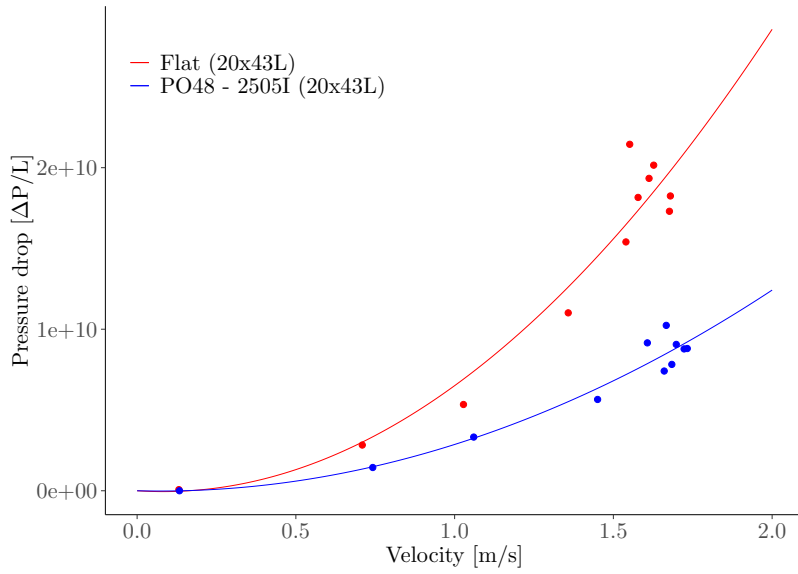


**Figure 4.11:** Comparison of the 43L flat and geometric weave, respectively shown as red and blue. Showing the predicted pressure-drop as determined using the Ergun Empirical Method. In addition, the relevant pressure-drop data is plotted in for each geometry.

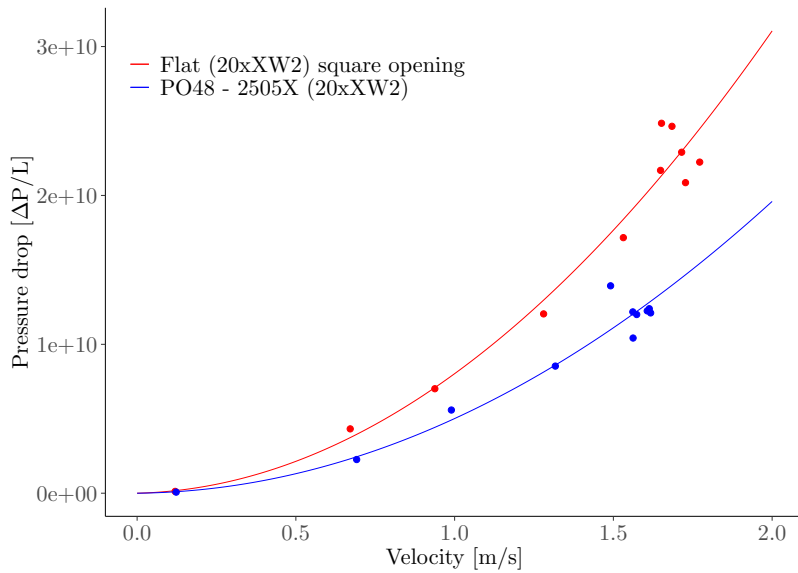


**Figure 4.12:** Comparison of the XW2 flat and geometric weave, respectively shown as red and blue. Showing the predicted pressure-drop as determined using the Ergun Empirical Method. In addition, the relevant pressure-drop data is plotted in for each geometry.

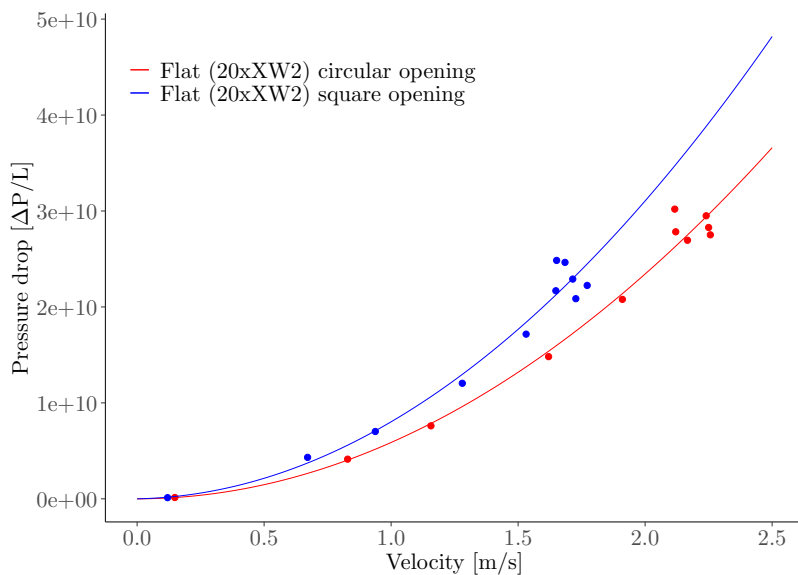


**Figure 4.13:** Comparing the square and circular interior for the filter house using the flat XW2 weave as a filter. The predicted pressure-drop with each opening is determined using the Ergun Empirical Method, where the circular and square opening are shown as red and blue respectively. Additionally, the measured pressure-drop data is plotted in with the respective colors.

**Table 4.3:** The calculated exponents using the third method for determining the empirical constants for the Forchheimer equation. This table shows the exponent for the second order velocity, where this value ideally should be 2.

Filters:	Exponents:
Flat (20x34L)	2.005
Flat (20x36L)	2.321
Flat (20x40L)	2.237
Flat (20x43L)	2.241
Flat (20xXW2) square opening	2.000
Flat (20xXW2) circular opening	2.000
PO48 - 2505I (20x34L)	2.444
PO48 - 25052 (20x36L)	2.721
PO48 - 25653 (20x40L)	2.319
PO48 - 25054 (20x43L)	2.166
PO48 - 2505X (20xXW2)	2.009

### 4.1.5 The Third Regression Method: Exponential Regression

Table 4.4 shows the determined empirical constants for the Forchheimer equation using the Exponential Regression. The determined exponents in this regression can be viewed in Table 4.3, where not all the exponents are 2, as they ideally should be. These exponents are as close to this value as they could be managed with this method. This deviance from the ideal value for the exponent indicates errors in the pressure-drop data that the values deviate from a second order curve. Further, this deviance in the exponents corroborate the possibility of an error in these measurements, as was discussed in section 4.1.4. However, the  $k_1$ - and  $k_2$ -values determined with this method constitute the best guess for the filters that the earlier two methods yielded a negative  $k_1$ -value for.

Both the  $k_1$ - and  $k_2$ -values that were determined using this method was positive. This is as expected, where the constraint of the method forces  $k_1$  to be positive, whilst the  $k_2$ -value is calculated using logarithms. A noteworthy aspect of the determined  $k_2$ -values, are that they are on the same order of magnitude as their counterparts with the previous two methods. This indicates that the exponential term outweighs the linear term in the expression, and thus the  $k_2$ -values can be assumed to be of a higher reliability compared to the  $k_1$ -values.

These empirical values are also represented graphically in Figures 4.14–4.19, where the relevant experimentally gathered pressure-drop data is also plotted in. In the first five of these figures, the pressure-drop is compared across geometries for each filter weave, whilst the last figure compares the square and circular interior for the filter house using the flat XW2 weave as a filter.

**Table 4.4:** The calculated empirical constants for each filter in regards to the Forchheimer equation, where the values are determined with the Exponential Regression Method. The first six rows show the flat weaves, whilst the last five show the geometric weaves. And the following three columns shows the  $k_1$ ,  $k_2$  and  $R^2$ -values.

Filter:	Exponential Method		
	$k_1$ :	$k_2$ :	$R^2$ :
Flat (20x34L)	1.27e-11	2.59e-07	0.979
Flat (20x36L)	3.34e-08	2.04e-07	0.997
Flat (20x40L)	3.28e-08	1.98e-07	0.996
Flat (20x43L)	6.29e-08	1.63e-07	0.994
Flat (20xXW2) square opening	8.80e-12	1.28e-07	0.996
Flat (20xXW2) circular opening	1.69e-11	1.72e-07	0.999
PO48 - 2505I (20x34L)	3.75e-08	4.36e-07	0.805
PO48 - 25052 (20x36L)	3.69e-08	4.41e-07	0.922
PO48 - 25653 (20x40L)	2.74e-08	4.39e-07	0.950
PO48 - 25054 (20x43L)	1.37e-07	3.57e-07	0.970
PO48 - 2505X (20xXW2)	3.47e-07	2.03e-07	0.996

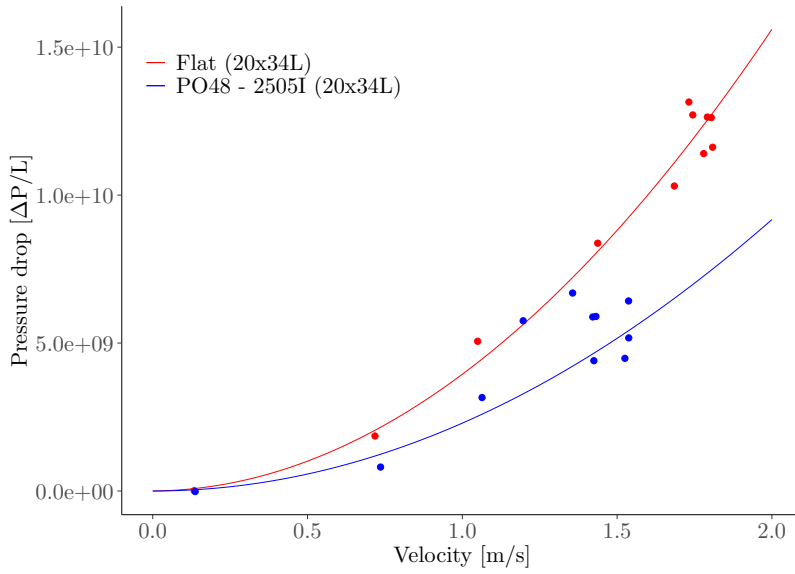


**Figure 4.14:** Comparison of the 34L flat and geometric weave, respectively shown as red and blue. Showing the predicted pressure-drop as determined using the Exponential Regression Method. In addition, the relevant pressure-drop data is plotted in for each geometry.

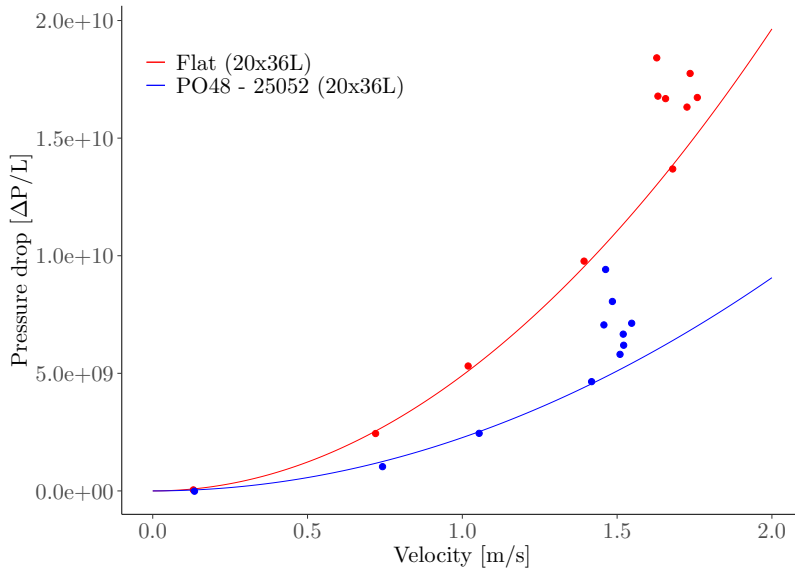


**Figure 4.15:** Comparison of the 36L flat and geometric weave, respectively shown as red and blue. Showing the predicted pressure-drop as determined using the Exponential Regression Method. In addition, the relevant pressure-drop data is plotted in for each geometry.

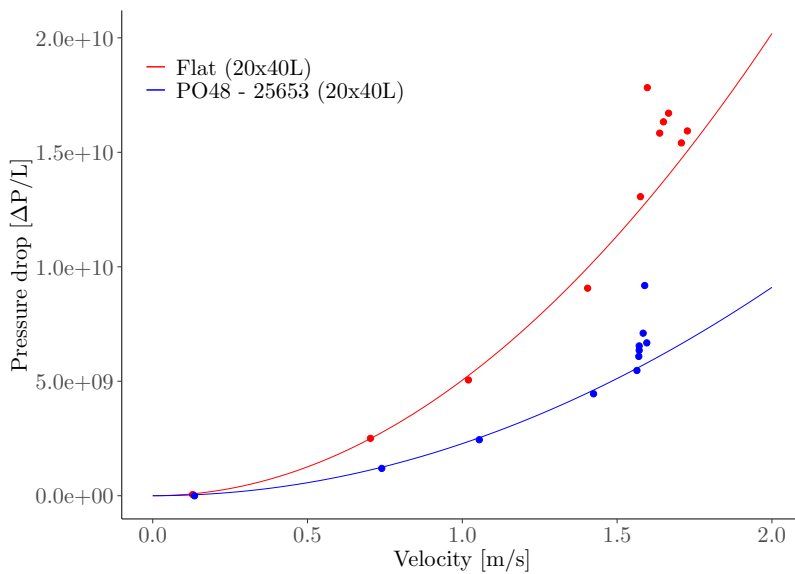


**Figure 4.16:** Comparison of the 40L flat and geometric weave, respectively shown as red and blue. Showing the predicted pressure-drop as determined using the Exponential Regression Method. In addition, the relevant pressure-drop data is plotted in for each geometry.

**Figure 4.17:** Comparison of the 43L flat and geometric weave, respectively shown as red and blue. Showing the predicted pressure-drop as determined using the Exponential Regression Method. In addition, the relevant pressure-drop data is plotted in for each geometry.

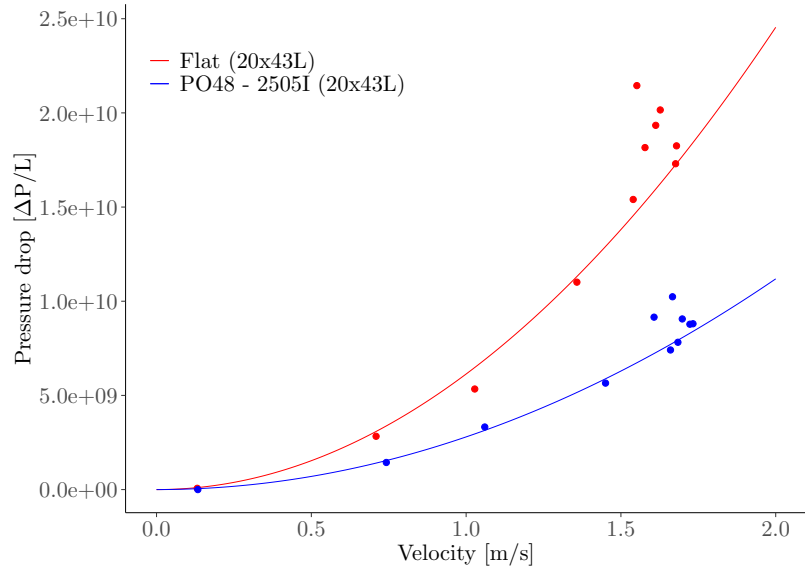


**Figure 4.18:** Comparison of the XW2 flat and geometric weave, respectively shown as red and blue. Showing the predicted pressure-drop as determined using the Exponential Regression Method. In addition, the relevant pressure-drop data is plotted in for each geometry.

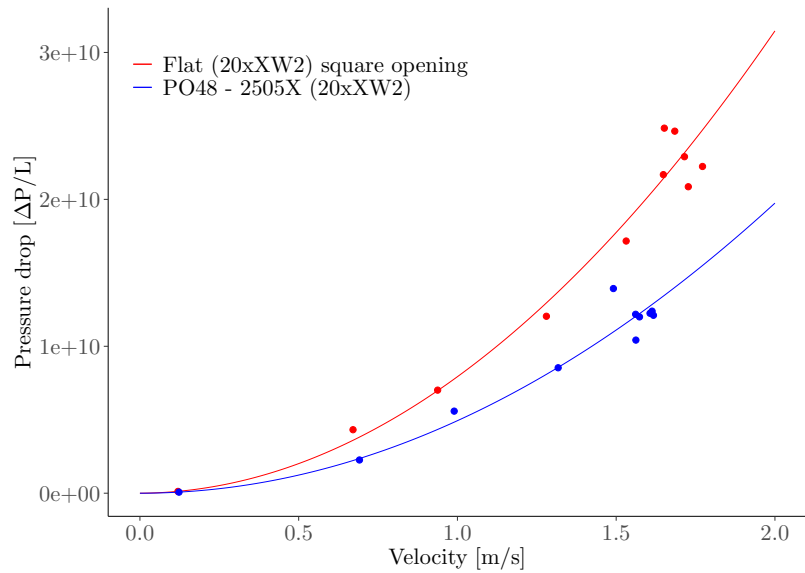
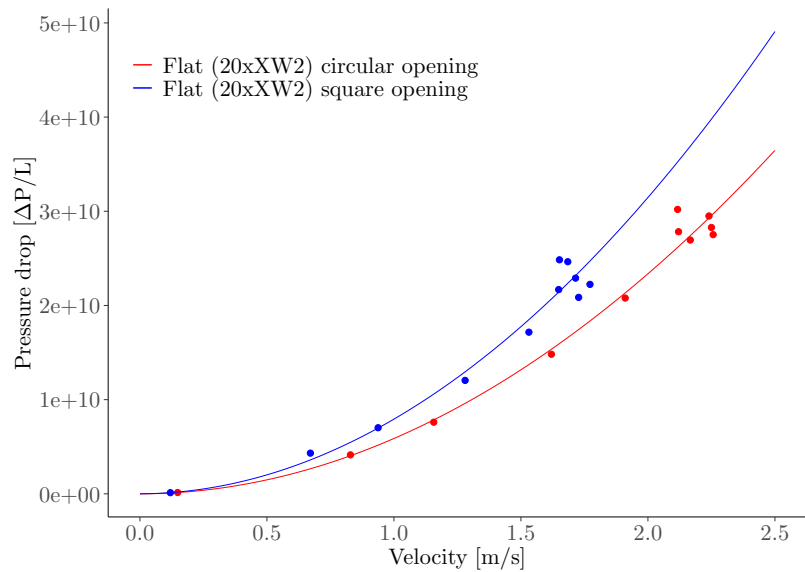


**Figure 4.19:** Comparing the square and circular interior for the filter house using the flat XW2 weave as a filter. The predicted pressure-drop with each opening is determined using the Exponential Regression Method, where the circular and square opening are shown as red and blue respectively. Additionally the measured pressure-drop data is plotted in with the respective colors.





#### 4.1.6 Utilization of Brute Force

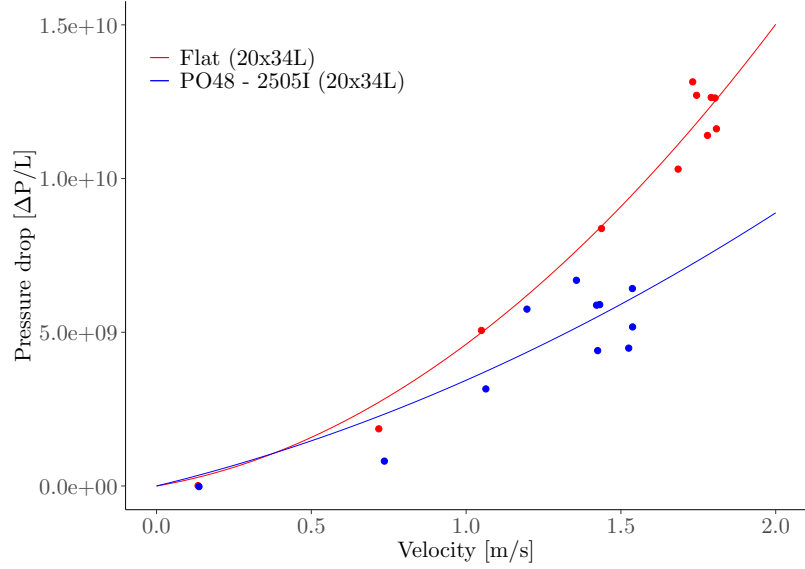
In comparison with the three previous methods, this method does not utilize regression. In this method the  $R^2$  is calculated as in a linear regression, forced through the origin. And with the constraints placed upon this method, the determined values of the empirical constants for the Forchheimer equation are the most reliable. These values can be seen in 4.5, where it can be noted that all the  $k_1$ -values and  $k_2$ -values are on the same order of magnitude. Whilst the empirical constants are the most reliable, that is not to say that they are correct. In particular the method by which these constants are determined artificially reduces the value of  $k_1$ , such that the predicted pressure-drop due to the linear term is maximized. Due to this, it is reasonable to believe that the  $k_1$ -value may be greater than the value provided in Table 4.5. This is consistent with the earlier methods resulting  $k_1$ -values, where a higher proportion of high flowrate pressure-drop values and the fact that the Forchheimer equation is of the second order, could lead to the  $k_2$ -value overshadowing the  $k_1$ -value. The determined  $k_2$ -values from all the methods yielding values on the same order of magnitude corroborate this notion. Considering this, a better approach to determining these constants may be to include a greater amount of low flowrate water trial. Alternatively, two experiments could be performed: one at lower flowrates solely to determine  $k_1$ , and one with higher flowrates to determine  $k_2$ , where  $k_2$  would be determined using  $k_1$ .

The empirical constants, as determined with this method, are graphically represented in Figures 4.20–4.25, where the relevant pressure-drop data is plotted in. Of these figures, the first five compare the pressure drop based on each weaves geometry. And the last figure compares the pressure-drop for the square and circular interior of the filter house, using the flat XW2 weave as a filter.

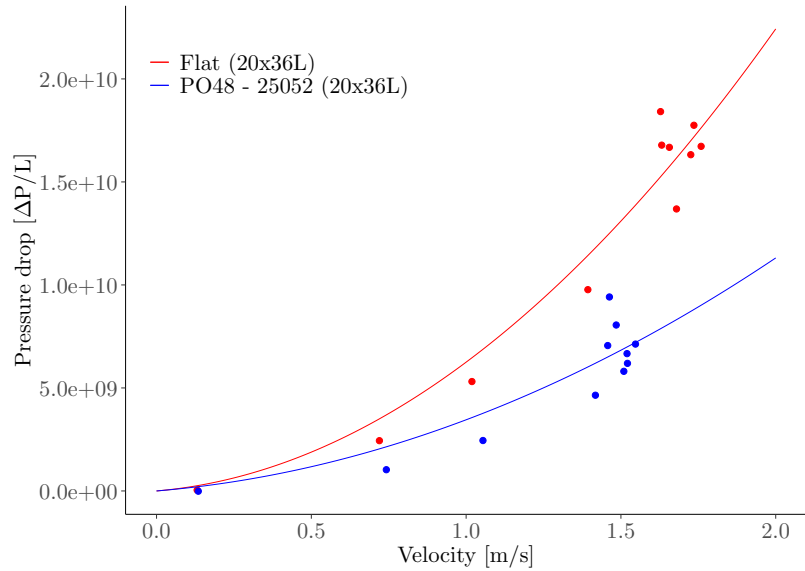
Filter:	Brute Force		
	$k_1$ :	$k_2$ :	$R^2$ :
Flat (20x34L)	6.64e-13	3.45e-07	0.995
Flat (20x36L)	8.82e-13	2.02e-07	0.988
Flat (20x40L)	6.41e-13	2.17e-07	0.987
Flat (20x43L)	6.27e-13	1.71e-07	0.982
Flat (20xXW2) square opening	3.42e-13	1.73e-07	0.991
Flat (20xXW2) circular opening	4.38e-13	2.16e-07	0.995
PO48 - 2505I (20x34L)	4.67e-13	9.96e-07	0.955
PO48 - 25052 (20x36L)	9.08e-13	4.54e-07	0.956
PO48 - 25653 (20x40L)	8.89e-13	5.45e-07	0.971
PO48 - 25054 (20x43L)	8.48e-13	4.47e-07	0.986
PO48 - 2505X (20xXW2)	3.36e-13	3.70e-07	0.989

**Table 4.5:** The calculated empirical constants for each filter in regards to the Forchheimer equation, where the values are determined with the Brute Force Method. The first six rows show the flat weaves, whilst the last five show the geometric weaves. And the following three columns shows the  $k_1$ ,  $k_2$  and  $R^2$ -values.

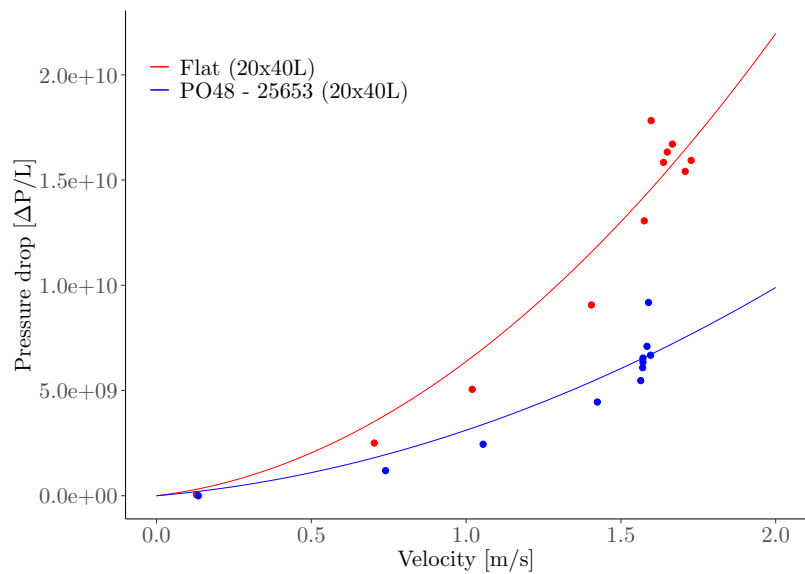
**Figure 4.20:** Comparison of the 34L flat and geometric weave, respectively shown as red and blue. Showing the predicted pressure-drop as determined using the Brute Force Method. In addition, the relevant pressure-drop data is plotted in for each geometry.



**Figure 4.21:** Comparison of the 36L flat and geometric weave, respectively shown as red and blue. Showing the predicted pressure-drop as determined using the Brute Force Method. In addition, the relevant pressure-drop data is plotted in for each geometry.



**Figure 4.22:** Comparison of the 40L flat and geometric weave, respectively shown as red and blue. Showing the predicted pressure-drop as determined using the Brute Force Method. In addition, the relevant pressure-drop data is plotted in for each geometry.



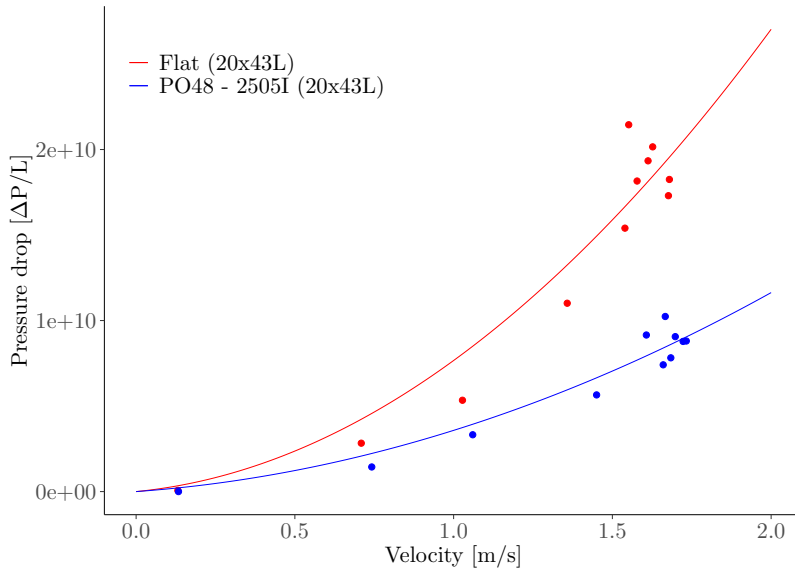


**Figure 4.23:** Comparison of the 43L flat and geometric weave, respectively shown as red and blue. Showing the predicted pressure-drop as determined using the Brute Force Method. In addition, the relevant pressure-drop data is plotted in for each geometry.

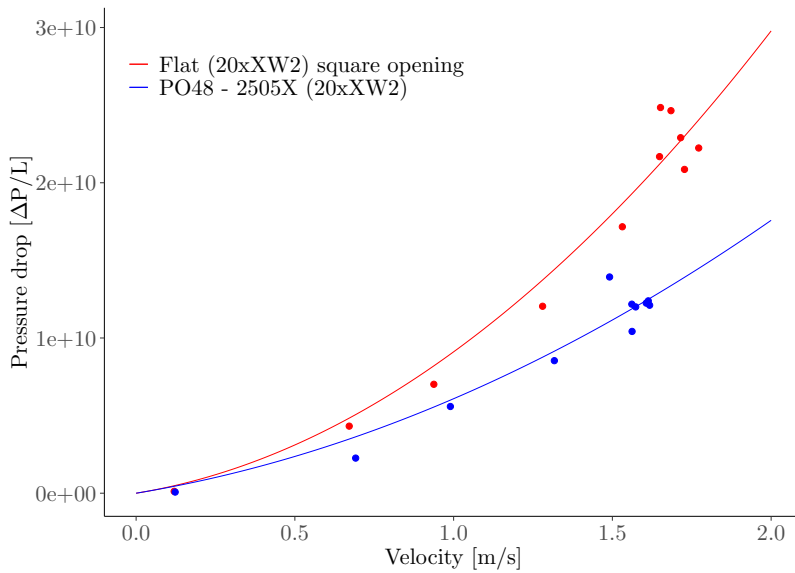


**Figure 4.24:** Comparison of the XW2 flat and geometric weave, respectively shown as red and blue. Showing the predicted pressure-drop as determined using the Brute Force Method. In addition, the relevant pressure-drop data is plotted in for each geometry.

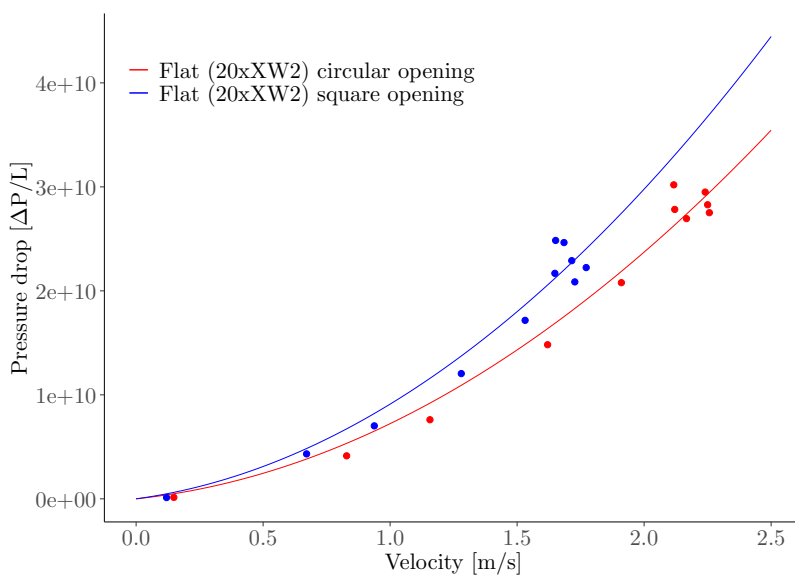


**Figure 4.25:** Comparing the square and circular interior for the filter house using the flat XW2 weave as a filter. The predicted pressure-drop with each opening is determined using the Brute Force Method, where the circular and square opening are shown as red and blue respectively. Additionally the measured pressure-drop data is plotted in with the respective colors.

### 4.1.7 In Regard to all Three Regression Methods

Every determined empirical constant in regards to the Forchheimer equation can be seen in Table 4.6, where each of these values are separated according to the method used. This table shows that every determined  $k_2$ -value is on the same order of magnitude, and that the same does not hold for the  $k_1$ -value, where the Brute Force Method yielded the smallest values. In addition to this, Figure 4.26 and 4.27 compares the predicted pressure-drops for the flat and geometric weaves respectively, and the relevant pressure-drop measurements are plotted in. These figures are made using the empirical values from the Brute Force Method, where the bias in the  $k_1$ -values are visible, as all the predicted pressure-drop values exceed the measured ones for every weave in the lower flowrates.

In both these figures, the different weaves have the same relative arrangement for their predicted pressure-drop. This arrangement is in the following ascending order for the predicted pressure-drop: 34L, 40L, 36L, 43L and XW2. As can be seen in the figures, the variance of the measured pressure-drop values for the different weaves overlap with each other. And coupled with the fact that every combination of weave and geometry was only measured across five parallels, the resulting determined empirical constants cannot be considered to be statistically significant. Thus the arrangement found in the figures can be the result of chance, where the actual relative pressure-drops of the weaves may be different. Additionally, the weaves in the middle of this arrangement are the ones that yielded a negative  $k_1$ -value for the first two methods. And for this reason have a higher uncertainty in their relative placements. In Table 4.6, it this pattern is not consistent for every method and geometry, by considering the  $k_2$ -values.

Using the Brute Force Method as the expected empirical constants, we can calculate the p-values for the empirical constants as determined by the other methods. This is done for the Linear Regression Method and the Ergun Empirical Method, where these p-values are shown for each of the empirical constants respectively in Table 4.7. The p-values are calculated using the coefficients determined in the regression and nine degrees of freedom, and are one sided relative to the sign in the t-test. Based on this assumption, only the constants determined by the Ergun Empirical Method supersede the constants determined by the Brute Force Method using a 95% confidence interval.

**Table 4.6:** Every determined empirical constant for the Forchheimer equation for the RGW used in the pressure-drop experiment. The first six rows show the flat weaves, while the last five rows show the geometric weaves. The following twelve columns are subdivided for each of the four methods used to determine the empirical constants. For each of these subdivisions the columns show the determined  $k_1$ ,  $k_2$  and  $R^2$ -values respectively.

Filter:	Linear Regression			Ergun Empirical			Exponential Method			Brute Force		
	$k_1$ :	$k_2$ :	$R^2$ :	$k_1$ :	$k_2$ :	$R^2$ :	$k_1$ :	$k_2$ :	$R^2$ :	$k_1$ :	$k_2$ :	$R^2$ :
Flat (20x34L)	1.21e-12	2.99e-07	0.995	-7.70e-12	2.50e-07	0.950	1.27e-11	2.59e-07	0.979	6.64e-13	3.45e-07	0.995
Flat (20x36L)	-9.90e-13	1.55e-07	0.989	-1.40e-12	1.61e-07	0.923	3.34e-08	2.04e-07	0.997	8.82e-13	2.02e-07	0.988
Flat (20x40L)	-6.27e-13	1.47e-07	0.989	-1.51e-12	1.63e-07	0.919	3.28e-08	1.98e-07	0.996	6.41e-13	2.17e-07	0.987
Flat (20x43L)	-4.04e-13	1.14e-07	0.984	-8.95e-13	1.29e-07	0.889	6.29e-08	1.63e-07	0.994	6.27e-13	1.71e-07	0.982
Flat (20xXW2) square opening	1.17e-12	1.39e-07	0.991	2.13e-12	1.33e-07	0.930	8.80e-12	1.28e-07	0.996	3.42e-13	1.73e-07	0.991
Flat (20xXW2) circular opening	5.45e-12	1.74e-07	0.995	3.84e-11	1.71e-07	0.967	1.69e-11	1.72e-07	0.999	4.38e-13	2.16e-07	0.995
PO48 - 25051 (20x34L)	5.64e-13	8.13e-07	0.955	-3.17e-12	3.39e-07	0.677	3.75e-08	4.36e-07	0.805	4.67e-13	9.96e-07	0.955
PO48 - 25052 (20x36L)	-6.18e-13	2.32e-07	0.962	-1.18e-12	2.71e-07	0.782	3.69e-08	4.41e-07	0.922	9.08e-13	4.54e-07	0.956
PO48 - 25653 (20x40L)	-7.16e-13	2.70e-07	0.977	-1.79e-12	3.27e-07	0.860	2.74e-08	4.39e-07	0.950	8.89e-13	5.45e-07	0.971
PO48 - 25054 (20x43L)	-2.38e-12	2.99e-07	0.988	-2.37e-12	2.99e-07	0.918	1.37e-07	3.57e-07	0.970	8.48e-13	4.47e-07	0.986
PO48 - 2505X (20xXW2)	7.13e-13	2.59e-07	0.989	4.93e-12	2.09e-07	0.902	3.47e-07	2.03e-07	0.996	3.36e-13	3.70e-07	0.989

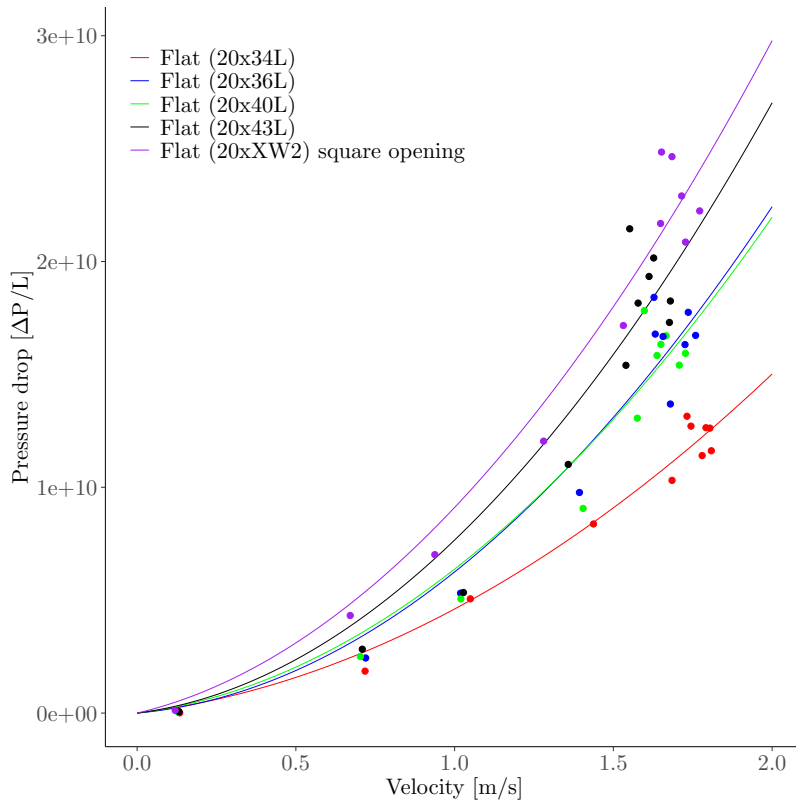


**Figure 4.26:** A comparison of the predicted pressure-drop with the Brute Force Method for the different weaves used in this experiment, with a flat geometry. Here the lines represent the predicted pressure-drop, while the points represent the measured pressure drops. The different weaves are represented by different colors: 20x34L, Red; 20x36L, Blue; 20x40L, Green; 20x43L, Black, and 20xXW2, Purple.

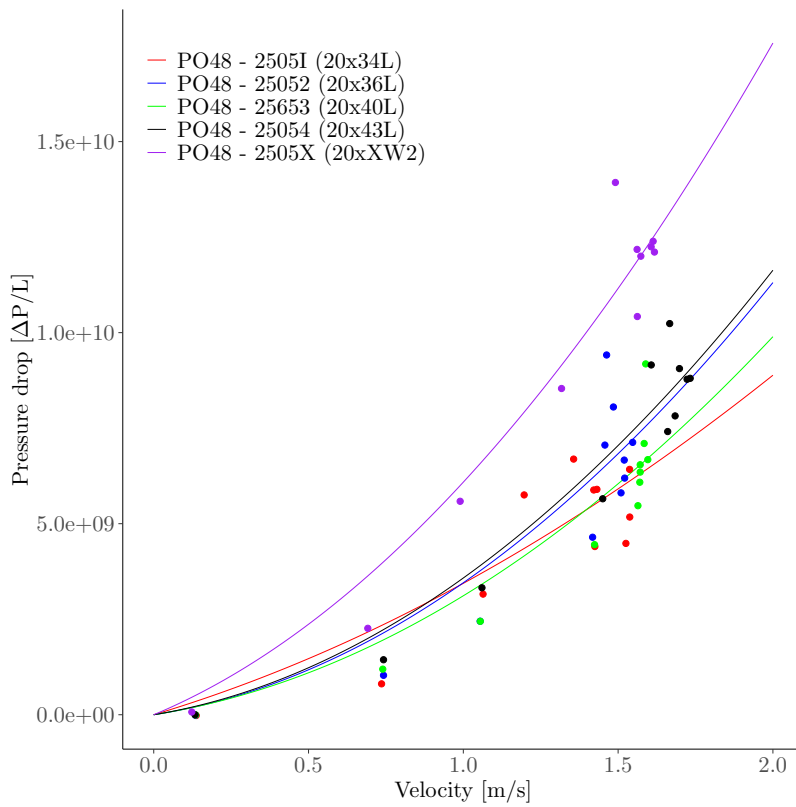


**Figure 4.27:** A comparison of the predicted pressure-drop with the Brute Force Method for the different weaves used in this experiment, with a shaped geometry. Here the lines represent the predicted pressure-drop, while the points represent the measured pressure drops. The different weaves are represented by different colors: 20x34L, Red; 20x36L, Blue; 20x40L, Green; 20x43L, Black, and 20xXW2, Purple.

**Table 4.7:** The calculated p-values for the empirical constants determined by the Linear Regression Method and the Ergun Empirical Method. These p-values use the calculated empirical constants for the Brute Force Method as the assumed null hypothesis.

Filter:	Linear Regression		Ergun Empirical	
	$k_1$ :	$k_2$ :	$k_1$ :	$k_2$ :
Flat (20x34L)	0.2715	0.2742	0.00153	0.00274
Flat (20x36L)	0.1805	0.1830	0.01982	0.03189
Flat (20x40L)	0.0901	0.0927	0.00870	0.01604
Flat (20x43L)	0.1116	0.1134	0.01993	0.03259
Flat (20xXW2) square opening	0.2113	0.2149	0.00988	0.01717
Flat (20xXW2) circular opening	0.2113	0.2149	0.00988	0.01717
PO48 - 2505I (20x34L)	0.4232	0.4416	0.00533	0.00925
PO48 - 25052 (20x36L)	0.1307	0.1328	0.01526	0.02392
PO48 - 25653 (20x40L)	0.0669	0.0686	0.00417	0.00770
PO48 - 25054 (20x43L)	0.1235	0.1264	0.00234	0.00443
PO48 - 2505X (20xXW2)	0.1235	0.1264	0.00234	0.00443

#### 4.1.8 The Pressure-Drop Results of the Ceramic Foam Filters

In addition to the measurements of the RGW, two CFF filters were measured in the pressure-drop experiment. This was  $Al_2O_3$  CFF filters at 10 and 20 ppi. The empirical constants in regards to the Forchheimer equation was determined using the Linear Regression Method. The determined  $k_1$ -values were  $-5.65e-12$  and  $-1.41e-12$  respectively for the 10 and 20 ppi CFF filters. Additionally the determined  $k_2$ -values were  $1.39e-06$  and  $3.46e-07$  respectively for the 10 and 20 ppi CFF filters. In Figure 4.28 a comparison between these two CFF filters is shown, where the 20 ppi filter has a higher pressure drop than the 10 ppi filter.

A comparison between the CFF filters and the RGW with the highest pressure-drop is shown in Figure 4.29. Here, both the CFF filters and the flat XW2 weave are graphed using the determined empirical constants from the Linear Regression Method, and the relevant measured pressure-drop values are plotted in. In this figure we can see that the predicted pressure-drop is highest for the flat XW2 weave, and this is likely due to the difference in the thickness. This difference in the thickness between these CFF filters and the RGW are at a factor of  $\sim 2000$ . And as such the flat XW2 weave can be expected to have a smaller total pressure-drop compared with these CFF filters.

Additionally, the measured pressure-drop values for the RGW appear to have a tendency to gather at the higher flowrates, which is apparent in Figure 4.26 and 4.27. Where this tendency was previously attributed to the constraint experienced by the tube intermedating the primary tank and primary pump, see Figure 4.1. This tendency does not seem to be reciprocated for the CFF, as seen in Figure 4.28, where the measured pressure-drop values appear to be placed at more even flowrate intervals. It is possible that the higher total pressure-drop from the CFF also constrain the flow, which leads to a more even flowrate intervals in the pressure-drop measurements. And as such, the placements of the measured pressure-drop values corroborate the notion of the CFF yielding higher total pressure-drops in comparison to the RGW further.

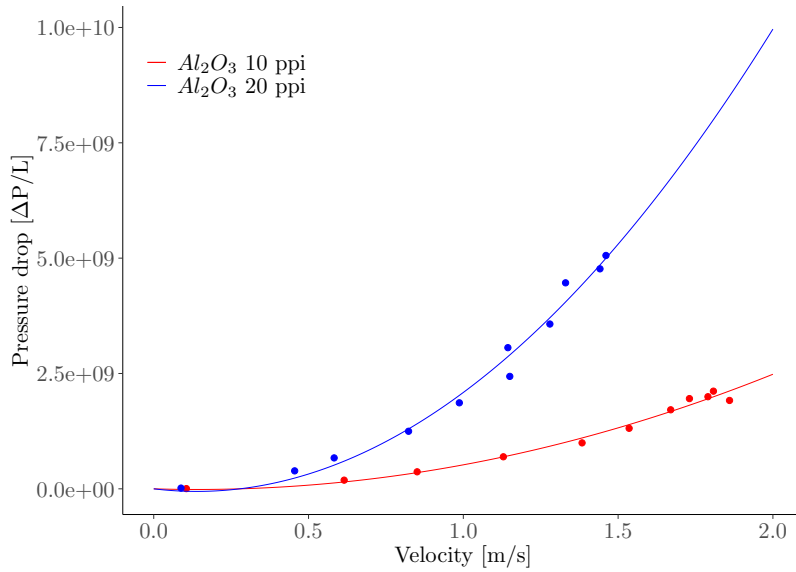


**Figure 4.28:** A graph of both the CFF filters measured in the pressure-drop experiment. Where the blue and red lines were graphed using the regressed values for  $Al_2O_3$  at 10 and 20 ppi respectively, using the Linear Regression Method. The plotted values are the measured pressure-drop values, and their colors correspond to the same of the lines.

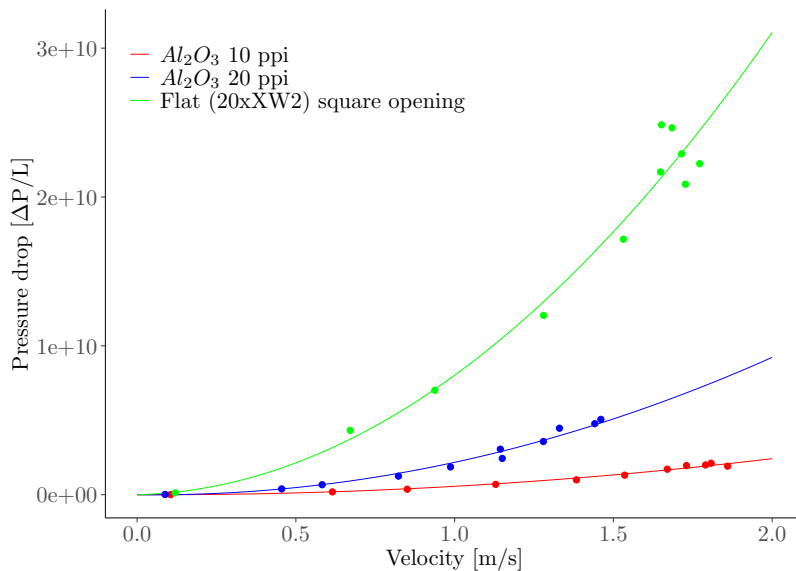


**Figure 4.29:** Comparison between the CFF filters and the Flat XW2 weave using the square interior. Here the blue and red line respectively represent  $Al_2O_3$  at 10 and 20 ppi, while the green line represents the Flat XW2 weave. All the lines are graphed using the Linear Regression Method, and have their respective pressure-drop measurements plotted in with the same colors.

## 4.2 Sand Casting and Scanning Electron Microscopy

Figures 4.30–4.32 shows results of sand casted aluminium through the geometrical rigid glass weave filters. All the samples for SEM were casted successfully and could directly be used further processing, such as cutting and polishing. Nevertheless, due to too low casting temperature and too little metal for the sand casting, an unsuccessful casting trial did occur, as shown in Figure 4.31 and Figure 4.32. The metal in this casting was not able to penetrate the filter, and in Figure 4.31 where it did, the metal set before fully submerging the filter. This metal trial was repeated with appropriate casting temperature and amount of metal. For the two successful castings that were done, the metal was heated until 840°C and 915°C, respectively. The metal was then set for cooling overnight. Following this, the casting were cut along their middle axis, and these images can be seen in Appendix B.



**Figure 4.30:** Successful casting of metal. The molten metal was able to penetrate the weaves and fully submerge the filter before solidification.

**Figure 4.33:** Filters (1) before and (2) metallographic sample preparation of PO48 - 25051 (20x34L).

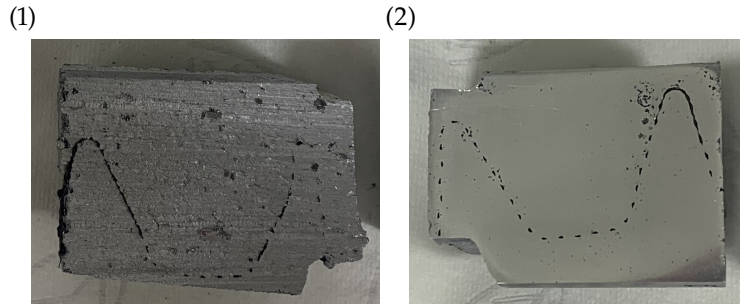


**Figure 4.31:** An unsuccessful casting of metal. The molten metal was able to penetrate the weaves but solidified before fully submerging the filter.

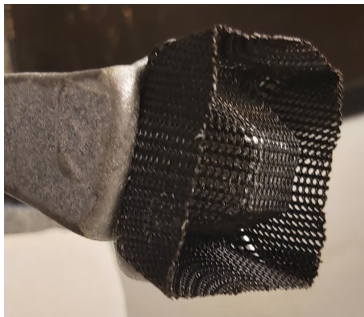


**Figure 4.32:** An unsuccessful casting of metal. The molten metal was not able to penetrate the weaves and solidified.

In Figure 4.34 four SEM image of the weaves are shown: (1), the 34L weave; (2), the 36L weave; (3), the 40L weave, and (4), the 43L weave. The first three images in this figure shows the presence of grains in the castings, which can have mixed in during the casting, mixing with the liquid aluminium alloy and making a heterogeneous solution. Such a grain is shown most prominently in image (3), where it is present in the middle of the top and in the middle of the right part of the image. In both instances the grain is placed inside a cavity in the metal. In addition to the cavities, the aluminium alloy experienced additional forms of casting shrinkage. This being primarily visible as the cavities in image (2) and the fractures in (4), as well as the space intermediated by the weaves. All the images shows the weave surviving the casting process and remain intact, indicating that they are able to withstand the heat and bypass of the molten metal. Two aspects of the weaves structure can be seen in these images, where (1) and (3) shows a cross section of the strands individually, while (2) and (4) shown the intersection of the orthogonal weaves. The individual strands are visible in all the images, appearing to not be wetted by the metal. Although, image (3) and (4) shows wetting at the interface between the weave and the metal. Surrounding the weaves, dark regions are visible in image (1), (2) and (4). These dark regions can be attributed to the ethanol used to clean the samples, as these regions varied in size during imaging. It is likely that some of the ethanol permeated into the vacant area surrounding the weaves. Additionally, lighter regions can be seen in all of the images, which are most prominent in (3) and (4). These lighter regions may be phases in the solidified aluminium alloy. Further SEM images are shown in Appendix C.



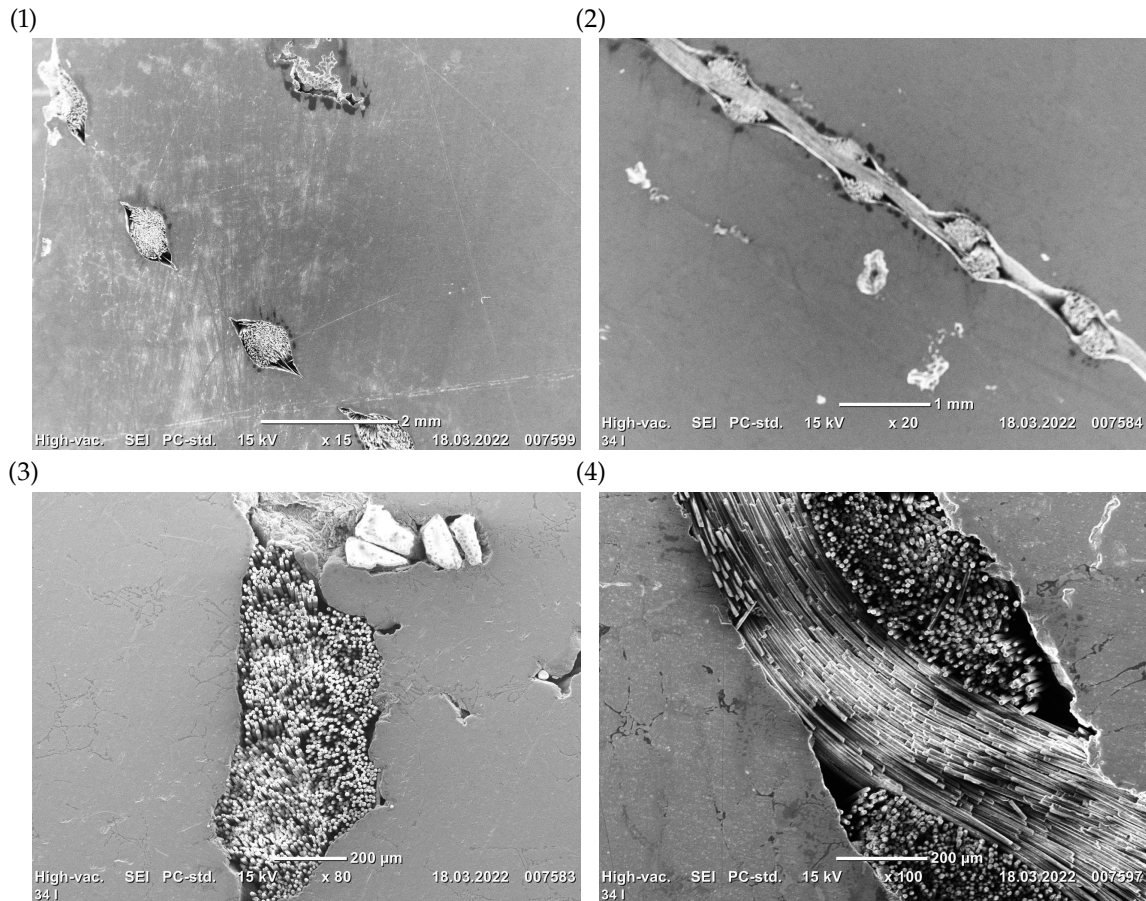
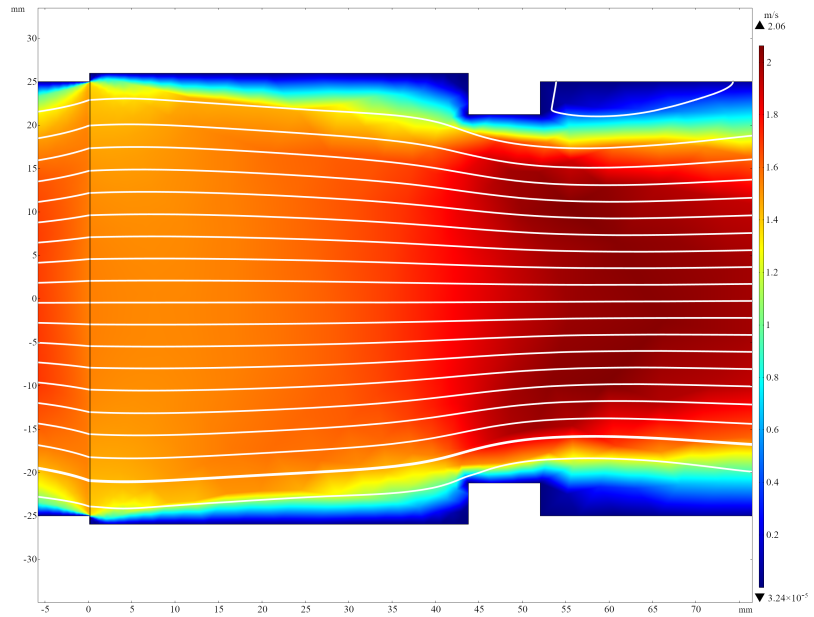


**Figure 4.34:** SEM pictures of the samples: (1) Weave structure and casting shrinkage in sample of 20x40L (Zoom = x15), (2) Weave structure and casting shrinkages in sample of 20x43L (Zoom = x20), (3) Lodged sand grains, weave structure and casting shrinkage in sample of 20x34L (Zoom = x80), and (4) Weave structure and some form of casting shrinkage in sample of 20x36L (Zoom = x100). (SEI, High-Vacuum.)

### 4.3 COMSOL Multiphysics® Modelling

Regarding the modelling using COMSOL Multiphysics®, the simulations of the flow patterns were similar across the flowrates used in the parametric sweep. This applies to both the 2D- and 3D-models, as well as to whether the flat or geometric weaves were modelled. The resulting flow patterns for the weaves were similar across the 2D- and 3D-model, where a major difference was the lack of jets in the 2D-model of the flat weave. This difference is the result of how the flat weave was modelled in both models, where it was treated as a square permeable surface in the 2D-model and as an array of cylinders in the 3D-model. Following this, this section will primarily focus on the results with a flowrate of an average velocity of  $1.5 \text{ m s}^{-1}$ . Additionally, COMSOL Multiphysics® uses the Brinkman equation to simulate flow through a permeable media when using the Free and Porous Media Flow (*fp*) module. This equation assumes laminar flow, which is not a valid condition for flowrates used here. As such, the assumption done in this modelling work is that the difference caused by treating the flow in the domains for the weaves as a laminar flow is negligible. This assumption is reasonable considering the thickness of the weaves.

**Figure 4.35:** The flow pattern of the 2D-model with the flat weave, with a flowrate of an average velocity of  $1.5 \text{ m s}^{-1}$ . Here a section of the whole system is shown, where this section encompasses the filter house, as well as a part of the inlet and outlet tube. In this image the colours correspond to the magnitudes of the velocities that the simulation converged on, and the legend on the right shows which velocity corresponds to which colour. The flow here goes from left to right. Further, it can be seen that the flowrate increases near the walls prior to the flat weave, and as such there is no expansion of the flow pattern inside of the filter house. There is only a contraction as the flow passes the protrusions in the filter house. After the flow passes the protrusions in the filter house, it expands into the outlet tube as the space between the protrusions is narrower than the diameter of the tubes.



### 4.3.1 2D-Modelling

The first simulation done with COMSOL Multiphysics<sup>®</sup> was the simulation of the flat weaves in the 2D-model. The resulting flow pattern for the average flowrate of  $1.5 \text{ m s}^{-1}$  can be seen in Figure 4.35, which shows a section of the model with the colours corresponding to the magnitude of the velocity. One notable feature of this figure is the expansion of the flow pattern prior to permeating through the flat weave. This expansion could have been caused due to the weaves resistance to being permeated, leading to a spread of the flow on the surface of the weave. As the tubes diameter is similar to the diameter of the filter house, there is little space for the flow to expand into after permeating the weave. Due to the filter house having protrusions next to the outlet tube, and the distance between these protrusions being less than the tube diameter in the middle section of the filter house, the flow pattern will contract prior to this protrusion and expand in the outlet tube. The higher flowrates in the outlet tube can be attributed to this contraction.

Figure 4.36 shows the simulation with the geometric weave at  $1.5 \text{ m s}^{-1}$ . In this figure we can see expansion inside the filter house and four areas of high flowrate. This expansion could be caused by the same mechanism as with the flat weave, where the flow pattern spreads upstream of the weave due to the weave's resistance to being permeated. This notion is supported by the two of the high flowrate areas, the ones upstream of the weave. These areas are on the weave, and next to the both walls of the filter house. As such, the surface of the weave in this area has a smaller volume compared to rest of the geometric weave, and this yields the high flowrates. Comparatively the two high flowrate areas downstream of the weave begin next to the bend in the weave that is closest to the walls of the filter house, and therefore next to the first high flowrate areas. Additionally, the initial part of the high flowrate areas downstream of the weave, are adjacent to two faces of the geometric weave. This adjacency implies that the flow that permeates these faces ends up in this region, as the streamlines in the figure shows the flow permeates the weave in it's normal direction. As it is water that is simulated in this model, and

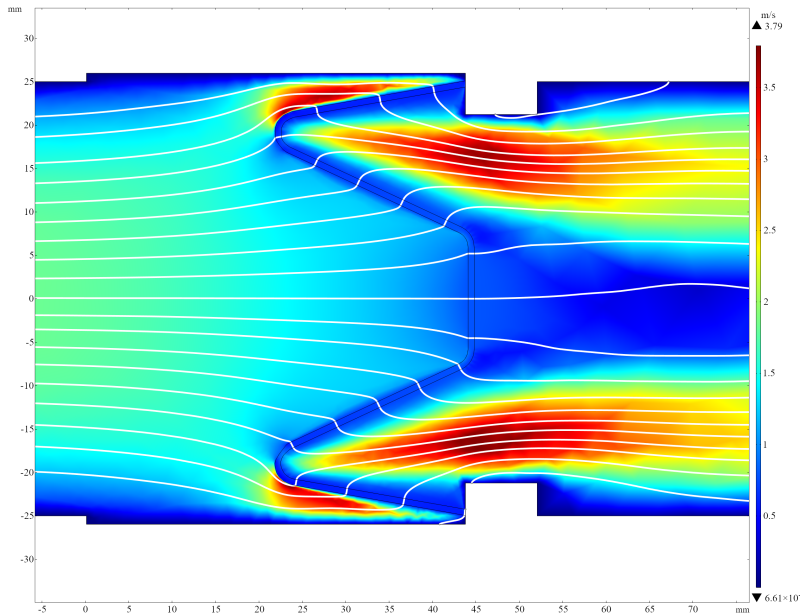




**Figure 4.36:** The flow pattern of the 2D-model with the geometric weave, with a flowrate of an average velocity of  $1.5 \text{ m s}^{-1}$ . Here a section of the whole system is shown, where this section encompasses the filter house, as well as a part of the inlet and outlet tube. In this image the colours correspond to the magnitudes of the velocities that the simulation converged on, and the legend on the right shows which velocity corresponds to which colour. The flow here goes from left to right. It can be seen that the flow pattern expands inside the filter house. Also, four areas with a high flowrate is visible, where two of these areas are upstream of the weave, next to the walls of the filter house. And the other two high flowrate areas are downstream from the geometric weave, each beginning next to the bends in the weave nearest the walls of the filter house and ending inside the outlet tube.

water is incompressible, this results in a higher flowrate. Therefore, both pairs of either ends of the weave can be considered as extensions of each other.

Both Figure 4.35 and 4.36, show the 2D-model simulated at the same flowrate of an average velocity of  $1.5 \text{ m s}^{-1}$ . And both of these simulation has areas that exceed the average velocity. In both instances these areas can be considered as caused by constrictions, where it is only the protrusions of the filter house for the flat weave, and primarily the geometry of the weave for the geometric weave. For both of these simulation the maximal flowrate can be seen in the legend, where it is  $2.06 \text{ m s}^{-1}$  for the flat weave, and  $3.79 \text{ m s}^{-1}$  for the geometric weave. The higher flowrates in the simulation with the geometric weave can be attributed to the area in which the flow is constricted. Whereas the simulation constricts the whole flow pattern in-between the protrusions in the filter house. The geometric weave constricts the flow pattern, that is distributed across it's surface, according to it's geometry. Thus it constricts the flow in a subset of the area constricted by the protrusions in the filter house.

Following this, the Particle Tracing for Fluid Flow (*ftp*) module was used to simulate particles moving in the flow pattern of the 2D-model with the geometric weave. And a particle tracing and particle movement plots of the solution are shown in Figure 4.37 and 4.38 respectively. In the particle tracing figure, the flow through the geometric weave in it's normal direction is not as noticeable as in Figure 4.36, although it is still noticeable. What is evident in this figure is that the flow in high flowrate areas upstream from the weave have a direction that is nearly tangential to the face of the geometric weave next to it. And that the flow that passes through this area primarily permeates the geometric weave in the parts of this face that is further downstream. Thus this corroborates the notion of this higher flowrate being caused by a constraint in the volume. In the figure for the particle movement, and shows chronological aspect to the flow pattern. Here it is evident that the bends in the middle of the filter, and furthest downstream, are being permeated by the flow prior to the bends near the walls of the filter house. This figure shows the

In  and  are complementary animated GIFs, that are embedded in this document, for Figure 4.37 and 4.38 respectively.

**Figure 4.37:** In this figure the trajectories of the simulated particles at 0.5 s using COMSOL Multiphysics® is shown. It can be seen that the flow mainly permeates through the geometric weave along its normal, resulting in the two sloped faces of the weave delivering the flow to the same area. Additionally it can be seen that the high flowrate area above the bends upstream in the weave has its trajectory along the bend. Thus providing the geometry with a void out of the weaves face that the high flowrate area touches, indicating a lower tendency of the flow to permeate this section of the weave.

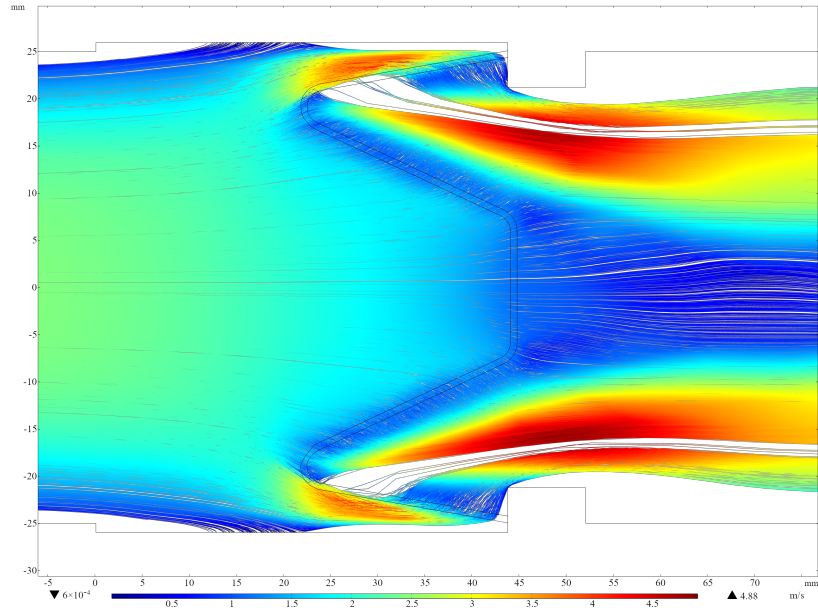
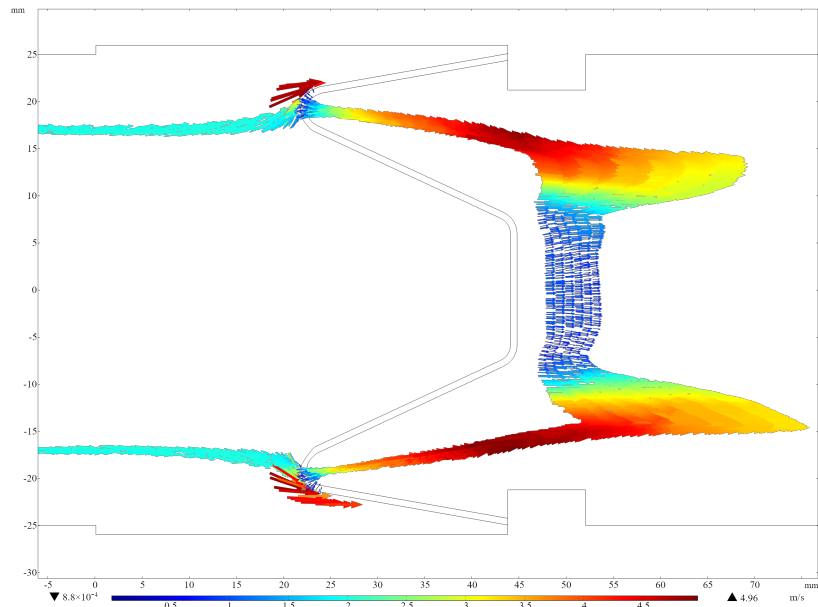


**Figure 4.38:** This figure shows the particle movement simulated at 0.1525 s with COMSOL Multiphysics®. In this image the particles in the center of the system has permeated through the geometric weave, and are situated in a pattern that matches the flow pattern seen in Figure 4.36. And the particles that were to the sides of the system has yet to permeate through the weave, where they are moving along the bend of the weave that is furthest upstream. As such the bends in the geometric weave that are the furthest downstream are permeated first, followed by the ones upstream. It can also be seen that the particles to the sides of the system flow and meet the upstream bend, and this gives the flow at this position a higher flowrate along the bend.



distribution of the flow along the weave, where the particles to the sides of the system flows in such a pattern as to meet the bend and pass into the high flowrate area. This corroborate the earlier notion of a volume constraint leading to higher flowrates, as a higher amount of the flow passes through this area. Otherwise the flow pattern of both these figures match, and this is show in the two attached animations to this report, saved as gif files.

### 4.3.2 3D-Modelling

As both the 2D- and 3D-model describe the same system, we can expect similar results in the simulations. And, the main differences between the results can be attributed to minor differences in the geometry, particularly the in the models of the geometric weave and the different approach for the flat weave, and the inherent difference between a 2D- and 3D-model.

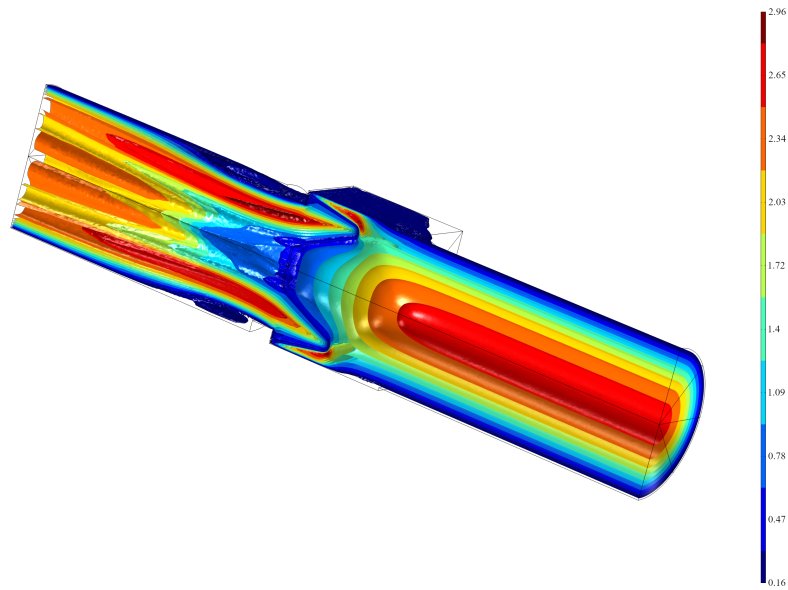


**Figure 4.39:** A figure showing an isosurface plot of the converged solution of the system with the geometric weave using COMSOL Multiphysics®. The solution used here is with a flowrate of an average velocity of  $1.5 \text{ m s}^{-1}$ , and showing the system through the middle axis of the filter house. There are 10 levels of the isosurface, each having a colour that corresponds to their flowrate. Here we can see four high flowrate areas, two upstream and two downstream of the geometric weave. And two comparatively higher flowrate areas in the later section of the outlet tube. The area just downstream of the center of the geometric weave is of a comparatively lower flowrate.

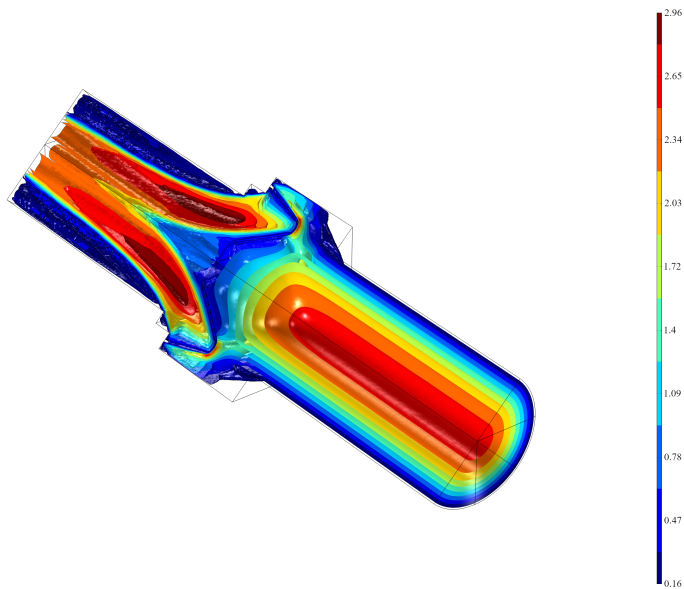


**Figure 4.40:** A figure showing an isosurface plot of the converged solution of the system with the geometric weave using COMSOL Multiphysics®. The solution used here is with a flowrate of an average velocity of  $1.5 \text{ m s}^{-1}$ , and showing the system through the middle axis of the filter house. There are 10 levels of the isosurface, each having a colour that corresponds to their flowrate. Here we can see four high flowrate areas, two upstream and two downstream of the geometric weave. The two high flowrate areas downstream of the geometric weave appear to join together in the later section of the outlet tube. The area just downstream of the center of the geometric weave is of a comparatively lower flowrate.

In Figure 4.39 and 4.40 two sides of the converged flow pattern for the 3D-model with the geometric weave is shown. Both figures show an isosurface representation of the velocity magnitude, with 10 levels and corresponding colours to this magnitude and at a flowrate of an average velocity of  $1.5 \text{ m s}^{-1}$ . Figure 4.39 shows this isosurface in an axial cross-section through the middle of the filter house, whilst Figure 4.40 shows this cross-section through the diagonal of the filter house. In both figures the flow goes from the bottom right to the top left. We can see the same four high flowrate areas in both these figures, which indicates that the respective areas either upstream or downstream of the geometric weave are part of the same high flowrate volume. Additionally, the size of these areas appear to vary between the middle and diagonal of the filter house, where the area upstream from the geometric weave decrease in size and conversely the areas downstream of the weave increase in size.

This could be caused by the distribution of the flow favouring the interior of the geometric weave on the diagonal, as the length of the interior of the weave takes up a larger fraction of the whole compared to the middle of the filter house. As such more of the flow would pass through the interior of the geometric weave in this axis, and thus the flow favours the interior face next to the bend in the upstream portion of the weave to the exterior face. This would facilitate a higher flowrate nearer to the center of the system, and as such this flow would also have a higher potential of spreading to the center.

This potential of spreading to the center of the system would not be present to the flow in the middle axis of the system, as the prioritised flow through the exterior face of the weave, facilitate flows to the edge of the system. In Figure 4.39 we can see the continuation of the high flowrate area downstream of the geometric weave, where it appears that this stream expands as it flows through the system. Next to this stream another stream manifests in the center of the outlet tube. It is proposed that this stream is the extension of the high flowrate area downstream of the geometric weave in the diagonal axis, where this flow spreads to the center of the system, as can be seen in Figure 4.40. And as both of these high flowrate areas can be interpreted to be of the same area, the flow pattern downstream of the geometric weave can be thought of a pattern that is reminiscent of a spherical spiral. The flow pattern in both the middle and diagonal axis of the filter house can also be seen in Figure 4.41, which shows a 2D representation of a subsection of the same simulation that is shown in Figure 4.39 and 4.40.

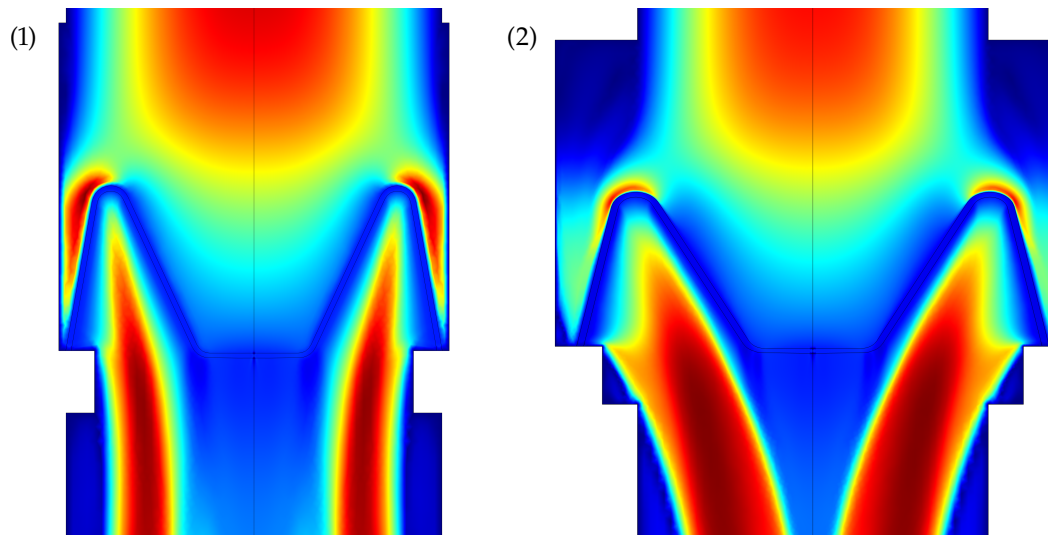


**Figure 4.41:** This figure show two plot of the flow pattern simulated at a flowrate of an average velocity of  $1.5 \text{ m s}^{-1}$  with the geometric weave using COMSOL Multiphysics<sup>®</sup>. Both are 2D-plots of the system shown in Figure 4.39 and 4.40, where (1) shows the flow pattern along the middle axis of the filter house whilst (2) shows the diagonal axis. In both images the colour correspond whit the magnitude of the flowrate, and they are scaled to the aspect ratio and the flow goes from the top of the images to the bottom. We can see the four high flowrate areas in both (1) and (2), two of which are upstream of the geometric weave and two downstream of the weave. The high flowrate areas upstream of the geometric weave appears to be larger in the middle plane than the diagonal plane. Additionally the high flowrate area downstream of the geometric weave appear to stay along the edge of the outlet tube for the middle plane, whilst it spreads towards the center of the outlet tube for the diagonal plane.

Replicating the experimentally gathered pressure-drop data in COMSOL Multiphysics<sup>®</sup> has not been attempted, however the pattern in the pressurechanges on the weaves can be assumed to be consistent with a

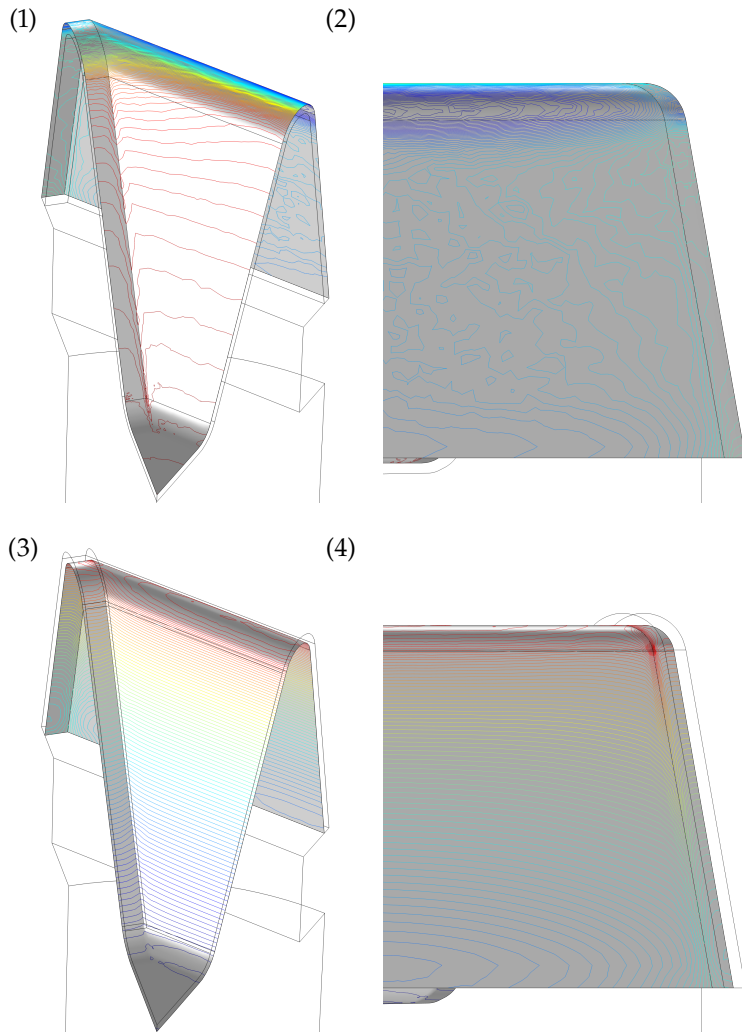


**Figure 4.42:** The pressure contour of one eighth of the whole geometric weave: where (1), the top of the front side; (2), the top of the back side; (3), the bottom of the front side, and (4), the bottom of the back side. In this figure it can be seen that the top side has the most pressure changes on top of the upstream bend, and the pressure is highest nearest the center of the geometric weave. Similarly the bottom side has also the highest pressure changes on the upstream bend, where this location is also the site of the highest pressure. Of both these sides, the lowest pressure values of the topside is greater than the highest pressure value of the bottom side. A difference between the topside and bottom side is that the pressure levels on the topside is more erratic, whilst the levels on the bottom side is more even. And the pressure levels on the front side of the top sides show that each pressure level moves downstream from the middle to the diagonal, where it moves up on the diagonal.

varying flowrate and permeability. In this manner the pressure contour on both sides of the geometric weave, can be considered. Figure 4.42, shows four images of two plots of the pressure contour, at the flowrate of an average velocity of  $1.5 \text{ m s}^{-1}$ . Two plots, one for the topside and bottom side, is used due to the resulting pressure difference across the weave in the simulation, where this pressure difference makes one plot of the whole weave impractical, as such two different scales are used for the topside and bottom side respectively. Only one eighth of the geometric weave is shown in this figure, and the colors of the pressure contour correspond with the pressure level, where blue is the lowest pressure and red the highest. It can be seen that the highest pressure gradient is on the weaves upstream bend, and this is the site with the highest pressure on the bottom side. Conversely, the place with the highest pressure on the topside is the center of the weave. The faces on the topside of the weave show pressure contours that bend down into the edge of the model. These bends are more apparent further upstream on the face, and these bends become steeper for the face on the diagonal axis of the filter house. On this diagonal axis, the contours reach furthest upstream the further downstream on the face the contours are, compared with the middle axis. The converse is true near the bends upstream on these interior faces.

When comparing these pressure contours with the flow pattern in Figure

4.39 and 4.40, where the inlet flowrates are coaxial, the only difference in the pressure contours on the interior of the geometric weave is the location where the flow meets the geometry. It can therefore be considered that the shapes of the pressure contours on the topside of the geometric weave are caused by the difference in this geometry compared with a circle. In the edges, which are caused by a simplification in the modelling of the geometric weave, this discrepancy from a circle is most evident as the two faces meet. And because of this simplification, this dip in the pressure contour can be considered to be softer in reality. Similarly, as the diagonal face also is the result of a simplification in the model, the upstream bends in the pressure contours can be considered to be exaggerated in this simulation and therefore to be softer in reality.

On the bottom side of the geometric weave, the pressure contours are more even than on the topside. The unevenness on the topside, coupled with the evenness on the bottom side stride with the earlier notion of the flow passing through the weave in it's normal direction. However the evenness on the bottom side implies that the flow emerges from the weave in it's normal direction. And as such, the flow inside the weave can be assumed flow in a direction close to the weaves normal, and adjust towards the normal direction of the weave as the flow permeates through the weave.

The last simulation is the simulation of the flat weave in the 3D-model. This simulation is done purely through the Turbulent Flow,  $k-\epsilon$  (*spf*), module, and does not model the weave as a permeable media. Here the weave is modelled as two arrays of cylinders, superimposed on each other. This approach assumes that the flow does not wet the weave, and as discussed in section 4.2 this assumption is valid. Due to the different approach in the 2D- and 3D-model of this weave, this simulation shows more details regarding the permeation of the flow through this weave. In Figure 4.43 the flow pattern of the system with the flat weave is shown with a flowrate of an average velocity of  $1.5 \text{ m s}^{-1}$ , where the flowrate is shown as isosurfaces and the colours correspond with the flowrates. The flow in this figure goes from the bottom right to the top left. And a high flowrate area is reciprocated in this simulation, as was the result in the 2D simulation of the flat weave, see Figure 4.35. This high flowrate area can also be viewed in Figure 4.45, which is a 2D-plot of the middle axis for the filter house.

Concerning the flat weave in the simulation, Figure 4.44 shows a close-up view of the isosurface of this weave. Conversely, Figure 4.46 shows a similar close-up view of this weave in a 2D-plot. In both these figures the flowrate in the space between the weaves reaches the highest flowrates in the simulation. These jets reach the the maximal flowrate in the simulation, which is  $2.63 \text{ m s}^{-1}$  as can be seen in the legend from Figure 4.46. In the first both these figures, a region around the weave strands of a comparatively low flowrate can be seen, where this film seems to constrict the high flowrate area in-between the strands. This constraint can also be seen on the flow towards the weave in Figure 4.44, where the isosurface overlays the weave in a net, and inter-mediated by isosurfaces that are reminiscent of half an oblate spheroid, curving inward towards the strands. After the constriction, these jets appear to flow beyond the weave in a pattern that is reminiscent of an prolate spheroid. These jets



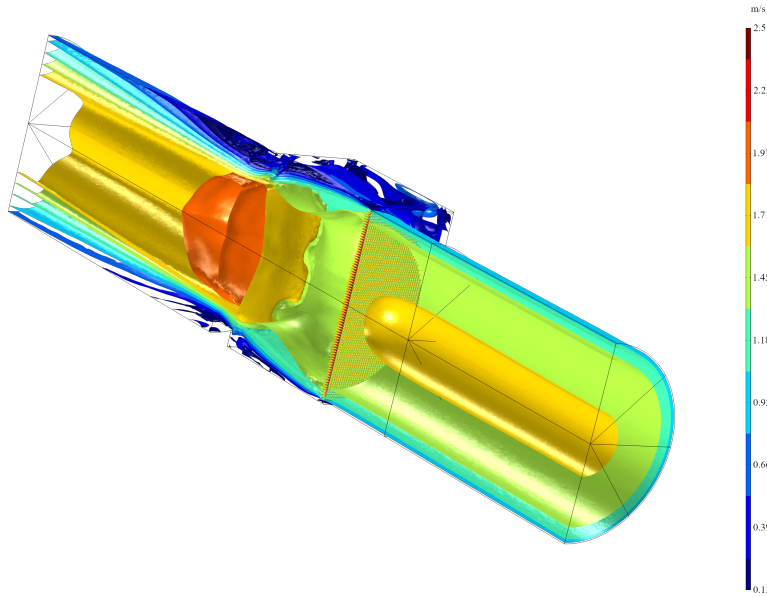


**Figure 4.43:** A 3D-plot of the converged solution for the system with the flat weave using COMSOL Multiphysics® at a flowrate of an average velocity of  $1.5 \text{ m s}^{-1}$ . Here the flow goes from the bottom right to the top left, and the flowrate is represented as isosurfaces using 10 levels, where each level correspond to a colour and the magnitude of the flowrate. In this figure there are two regions with a high flowrate, the first area is primarily inside the outlet tube and the second region is at the flat weave. In the flat weave there are several areas with a high flowrate, each correspond to the space between the strands of the flat weave, and these areas appear as jets, where a close-up of this region is shown in Figure 4.44.

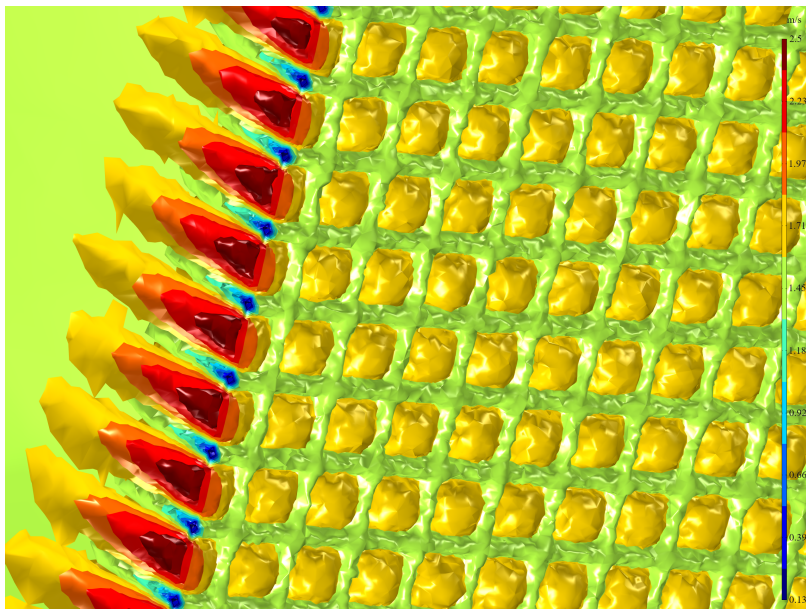


**Figure 4.44:** A close-up of the flat weave as shown in Figure 4.43. In this figure the side of the flat weave that meets the flow is shown, where the flowrate is at an average velocity of  $1.5 \text{ m s}^{-1}$ . The jets with the high flowrates can be seen beginning in the space between the strands of the flat weave, and resembling a prolate spheroid preceded by a constraint of the flowrate by the strands of the weave. The isosurface of this constrain resembles a prolate spheroid in appearance. Following this the strands of the weave appear to have a region of low flowrate around them, where this region trails between the jets downstream of the flat weave.

appear to be separated by regions of a relatively lower flowrate that follow beyond the strands of the weave.

Modelling the geometric weave with individual strands is also possible, where the resulting model would be more complex than the model for the flat weave. Additionally such a model would need to be comprised of bent strands, as the geometric weave is not only comprised of linear strands. However the difference between making a model of the geometric weave with straight or bent strands could be assumed to be negligible. Such a model could be used to compare the flow pattern through the flat and geometric weave, and not relegating the comparisons to the flow pattern around the weaves. From the flow pattern downstream of the weaves, it is clear in the simulation that the geometric weave produces a more complex flow pattern than the flat weave. No simulation with the geometric weave in the reverse position as was used in both the 2D- and 3D-model was done. As such the resulting complex flow pattern

**Figure 4.45:** A 2D-plot of the middle plane for the filter house for the system with the flat weave. This plot shown half of the plane, such that the lower line is the central axis of the system. The flowrate in this plot is the same as for Figure 4.43, with an average velocity of  $1.5 \text{ m s}^{-1}$  and a flow that goes from left to right. The colours of the plot correspond to the magnitude of the flowrate, and has streamlines. We can see the constraint of the flowrate along the protrusions in the filter house and extend into the outlet tube. The jets from the flat weave are visible, and the legend shows that these jets reach a flowrate of  $2.63 \text{ m s}^{-1}$ . a close-up of these jets are shown i Figure 4.46.

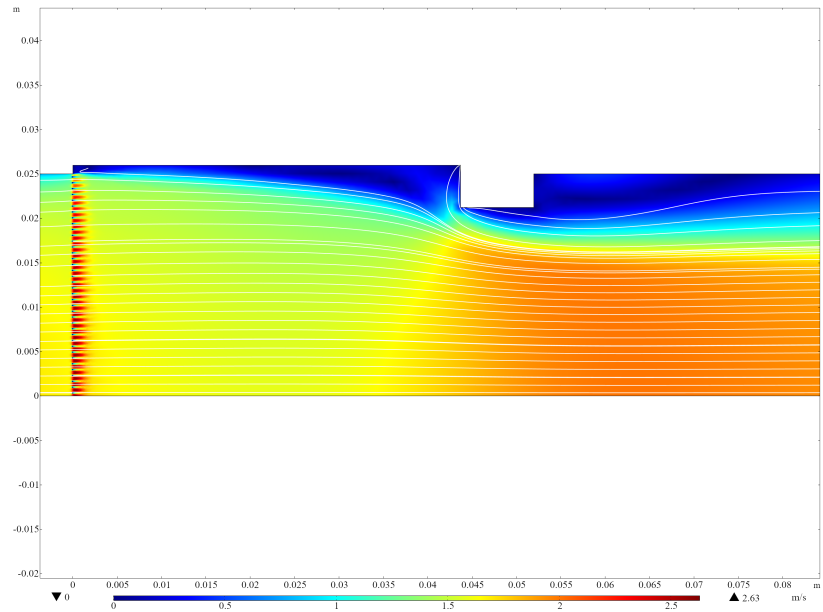
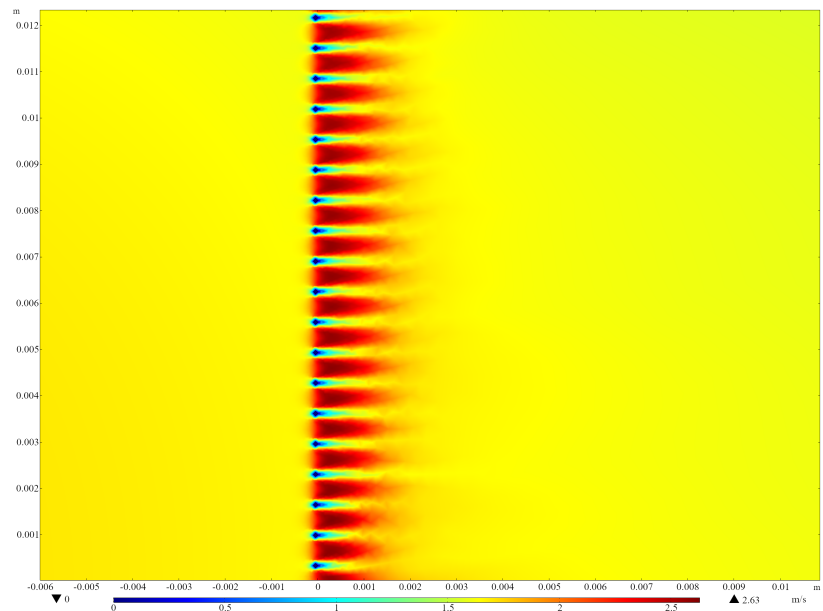


**Figure 4.46:** This figure shows a close-up of the jets in the solution plotted in Figure 4.45. And shows the solution to the simulated 3D-model with the flat weave at a flowrate of an average velocity of  $1.5 \text{ m s}^{-1}$ , where the flow goes from the left to the right. The only visible feature of this figure is the flow regarding the flat weave itself, where the lowest position in the image is the center of the system, and is in the middle plane for the filter house. The jets are visible, and begin in-between the filter strands, and extend past the filter strands, intermeditated by lower flowrate areas. And the strands of the flat weave appears to have a low flowrate region surrounding itself.



from these simulations are not definitive, due to the possibility of the resulting flow pattern of the geometric weave in the reverse position being simpler.

In short the results from this project can be summarised as the following:

- ▶ The geometry of the RGW influenced the pressure-drop, where the flat weaves had a higher pressure-drop than the geometric weaves.
- ▶ Lengthwise the CFF had less pressure-drop than the RGW filters, whilst the total pressure-drop was less for the RGW filters.
- ▶ The pressure-drop of all samples could be analysed experimentally and analytically.
- ▶ The most reliable empirical constants was found using the Brute Force Method.
- ▶ Both the  $k_1$ - and  $k_2$ -values could be identified for all filters.
- ▶ Modelling the RGW with COMSOL Multiphysics® was confirmed a possibility.

From the pressure-drop data the flat weaves were observed to yield a higher pressure-drop compared to the geometric weaves. And both these geometries observed the same following arrangement for the different weaves, from (1) highest pressure-drop to (5) lowest:

1. XW2
2. 43L
3. 36L
4. 40L
5. 34L

Concerning the CFF, the 10 ppi filter was found to have a lower pressure-drop compared to the 20 ppi filter. Both of these filters yielded a higher total pressure-drop compared to the RGW, while also having a lower lengthwise pressure-drop. Adding to this, the circular interior was found to have a smaller pressure-drop relative to the square interior, in spite of it's smaller area, where both interiors had the same diameter and length.

Four methods were used to determine the empirical constants in regards to the Forchheimer equation, and were the Linear Regression Method, Ergun Empirical Method, Exponential Regression Method, and the Brute Force Method. Of these methods the first two gave negative  $k_1$ -values for some of the weaves and in this respect are unreliable. The third method did not regress the exponent for the velocity in the second order term for some of the weaves to 2, and in this respect these values are unreliable. For these three methods the cause for this unreliability was considered to be the same: the high flowrates used in the experiment and the nature of fitting variables to data. Regarding the fourth method, this method yielded empirical constants that were biased towards lower values, which was considered to be more reliable compared to the results from the other three methods.

Modifying the methodology for the water trials to either weigh lower flowrates more, or determine the  $k_1$ -value separate from the  $k_2$  value would eliminate the source of error in the determination of the empirical constants. And by eliminating this source of error, the use of the first

three methods for determining the empirical constants would regain their reliability, thus eliminating the need for the fourth method. Even so, every determined value for  $k_2$  was in the same order of magnitude, as can be seen in Table 4.6. For this reason, the determined  $k_2$ -values were determined to be reliable.

Due to the low number of parallels used for every combination of geometry and weave, the determined empirical constants were determined to not be statistically significant. Further trials are needed to determine these values to determine these constants to statistically significant values.

Beyond this, the possibility of modelling the RGW was confirmed in COMSOL Multiphysics®. And the results from the SEM images confirmed the assumption that the RGW can be modelled as individual strands. One such 3D-model was simulated, and showed jets between the strands, see Figure 4.46. The resulting flow pattern for the flat weave was primarily determined by the system itself, as shown in both the 2D and 3D simulations. And the flow pattern of the geometric weave produces four distinct jets in a plane and a spiral flow pattern, where these jets were determined to be of two distinct volumes of a high flowrate. The simulation of the geometric weave was only done with one orientation of the weave, and no conclusion can be drawn from the flow pattern this weave would produced in the reverse orientation.

A better quantification of the empirical constants in regards to the Forchheimer equation can be accomplished by increasing the number of parallels and eliminating the identified sources of error. And by increasing the number of flowrates used in the experiment, while controlling the intervals between each flowrate. In such a way statistically significant values for the empirical constants can be determined. These values can be compared with other additional approaches. For quantifying these values the following statistical methods can be used:

- ▶ Investigating the contribution of the identified sources of error on the empirical constants.
- ▶ Perform similar experiments using liquid aluminium.
- ▶ Corroborate the empirical constants with simulations of the system.

In addition, the empirical values for the geometric weave can be investigated in the reverse direction from the direction used in this project. And the flow pattern of the geometric weave can be simulated as individual strands.

Further, the filtration efficiency for RGW filters can be investigated and compared with CFF. A time-dependent investigation of the fatigue, performance and wetting properties of the RGW filters in liquid aluminium. Following, the reusability and recyclability of the RGW can be investigated.

Additionally, the RGW can be treated as being made of particles. Where an attempt at corroborating the size of these particles with measurable aspects of the weave, e.g. the thickness of the weaves strands or the space in the weave.



# Bibliography

Here are the references in citation order.

- [1] D. Corleen Chesonis. *A Holistic Approach to Molten Metal Cleanliness*. Ed. by Arne P. Ratvik. Springer International Publishing, 2017, pp. 1411–1417 (cited on page 1).
- [2] CRU International International Aluminium Institute. ‘Opportunities for aluminium in a post–Covid economy’. en. In: (2022), p. 41 (cited on page 1).
- [3] Pyrotek. *Rigid Glasweve® Filters for Sand and Permanent Mould Casting*. 2022. URL: <https://www.pyrotek.com/primary-solutions/aluminium/foundry/show/ProductLine/rigid-glasweve-filters-for-gravity-casting> (visited on 05/15/2022) (cited on page 1).
- [4] Mark W. Kennedy. ‘Removal of Inclusions from Liquid Aluminium using Electromagnetically Modified Filtration’. In: (2013). (Visited on 05/19/2022) (cited on page 3).
- [5] Philipp Forcheimer. *Wasserbewegung Durch Boden*. Vol. 45. 1901, pp. 1782–1788 (cited on page 3).
- [6] Sabri Ergun. *Fluid Flow through Packed Columns*. Vol. 48. 1952, pp. 89–94 (cited on page 3).
- [7] ThermoFisher Scientific. ‘Principles of Scanning Electron Microscopy’. en. In: (2022) (cited on page 4).
- [8] ‘Principles of SEM’. In: *Principles and Practice of Variable Pressure/Environmental Scanning Electron Microscopy (VP-ESEM)*. John Wiley & Sons, Ltd, 2008. Chap. 2, pp. 17–62. doi: <https://doi.org/10.1002/9780470758731.ch2> (cited on page 4).
- [9] Susan Swapp. ‘Scanning Electron Microscopy (SEM)’. en. In: (2017) (cited on page 4).
- [10] COMSOL. ‘The Finite Element Method (FEM)’. en. In: (2017) (cited on page 5).
- [11] COMSOL. ‘CFD module’. en. In: (2017) (cited on page 5).
- [12] COMSOL. ‘Navier-Stokes Equations’. en. In: (2017) (cited on page 6).
- [13] COMSOL Walter Frei. ‘Which Turbulence Model Should I Choose for My CFD Application?’ en. In: (2017) (cited on page 6).
- [14] Kexu Zhang. ‘Liquid Permeability of Ceramic Foam Filters’. In: 98 (2012). (Visited on 03/07/2022) (cited on pages 10, 11, 29).
- [15] Claudia Voigt et al. ‘Overview of the Possibilities and Limitations of the Characterization of Ceramic Foam Filters for Metal Melt Filtration’. eng. In: (2021) (cited on page 11).
- [16] Joseph G. Eisenhauer. ‘Regression through the Origin’. In: *Teach. Stat.* 25.3 (2003), pp. 76–80. doi: [10.1111/1467-9639.00136](https://doi.org/10.1111/1467-9639.00136). (Visited on 05/16/2022) (cited on page 14).





# APPENDIX



# Filter House Dimensions

# A

In Table A.1 the measurements for the filter house are presented.

Tube diameter: [mm]	Filter house measurements [mm]		
	diameter:	holder height:	holder width:
50.00	51.94	8.26	4.75

**Table A.1:** The measured dimensions of both the filter house and tube diameter for the pressure drop experiments.



## B SEM Samples

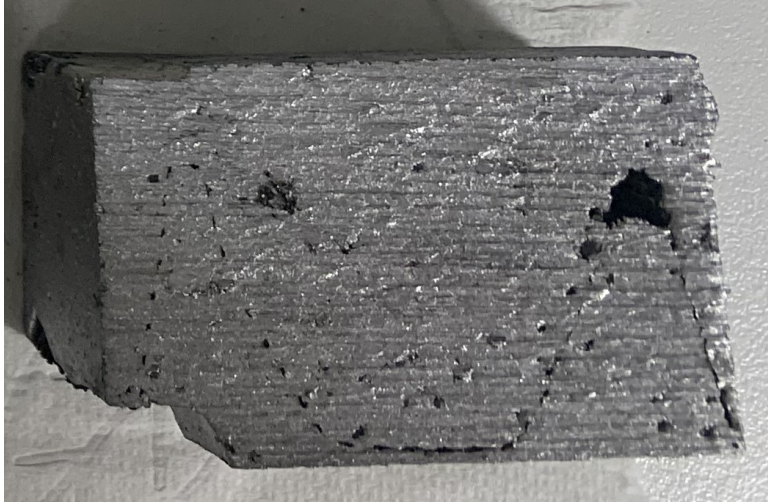


**Figure B.1:** Cut casting sample of PO48 - 25052 (20x36L) before metallographic preparation for SEM



**Figure B.2:** Cut casting sample of PO48 - 25653 (20x40L) before metallographic preparation for SEM

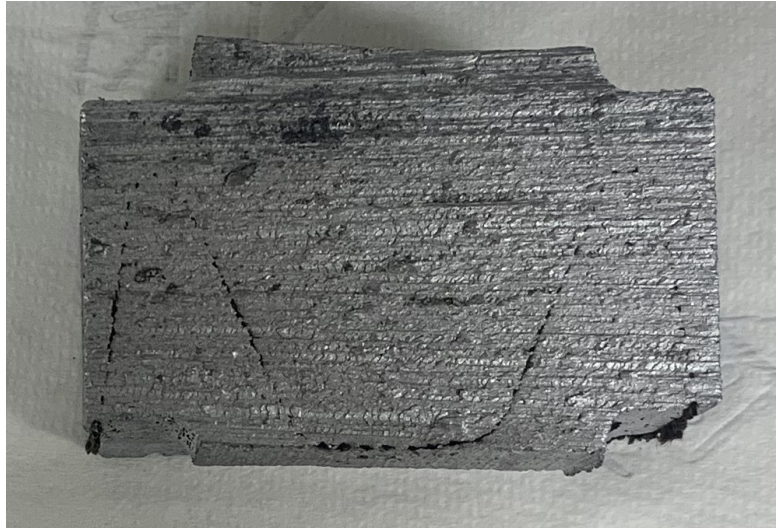


**Figure B.3:** Cut casting sample of PO48 - 25054 (20x43L) before metallographic preparation for SEM



**Figure B.4:** Cut casting sample of PO48 - 2505X (20xXW2) before metallographic preparation for SEM

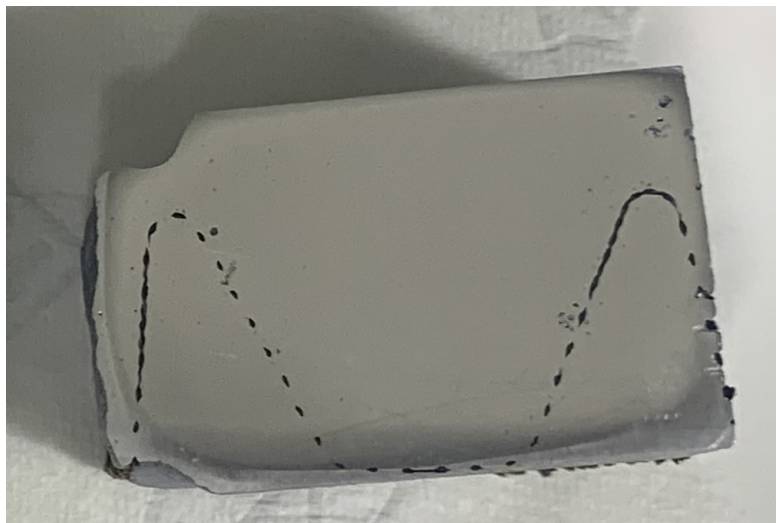


**Figure B.5:** Cut casting sample of PO48 - 25052 (20x36L) after metallographic preparation for SEM

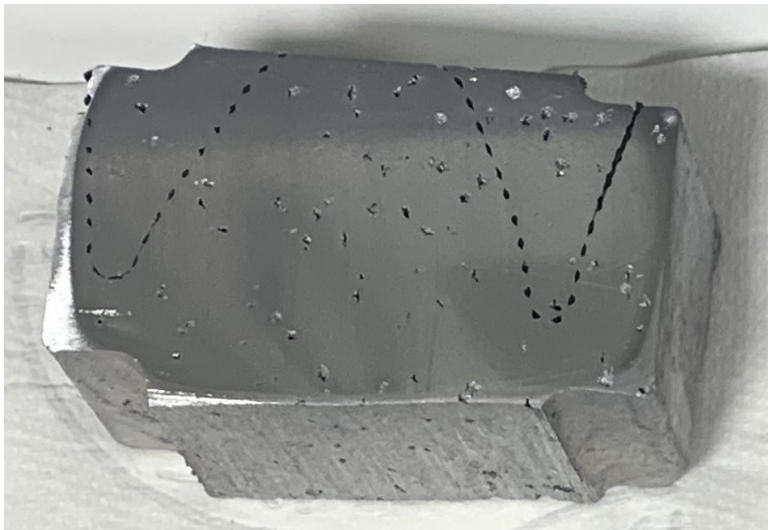


**Figure B.6:** Cut casting sample of PO48 - 25653 (20x40L) after metallographic preparation for SEM

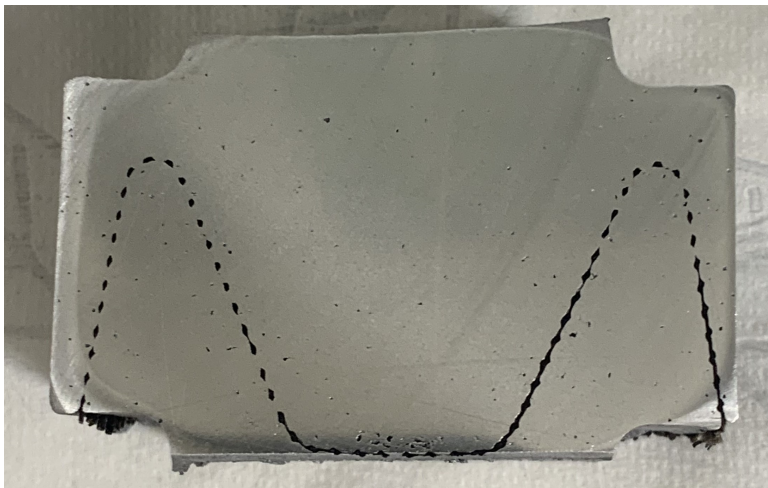


**Figure B.7:** Cut casting sample of PO48 - 25054 (20x43L) after metallographic preparation for SEM

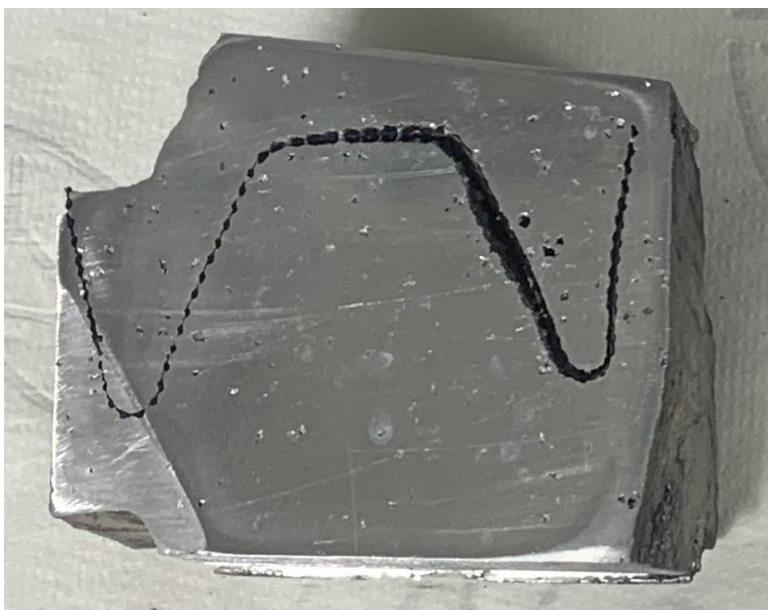
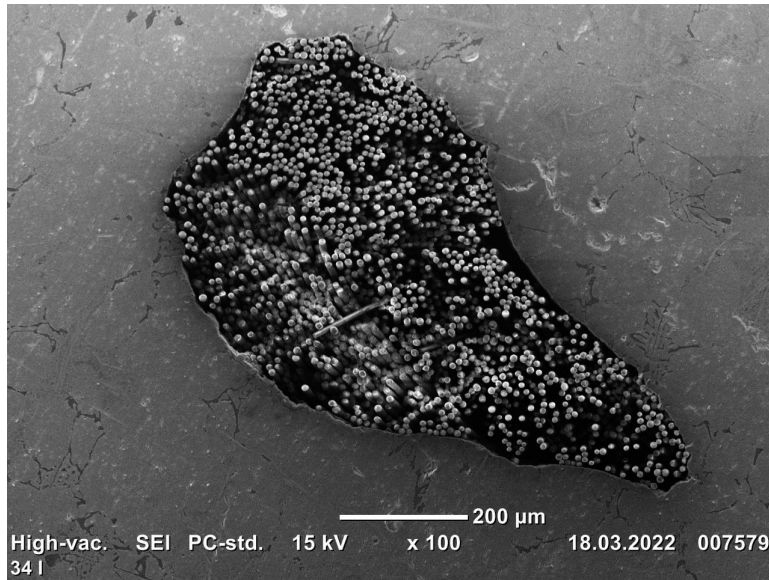


**Figure B.8:** Cut casting sample of PO48 - 2505X (20xXW2) after metallographic preparation for SEM

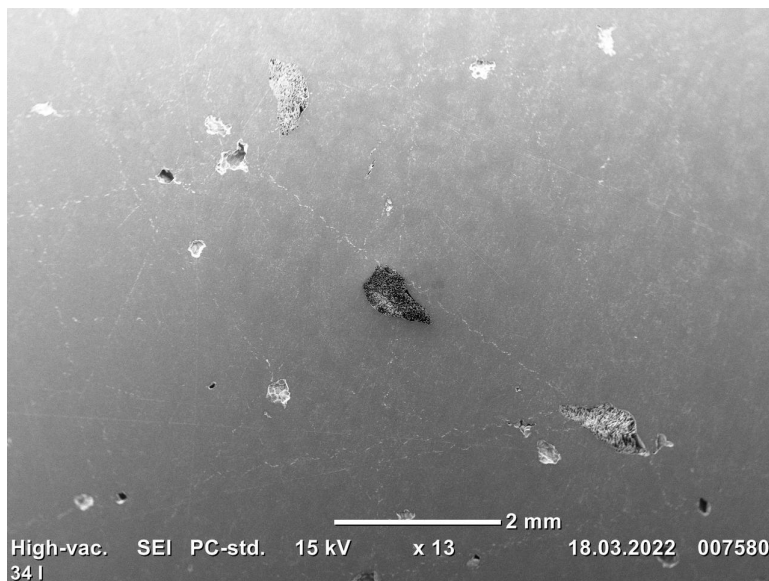




## C SEM Pictures

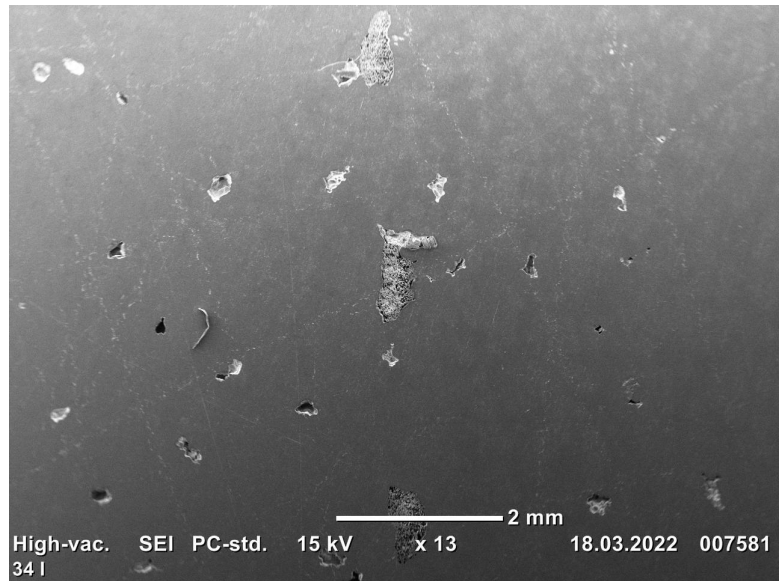


**Figure C.1:** Close-up of a weave in the sample of geometrical shaped filter PO48 - 2505I (20x34L). Zoom = x100. SEI. High-Vacuum.

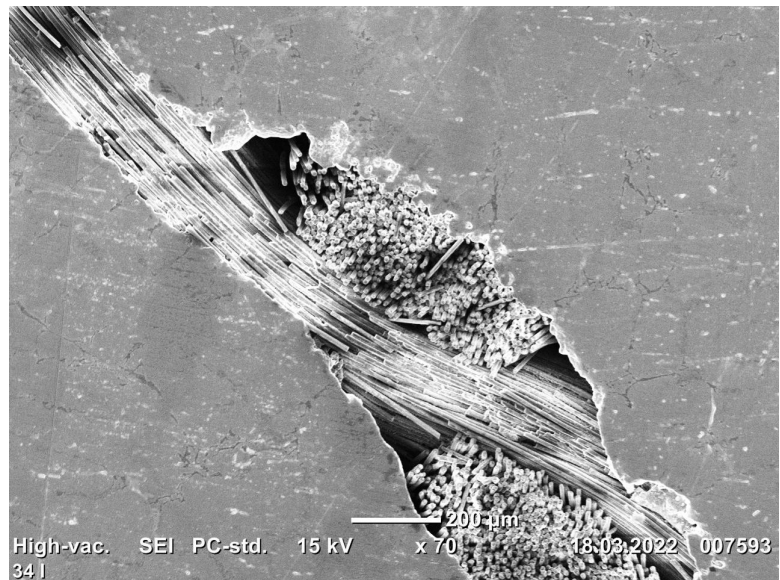


**Figure C.2:** Weaves and casting shrinkages in the sample of geometrical shaped filter PO48 - 2505I (20x34L). Zoom = x13. SEI. High-Vacuum.

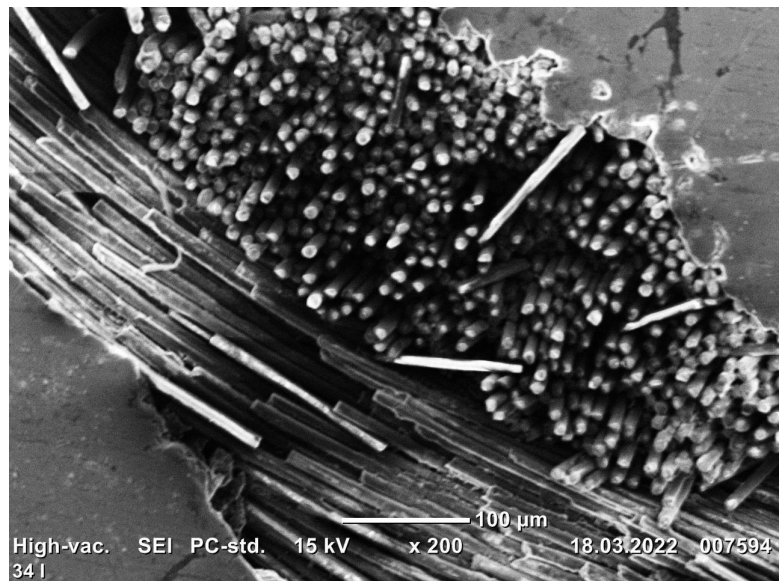
**Figure C.3:** Weaves and casting shrinkages in the sample of Geometrical shaped filter PO48 - 25051 (20x34L). Zoom = x13. SEI. High-Vacuum.

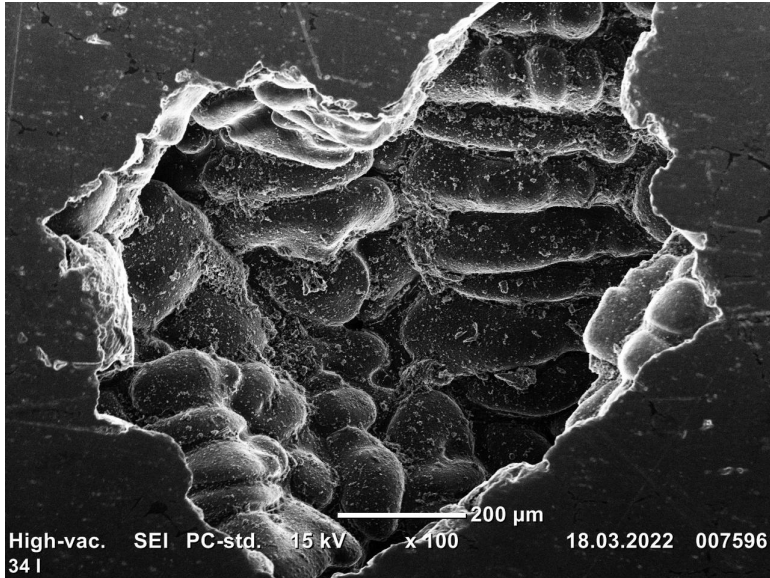


**Figure C.4:** Close-up of a weave in the sample of geometrical shaped filter PO48 - 25052 (20x36L). Zoom = x70. SEI. Parallel 1. High-Vacuum.

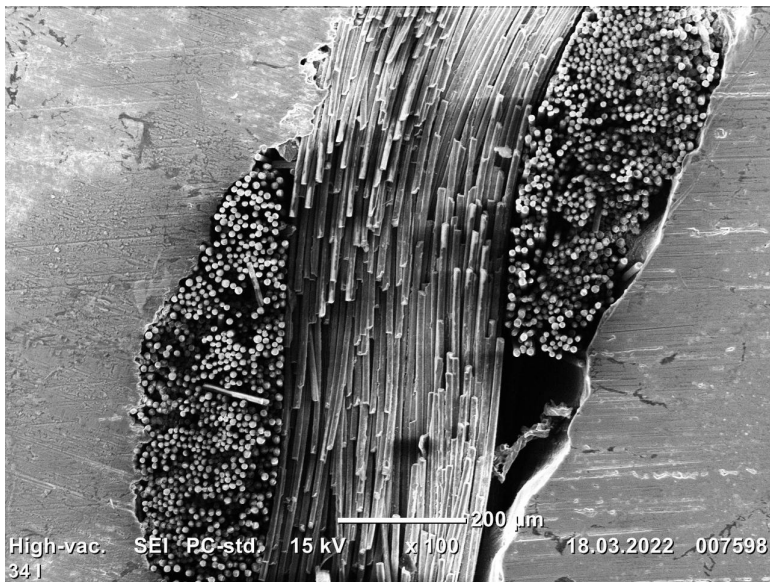


**Figure C.5:** Close-up of a weave in the sample of geometrical shaped filter PO48 - 25052 (20x36L). Zoom = x200. SEI. Parallel 1. High-Vacuum.

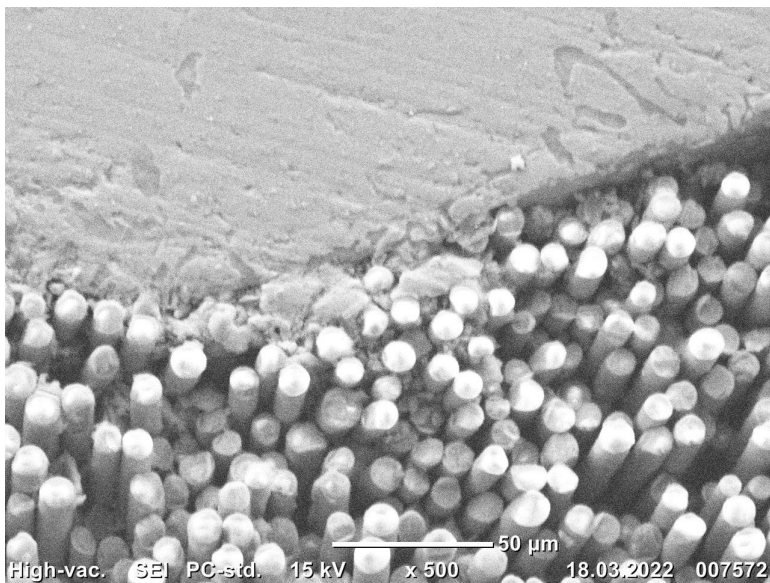




**Figure C.6:** Close-up of a cavity caused by casting shrinkage in the sample of geometrical shaped filter PO48 - 25052 (20x36L). Zoom = x100. SEI. Parallel 1. High-Vacuum.

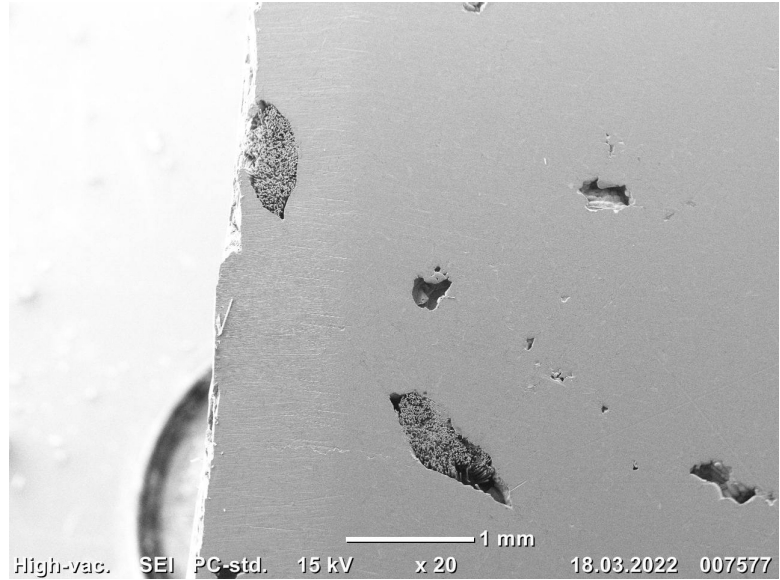


**Figure C.7:** Close-up of a weave in the sample of geometrical shaped filter PO48 - 25052 (20x36L). Zoom = x100. SEI. Parallel 1. High-Vacuum.

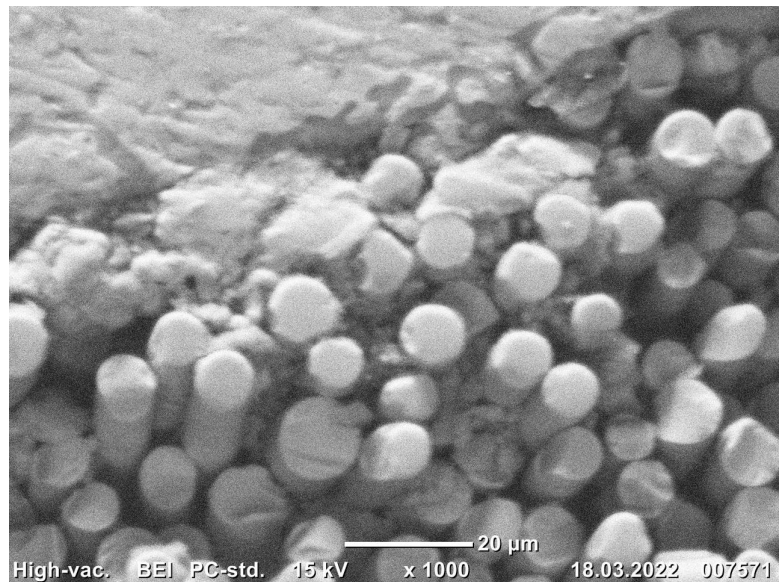


**Figure C.8:** Close-up of a weave in the sample of geometrical shaped filter PO48 - 25052 (20x36L). Zoom = x500. SEI. Parallel 2. High-Vacuum.

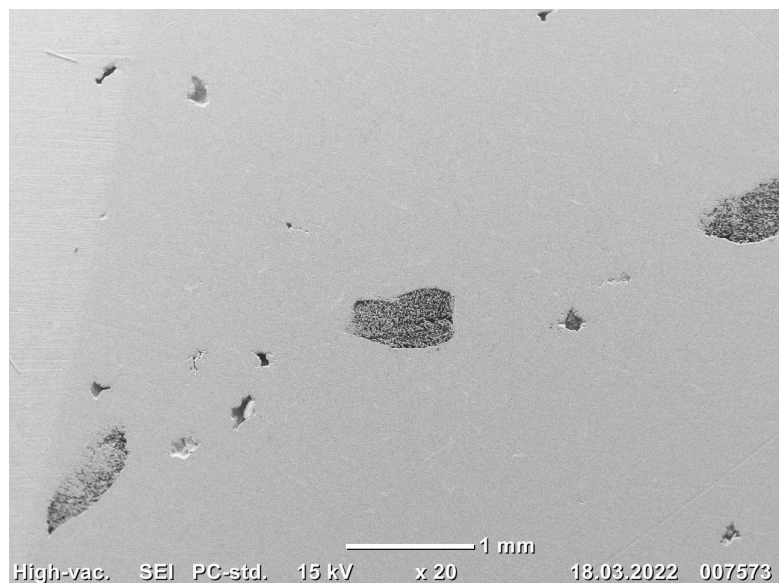
**Figure C.9:** Weaves and cavities caused by casting shrinkages in the sample of geometrical shaped filter PO48 - 25052 (20x36L). Zoom = x20. SEI. Parallel 2. High-Vacuum.

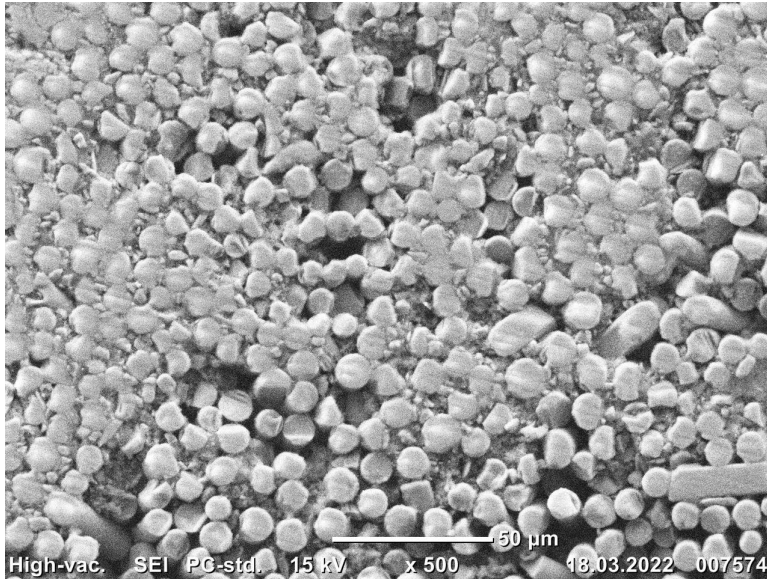


**Figure C.10:** Close-up of a weave and a degree of wetting in the sample of geometrical shaped filter PO48 - 25052 (20x36L). Zoom = x1000. BEI. Parallel 2. High-Vacuum.

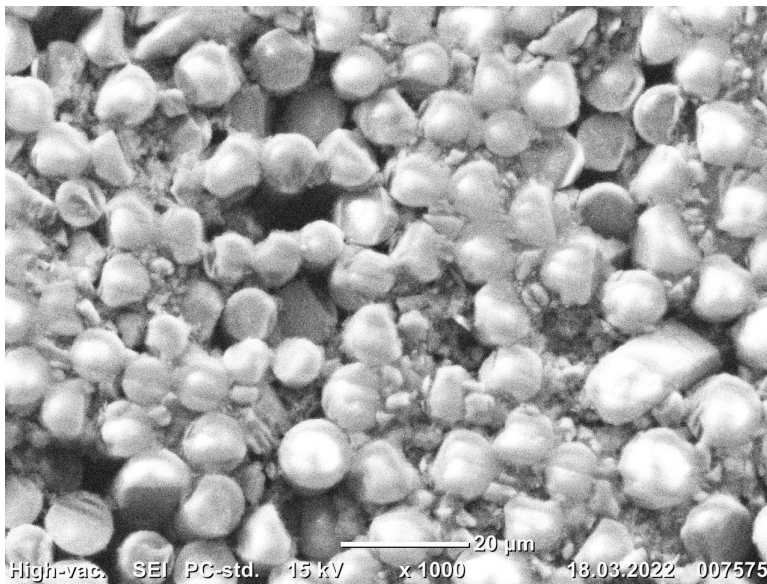


**Figure C.11:** Weaves and cavities caused by casting shrinkages in the sample of geometrical shaped filter PO48 - 25052 (20x36L). Zoom = x20. SEI. Parallel 2. High-Vacuum.

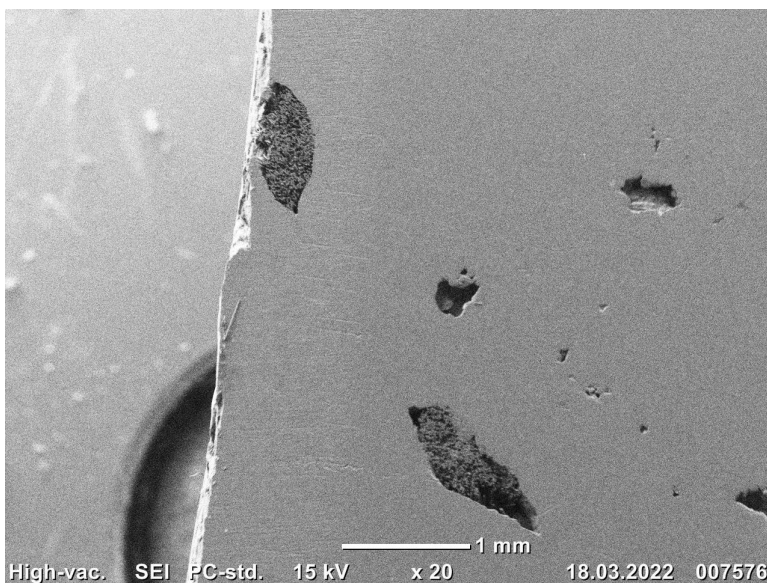




**Figure C.12:** Close-up of a weave in the sample of geometrical shaped filter PO48 - 25052 (20x36L). Zoom = x500. SEI. Parallel 2. High-Vacuum.

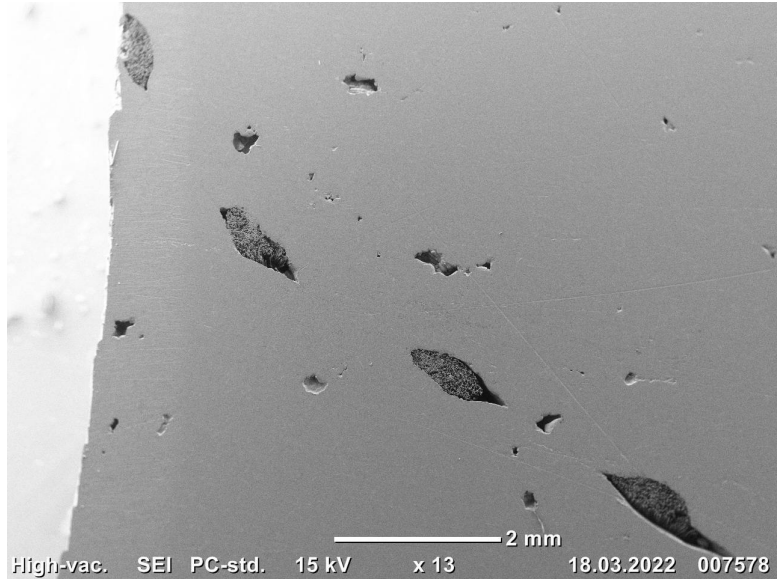


**Figure C.13:** Close-up of a weave in the sample of geometrical shaped filter PO48 - 25052 (20x36L). Zoom = x1000. SEI. Parallel 2. High-Vacuum.

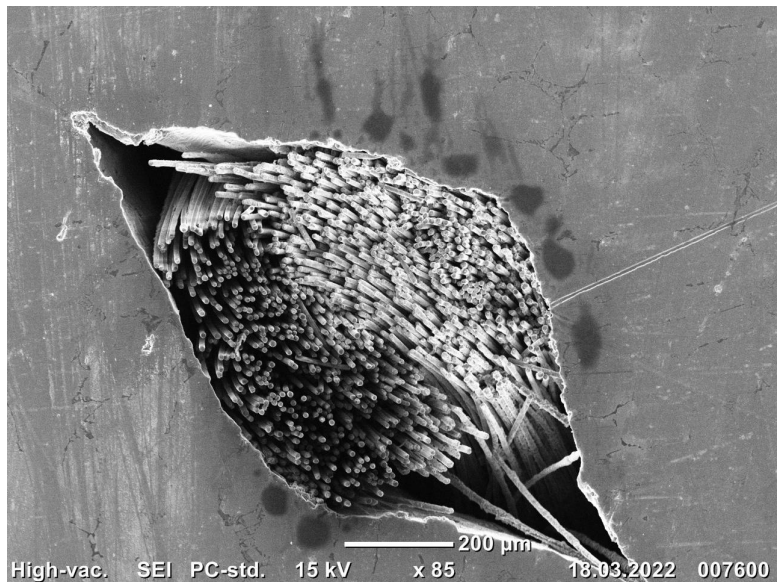


**Figure C.14:** Weaves and cavities caused by casting shrinkages in the sample of geometrical shaped filter PO48 - 25052 (20x36L). Zoom = x20. SEI. Parallel 2. High-Vacuum.

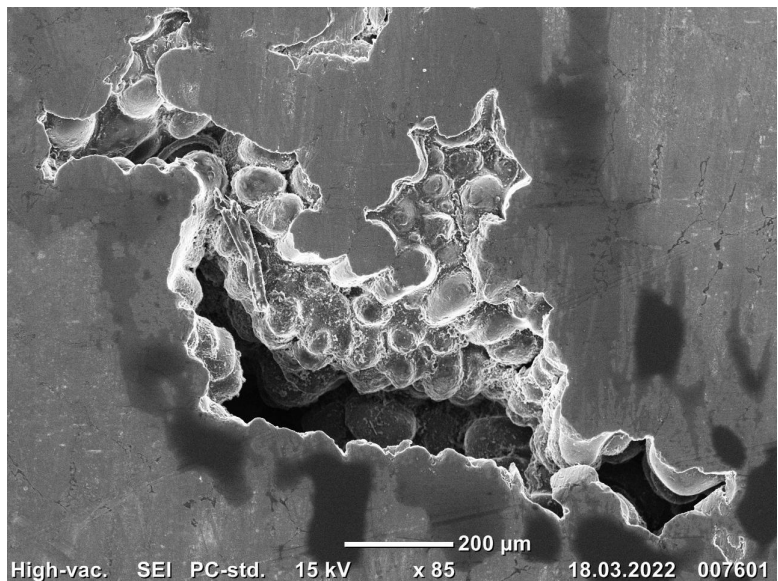
**Figure C.15:** Weaves and cavities caused by casting shrinkages in the sample of geometrical shaped filter PO48 - 25052 (20x36L). Zoom = x13. SEI. Parallel 2. High-Vacuum.

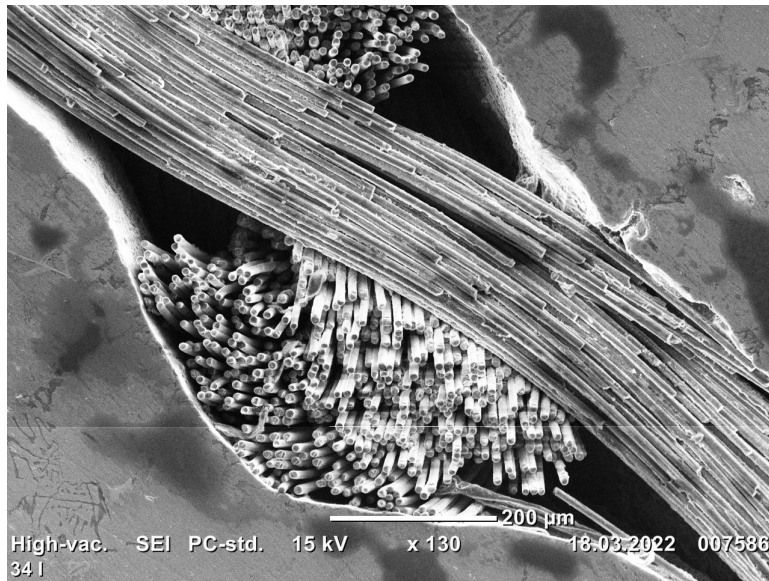


**Figure C.16:** Close-up of a weave and possible permeation of ethanol in the sample of geometrical shaped filter PO48 - 25653 (20x40L). Zoom = x85. SEI. High-Vacuum.

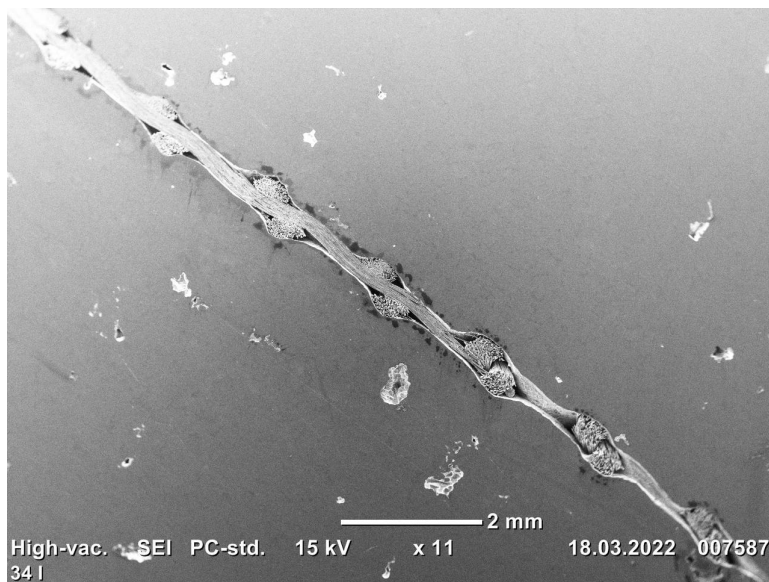


**Figure C.17:** Close-up of a cavity caused by casting shrinkage in the sample of Geometrical shaped filter PO48 - 25653 (20x40L). Zoom = x85. SEI. High-Vacuum.

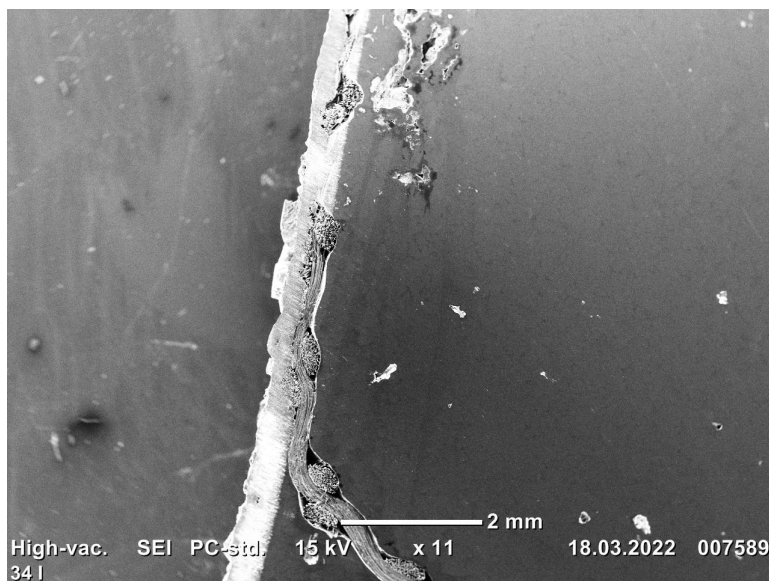




**Figure C.18:** Close-up of a weave and possible permeation of ethanol in the sample of geometrical shaped filter PO48 - 25054 (20x43L). Zoom = x130. SEI. High-Vacuum.

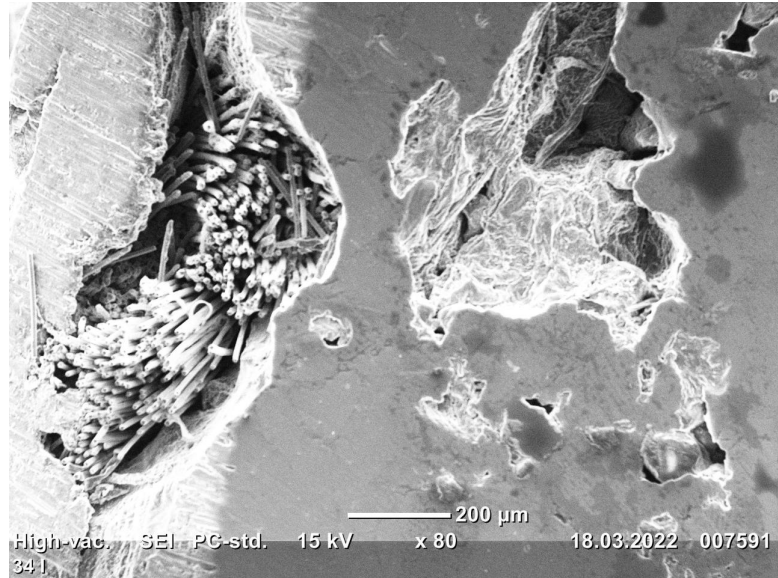


**Figure C.19:** Weaves and cavities caused by casting shrinkages in the sample of geometrical shaped filter PO48 - 25054 (20x43L). Zoom = x11. SEI. High-Vacuum.



**Figure C.20:** Weaves and cavities caused by casting shrinkages in the sample of geometrical shaped filter PO48 - 25054 (20x43L). Zoom = x11. SEI. High-Vacuum.

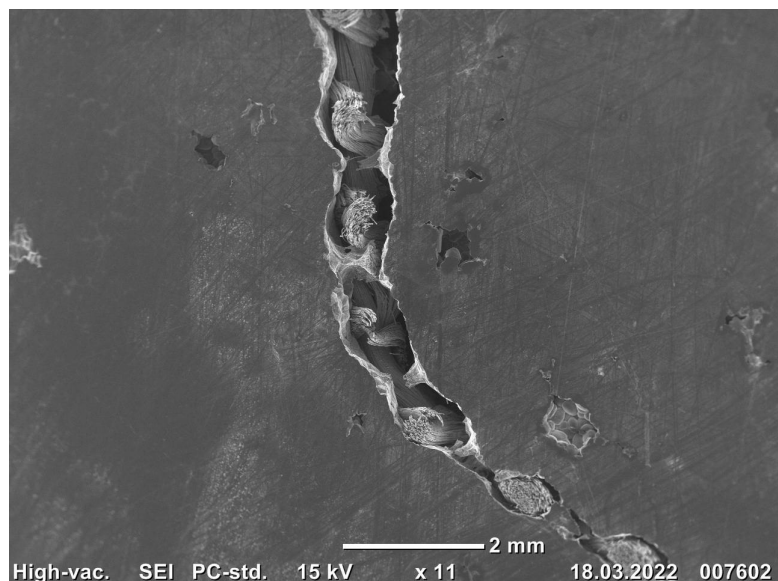
**Figure C.21:** Close-up of a weave, cavities caused by casting shrinkage and possible permeation of ethanol in the sample of geometrical shaped filter PO48 - 25054 (20x43L). Zoom = x80. SEI. High-Vacuum.



**Figure C.22:** Close-up of a weave, cavities caused by casting shrinkage and possible permeation of ethanol in the sample of geometrical shaped filter PO48 - 25054 (20x43L). Zoom = x100. SEI. High-Vacuum.



**Figure C.23:** Close-up of a weave and cavities caused by casting shrinkage in the sample of geometrical shaped filter PO48 - 2505X (20xXW2). Zoom = x11. SEI. High-Vacuum.





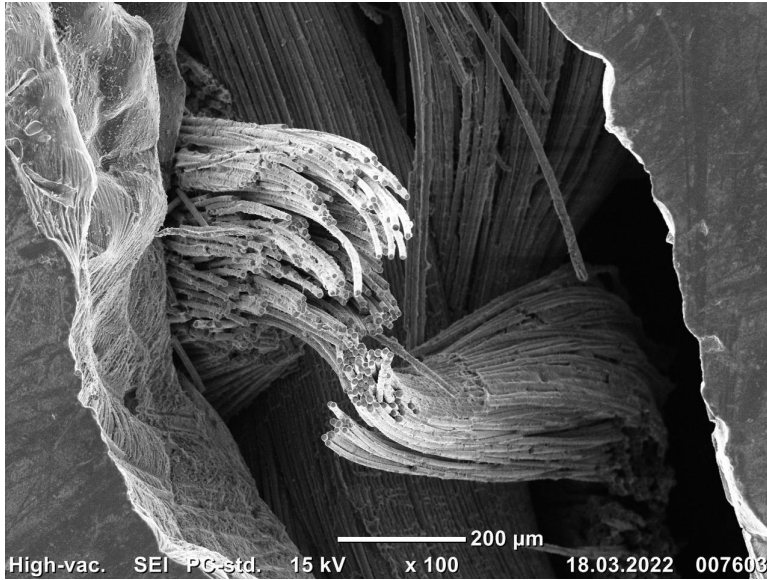


**Figure C.24:** Close-up of a weave in the sample of geometrical shaped filter PO48 - 2505X (20xXW2). Zoom = x100. SEI. High-Vacuum.

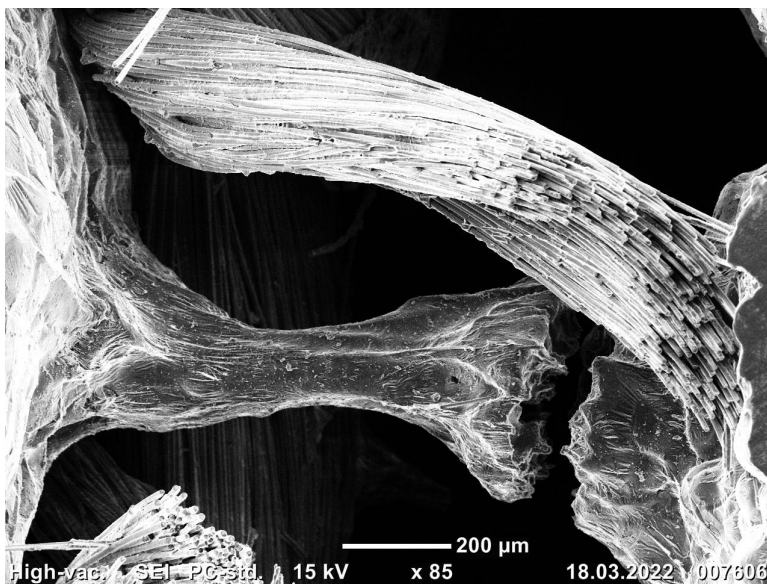


**Figure C.25:** Close-up of a weave and possible wetting in the sample of geometrical shaped filter PO48 - 2505X (20xXW2). Zoom = x85. SEI. High-Vacuum.

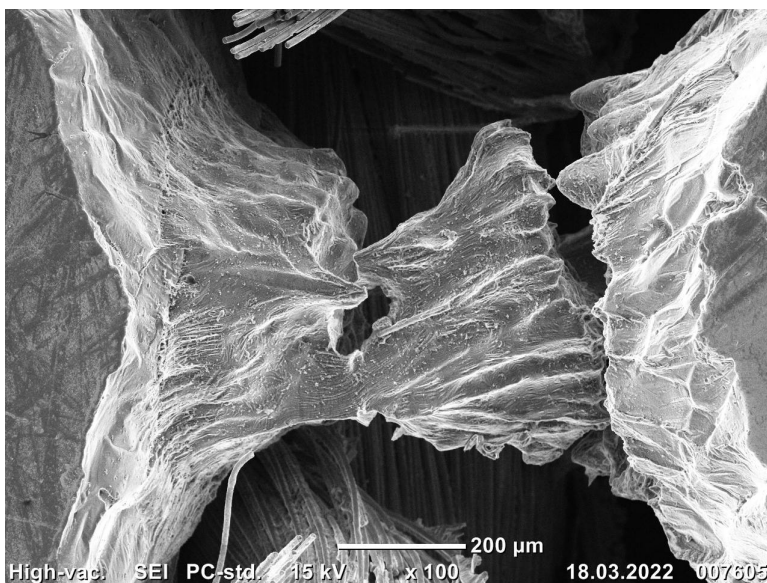


**Figure C.26:** Close-up of possible wetting in the sample of geometrical shaped filter PO48 - 2505X (20xXW2). Zoom = x100. SEI. High-Vacuum.

**Figure C.27:** Close-up of a weave in the sample of geometrical shaped filter PO48 - 2505X (20xXW2). Zoom = x100. SEI. High-Vacuum.

